

Editorial corner – a personal view

Cell-instructive hydrogels to assemble in biofluids

C. Werner*

Leibniz Institute of Polymer Research Dresden and TU Dresden, Germany

Embedding cells in engineered polymer matrices, which mimic fundamental characteristics of naturally occurring extracellular microenvironments, is a key task in the rapidly progressing fields of tissue engineering and regenerative medicine (DOI: [10.1038/nature08602](https://doi.org/10.1038/nature08602)). Importantly, cell-instructive matrix signals – including matrix-associated growth factors, ligands of cellular adhesion receptors, intrinsic viscoelastic properties and susceptibility for cell-driven reorganization – have to be presented in a spatiotemporally adjusted manner (DOI: [10.1002/marc.201200382](https://doi.org/10.1002/marc.201200382)).

For that purpose, the current practice in cell biology and biotechnology mostly relies on reconstituting non-covalently associating biopolymer meshworks (collagen fibrils, Matrigel). Although effective in numerous *in vitro* approaches to cell signaling, these preparations are hardly compatible with safety requirements for medical applications and are often not suitable for the mechanistic investigation of particular exogenous signals.

Recent approaches have therefore aimed at forming covalent polymer hydrogel networks in the presence of cells in culture or even within living tissue. A range of poly(ethylene glycol) (PEG) conjugates with adhesive peptide ligands and/or degradable peptide crosslinkers were converted in cell-compatible crosslinking schemes, including Michael-type addition, triazole formation, enzymatic (Factor XIIIa/transglutaminase-mediated) crosslinking, and photo-induced polymerization.

Amongst these, the Michael-type addition reaction turned out to be particularly powerful, as it does not require a catalyst, has no side products, and pro-

ceeds rapidly under physiological conditions (DOI: [10.1002/adma.201103574](https://doi.org/10.1002/adma.201103574)). The thiol group of cysteine residues can participate as a nucleophile in this reaction, which massively extends the number of suitable substrates and simplifies the attachment of bioactive peptides or proteins. A very common synthetic scheme for the formation of PEG-peptide hydrogels utilizes dithiol-containing peptides to react with PEG-polymers carrying electron deficient double bonds at the terminal groups.

Recently, this scheme was further extended by incorporating glycosaminoglycan building blocks for the *in situ* formation of biohybrid gel matrices, which allows for the versatile biomimetic functionalization of the obtained materials with a plethora of glycosaminoglycan-binding growth factors: Michael-type reaction schemes were applied for the formation of customized, cell-embedding, PEG-glycosaminoglycan hydrogels with precisely adjusted polymer network properties and independently tunable signaling characteristics (DOI: [10.1002/adma.201300691](https://doi.org/10.1002/adma.201300691)). These materials provide a means for the effective modulation of therapeutically relevant cell fate decisions *in vivo* and are thus expected to become instrumental in medical technologies aimed at regenerating diseased or injured tissues.



Prof. Dr. Carsten Werner
Member of International Advisory Board

*Corresponding author, e-mail: werner@ipfdd.de
© BME-PT

Surface and thermomechanical characterization of polyurethane networks based on poly(dimethylsiloxane) and hyperbranched polyester

M. V. Pergal^{1*}, J. V. Džunuzović¹, R. Poręba², D. Micić³, P. Stefanov⁴, L. Pezo³, M. Špirková²

¹Institute of Chemistry, Technology and Metallurgy (ICTM)-Center of Chemistry, University of Belgrade, Studentski trg 12–16, 11000 Belgrade, Serbia

²Institute of Macromolecular Chemistry AS CR, v.v.i. (IMC), Nanostructured Polymers and Composites Department, Heyrovského nam. 2, 16206 Prague, Czech Republic

³Institute of General and Physical Chemistry, University of Belgrade, Studentski trg 12–16, 11000 Belgrade, Serbia

⁴Institute of General and Inorganic Chemistry, Bulgarian Academy of Sciences, Acad. Georgi Bonchev 11, 1113 Sofia, Bulgaria

Received 3 April 2013; accepted in revised form 10 June 2013

Abstract. Two series of polyurethane (PU) networks based on Boltorn[®] hyperbranched polyester (HBP) and hydroxyethoxy propyl terminated poly(dimethylsiloxane) (EO-PDMS) or hydroxy propyl terminated poly(dimethylsiloxane) (HP-PDMS), were synthesized. The effect of the type of soft PDMS segment on the properties of PUs was investigated by Fourier transform infrared spectroscopy (FTIR), contact angle measurements, surface free energy determination, X-ray photoelectron spectroscopy (XPS), scanning electron microscopy (SEM), atomic force microscopy (AFM), dynamic mechanical thermal analysis (DMTA) and differential scanning calorimetry (DSC). The surface characterization of PUs showed existence of slightly amphiphilic character and it revealed that PUs based on HP-PDMS have lower surface free energy, more hydrophobic surface and better waterproof performances than PUs based on EO-PDMS. PUs based on HP-PDMS had higher crosslinking density than PUs based on EO-PDMS. DSC and DMTA results revealed that these newly-synthesized PUs exhibit the glass transition temperatures of the soft and hard segments. DMTA, SEM and AFM results confirmed existence of microphase separated morphology. The results obtained in this work indicate that PU networks based on HBP and PDMS have improved surface and thermomechanical properties.

Keywords: coatings, poly(urethane-siloxane)s, hyperbranched polyester, surface free energy, dynamic mechanical analysis

1. Introduction

Polyurethane (PU) coatings are very important because of their excellent mechanical properties, good hardness and high abrasion resistance [1, 2]. The properties of PU coatings can be tailor-made by appropriate selection of the constituents such as soft and hard segments and using an appropriate amount of crosslinker. However, poor thermal stability of conventional PU coatings limits their high temperature applications [3, 4]. For PU to be useful at high

temperatures, its architecture should be modified by introducing poly(dimethylsiloxane) (PDMS) segments in the PU backbone [5]. Therefore, many investigations have been carried out in which PDMS was used as a component of polyurethane to improve PU properties, such as water resistance, flame resistance, and thermal stability [6, 7]. Furthermore, PU with PDMS has been tested as a component of foul-release type coatings due to its smooth and non-stick surface [6].

*Corresponding author, e-mail: marijav@chem.bg.ac.rs

© BME-PT

PDMS, a major compound in the class of polysiloxanes, has a number of unique and specific properties such as high thermal and oxidative stability, good water resistance, biocompatibility, low surface tension, low glass transition temperature, high permeability to many gases and very good UV stability [8, 9]. However, poor mechanical properties and abrasion resistance of PDMS limit its application in many fields [10]. Another shortcoming is its incompatibility with organic polymers arising from the non-polar nature of the PDMS based on its very low solubility parameter ($14.9 \text{ J}^{1/2} \cdot \text{cm}^{-3/2}$) compared to other polymers ($17.6\text{--}28.6 \text{ J}^{1/2} \cdot \text{cm}^{-3/2}$). The non-polar nature of the PDMS structure combined with the weak intermolecular interaction leads to the creation of a polymer phase that is both thermodynamically and mechanically incompatible, not only with the PU components, but also with all organic monomers and with other polymer. This leads to the formation of phase-segregated morphology of PUs [8]. Polyurethane networks based on PDMS macrodiols and hyperbranched polyesters (HBP) as crosslinkers introduced into the hard segment domains can combine properties of all components, making these networks good candidates for coating applications. The large number of terminal hydroxyl groups present in Boltorn[®] HBPs enables fast formation of networks that have good mechanical properties, as well as good resistance to chemicals [11–14], while the presence of PDMS contributes to the good thermal and surface properties, and to elasticity of the highly crosslinked materials. In our previous studies, we have investigated the influence of the content of α,ω -dihydroxyethoxy propyl-poly(dimethylsiloxane) (EO-PDMS) and type of HBPs on the swelling behavior, morphological, thermal and thermomechanical properties of PU networks [15–21]. These results confirmed that physical and thermal properties are related to the crosslinking density, hydrogen bonding interactions, microphase separation and content of EO-PDMS soft segment. The aim of our previous studies was to prepare poly(urethane-siloxane) networks with good thermal, mechanical and surface properties, which would be suitable for coating applications.

As far as we are aware, there is a paucity of peer-reviewed literature on the surface free energy of these particular polyurethanes prepared in the form of films, which is especially important for coatings.

In the present work, therefore, we have studied the surface and thermomechanical properties of PU networks prepared with different types of soft PDMS segment, as part of our efforts to produce improved PUs. Two series of PU networks based on hydroxyethoxy propyl terminated PDMS or hydroxy propyl terminated PDMS as the soft segment and 4,4'-methylenediphenyl diisocyanate and Boltorn[®] hyperbranched polyester of the third pseudo generation (BH-30) as components of hard segment were prepared. The PU networks were characterized by Fourier transform infrared spectroscopy (FTIR), contact angle measurements, surface free energy determination, X-ray photoelectron spectroscopy (XPS), scanning electron microscopy (SEM), atomic force microscopy (AFM), dynamic mechanical thermal analysis (DMTA) and differential scanning calorimetry (DSC).

2. Experimental

2.1. Materials

α,ω -Dihydroxyethoxy propyl-poly(dimethylsiloxane) (EO-PDMS) and α,ω -dihydroxypropyl-poly(dimethylsiloxane) (HP-PDMS) supplied from ABCR (Karlsruhe, Germany) were dried over molecular sieves (0.4 nm) before use. The average molecular weights, M_n , of the EO-PDMS and HP-PDMS were calculated from ¹H NMR spectroscopy. In addition, the degree of polymerization of the PDMS-block in the EO-PDMS and HP-PDMS prepolymers was determined as the relative intensities of the Si-CH₃ protons signals and the terminal -CH₂- protons in the ethylene oxide residue or the -CH₂- protons arising from the PDMS propylene groups which were connected to oxygen atoms in hydroxyl groups, respectively. Therefore, the degree of polymerization of PDMS-block in the EO-PDMS and HP-PDMS prepolymers was 12.8 and 10.6. The M_n of the prepolymer EO-PDMS was 1200 g/mol [22], while for the prepolymer HP-PDMS it was 960 g/mol. 4,4'-Methylenediphenyl diisocyanate (MDI) (supplied from Aldrich, Steinheim, Germany), with an isocyanate content of 33.6 wt%, was used as received. Commercially available Boltorn[®] hydroxy-functional aliphatic HBP of the third pseudo generation (BH-30) was kindly supplied by Perstorp Specialty Chemicals AB (Sweden) and dried at 50°C under vacuum for 48 h prior to use. The aliphatic hyperbranched polyester is based on 2,2-bis(hydrox-

ymethyl)propionic acid as a monomer and tetrafunctional ethoxylated pentaerythritol as a core [23]. For the exact calculation of the amounts of all components necessary for the synthesis of PUs, the value of the molecular weight determined by vapor pressure osmometry ($M_n = 3080$ g/mol) and hydroxyl number of BH-30 determined by titration method ($HN = 474.1$ mg KOH/g) were used. Consequently, the exact functionality, f_n , of the BH-30 used was calculated ($f_n = 26$) [24]. The catalyst was stannous-octanoate ($\text{Sn}(\text{Oct})_2$), supplied from Aldrich (St. Louis, USA). The solvent *N*-methyl-2-pyrrolidone (NMP) supplied from Acros (Geel, Belgium) was dried over calcium-hydride and distilled before use. Tetrahydrofuran (THF) supplied from J.T. Baker (Center Valley, USA) was refluxed with lithium-aluminum hydride and distilled before use. Formamide (analytically pure, Merck, Darmstadt, Germany) and diiodomethane (analytically pure, UCB, Brussels, Belgium) were used as received.

2.2. Synthesis of PU films based on PDMS and control sample

Two series of PU networks based on PDMS macrodiols, MDI and Boltorn[®] HBP were synthesized by a two-step polymerization in solution, using a mixture of *N*-methyl-2-pyrrolidone/tetrahydrofuran as the solvent and stannous octanoate as the catalyst. Macrodiols used for the preparation of samples of series PUS1 (PUS1-15 and PUS1-30) and PUS2 (PUS2-15 and PUS2-30) were hydroxyethoxy propyl terminated PDMS and hydroxy propyl terminated PDMS, respectively. Each series of the synthesized PUs consisted of two samples of different PDMS content (15 and 30 wt%), which, in this study, is marked by the last two numbers in the name of prepared samples. The total molar ratio of –NCO (from MDI) and –OH groups (from PDMS macrodiol and BH-30) was, for all samples, kept constant (NCO/OH = 1.05) [25–27]. Catalyst concentration was kept at 0.02 wt% [25–27]. The details for the synthesis of similar PU networks are given in our previously published papers [16–21]. Compositions of the synthesized PUs and weights of the reactants used for the synthesis of PUs are presented in Table 1. PU samples were synthesized in 100 mL four-neck round-bottom flasks, placed in a silicone oil bath and connected to an inlet for dry argon, a mechanical stirrer, a dropping funnel and a reflux condenser. Calculated amounts of macrodiol and MDI were

Table 1. Compositions of the synthesized PUs and weights of reactants used for their preparation

Sample	Soft segment content [wt%]	PDMS macrodiol [g]	MDI [g]	BH-30 [g]
PUS1-15	15	2.5004	7.7706	6.4615
PUS1-30	30	4.0004	5.3212	4.0128
PUS2-15	15	2.5004	7.7714	6.3965
PUS2-30	30	4.0004	5.4258	3.9096
MDI-BH30	0	0	5.0002	4.5128

weighed into reaction flask at room temperature, dissolved in the mixture of NMP/THF and then heated up to 40°C under an argon atmosphere. The reaction started by the introduction of a solution of $\text{Sn}(\text{Oct})_2$ in NMP. The reaction mixture was stirred for 30 min (for the PUS1 series) or 20 min (for the PUS2 series) at 40°C to prepare the NCO-terminated prepolymer, i.e. until the theoretical NCO content was attained. The NCO content was controlled by the dibutylamine back-titration method [28]. In the second stage of the reaction, a dilute solution of BH-30 in NMP was added drop-wise to the NCO-terminated prepolymer and the reaction was continued at 40°C for 10 min. Finally, the obtained reaction mixture was cast into Petri dishes. The crosslinking reaction was continued in a force-draft oven during 40 h at 80°C and 1 h at 110°C, and finally 10 h at 50°C in a vacuum oven. The thickness of the synthesized yellow PU films was about 1 mm. The synthesis of the control (MDI-BH30) sample, prepared without PDMS macrodiol, was carried out at the same conditions, but the crosslinking reaction proceeded at ambient temperature for 24 h, and then in a vacuum oven at 50°C for 10 h and at 80°C for 12 h.

2.3. Characterization

FTIR spectra of PUs were recorded using the attenuated total reflection (ATR) mode on Nicolet 6700 FTIR spectrometer (Madison, USA). The scanning range was from 500 to 4000 cm^{-1} at the resolution of 4 cm^{-1} , and 64 scans were collected for each sample.

The static contact angles were measured using a contact angle analyzer (Krüss DSA100, Hamburg, Germany), equipped with software for a drop shape analysis. The static contact angle (θ) was measured by a sessile drop method at a temperature of 23°C. Single drops of test liquids with volumes of 20 μL were deposited on the polymer film surface and the

contact angles were measured after 30 s. In all cases, at least five measurements were used, and the average contact angle was calculated. The equilibrium contact angle is defined as the angle between the solid surface and a tangent, drawn on the drop-surface, passing through the triple-point atmosphere-liquid-solid [29]. The relationship between three interfacial tensions is given by Young’s Equation (1):

$$\cos\theta = \frac{\gamma_{\text{solid/vapor}} - \gamma_{\text{solid/liquid}}}{\gamma_{\text{liquid/vapor}}} \quad (1)$$

where $\gamma_{\text{solid/vapor}}$ is the energy of the surface, $\gamma_{\text{solid/liquid}}$ is the interfacial tension between the solid and the drop of liquid, $\gamma_{\text{liquid/vapor}}$ is the liquid-vapor surface tension and θ is the contact angle of the drop with the surface.

The surface free energy of PUs was calculated according to the van Oss Chaudhury Good method [30]. This method has been widely used to investigate the surface free energy of polymer films that are used as coatings. For reliable determination of the surface energy, three test liquids (distilled water, formamide and diiodomethane) with known surface tensions [31, 32], ranging from very polar to non-polar, were utilized to determine the surface free energy of the PU films, as shown in Table 2. The surface free energy and its components were calculated by solving the following set Equations (2) [30]:

$$\begin{aligned} \gamma_{LV1}(1-\cos\theta_1) &= 2\sqrt{\gamma_S^{LW}\gamma_{LV1}^{LW}} + \sqrt{\gamma_S^+\gamma_{LV1}^-} + \sqrt{\gamma_S^-\gamma_{LV1}^+} \\ \gamma_{LV2}(1-\cos\theta_2) &= 2\sqrt{\gamma_S^{LW}\gamma_{LV2}^{LW}} + \sqrt{\gamma_S^+\gamma_{LV2}^-} + \sqrt{\gamma_S^-\gamma_{LV2}^+} \\ \gamma_{LV3}(1-\cos\theta_3) &= 2\sqrt{\gamma_S^{LW}\gamma_{LV3}^{LW}} + \sqrt{\gamma_S^+\gamma_{LV3}^-} + \sqrt{\gamma_S^-\gamma_{LV3}^+} \\ \gamma_S &= \gamma_S^{LW} + \gamma_S^{AB} = \gamma_S^{LW} + 2\sqrt{\gamma_S^+\gamma_S^-} \end{aligned} \quad (2)$$

where γ_s is the surface free energy that can be divided into two components: the dispersive (γ^{LW}) which represent the van der Waals interactions, and the polar component (γ^{AB}) including the Lewis acid parameter (γ^+) and the Lewis base parameter (γ^-). γ_{LV} is the surface tension of the liquid in equilibrium with its own vapor. The total surface energy and its components could be obtained by solving Equation (2), since values of γ_{LV}^{LW} , γ_{LV}^+ , γ_{LV}^- are known. The surface composition of the PU films was determined by X-ray photoelectron spectroscopy (XPS) using a VG ESCALAB II electron spectrometer

Table 2. Surface tension of the examined liquids for surface energy determination

Liquids	γ_{LV} [mJ/m ²]	γ_{LV}^{LW} [mJ/m ²]	γ_{LV}^+ [mJ/m ²]	γ_{LV}^- [mJ/m ²]
Distilled water	72.8	21.8	25.5	25.5
Formamide	58.0	39.0	2.28	39.6
Diiodomethane	50.8	50.8	0	0

(East Grinstead, England) under a base pressure of $1 \cdot 10^{-8}$ Pa. The photoelectron spectra were excited using non-monochromatized Al K $_{\alpha}$ radiation ($h\nu = 1486.6$ eV) with a total instrumental resolution of 1 eV. The photoelectron spectra were corrected by subtracting a Shirley-type background and were quantified using the peak area and Scofield photoionization cross-sections.

Scanning electron microscopy (SEM) micrographs of the PUs were obtained on a JEOL JSM-6610 instrument (Tokyo, Japan), at a working distance of *ca.* 14 mm and an accelerating voltage of 20 kV.

Investigation of the surface topography and heterogeneity relief was done by the atomic force microscope (DimensionIcon, Bruker, Santa Barbara, USA), equipped with the SSS-NCL probe, Super Sharp SiliconTM- SPM-Sensor (NanoSensorsTM Switzerland; spring constant 35 N/m, resonant frequency ≈ 170 kHz). Measurements were performed under ambient conditions using the tapping mode AFM technique. The scans covered the sizes of 10×10 μm . The AFM images of the fracture areas of PU films after previous freeze-fracturing at the temperature of liquid were measured in order to evaluate the inner arrangement in the bulk system.

Dynamic mechanical thermal analysis (DMTA) was performed on an ARES G2 rheometer (TA Instruments, New Castle, USA) at a frequency of 1 Hz, strain 0.1%, with a heating rate of 3°C/min and in the temperature range from -135 to 180°C . The measurements were carried out using rectangular specimens ($15.0 \text{ mm} \times 7.8 \text{ mm} \times 1.0 \text{ mm} \pm 0.2 \text{ mm}$), under torsion mode, using torsion fixture (rectangle) geometry. All details of the calculation of crosslinking density and average molecular weight between two crosslinks using the rubber elasticity theory and calculated from DMTA results, are described in the literature [19–21, 33]. Some clarification of the calculation of crosslinking density is given. The crosslinking density of the synthesized PU networks can be calculated from the rubber elasticity theory using Equation (3) and (4):

$$\nu = \frac{G'}{RT} \quad (3)$$

where G' represents rubbery plateau modulus at $T = (T_{gHS})_{G'} + 90^\circ\text{C}$, $(T_{gHS})_{G'}$ is the glass transition temperature of the hard segments determined from loss modulus (G'') maximum, T is the temperature in Kelvin and R is the universal gas constant. Value of the molecular weight of polymer chain between crosslinks (M_c) was evaluated as:

$$M_c = \frac{\rho_{PU}}{\nu} \quad (4)$$

where ρ_{PU} is the density of PUs.

Differential scanning calorimetry (DSC) was carried out on a DSC Q1000V9.0 Build 275 thermal analyzer (New Castle, USA). The DSC scans were recorded under a dynamic nitrogen atmosphere (the flow rate of nitrogen was 50 mL/min), in the temperature range from -140 to 230°C , at a heating and cooling rate of 10 and $5^\circ\text{C}/\text{min}$, respectively.

3. Results and discussion

3.1. Synthesis of the PU networks

Two series of PUs based on Boltorn[®] hyperbranched polyester of the third pseudo generation, 4,4'-methylenediphenyl diisocyanate and hydroxyethoxy propyl terminated poly(dimethylsiloxane) (samples

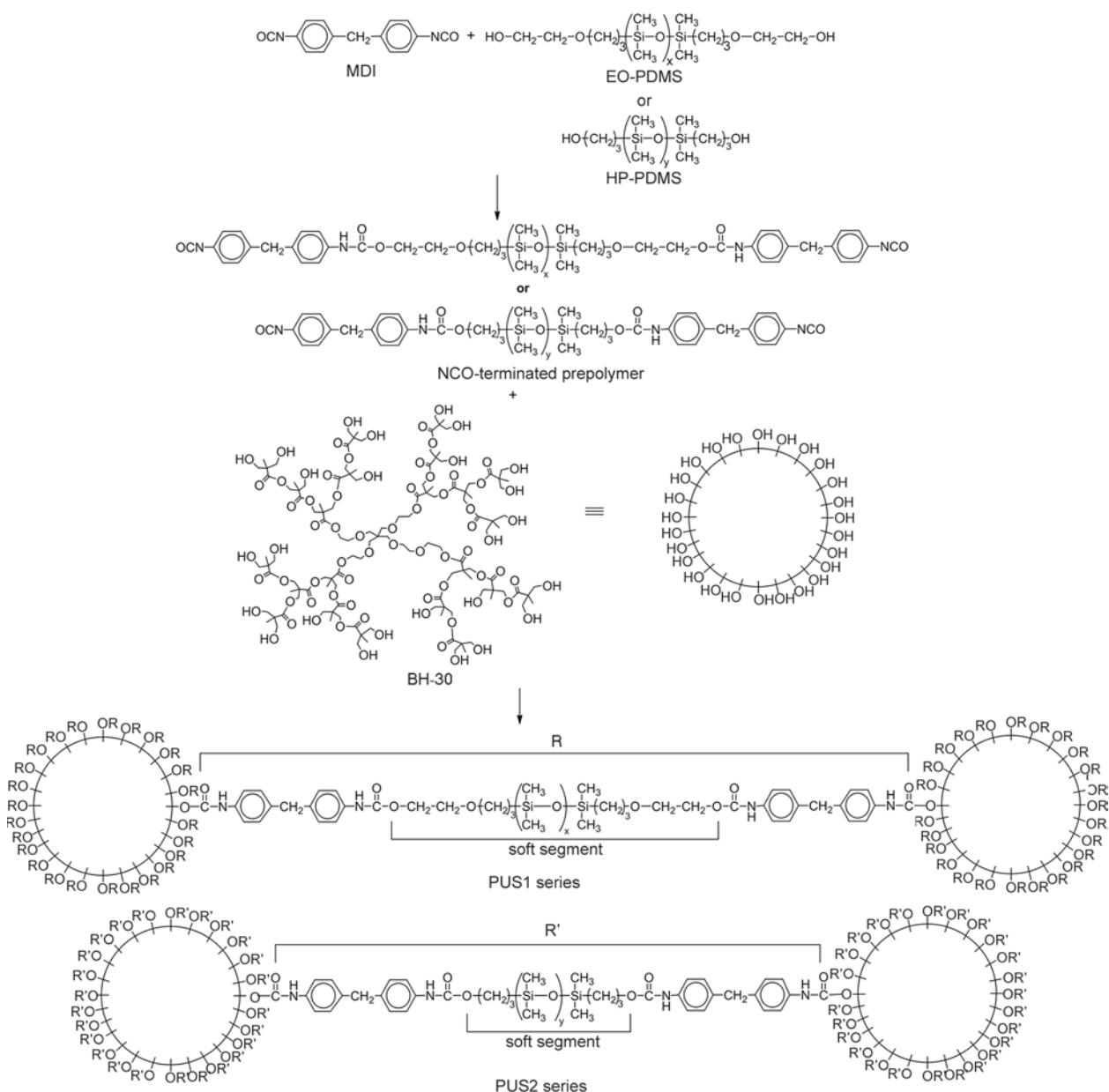


Figure 1. The simplified reaction pathway of the synthesis of PU networks based on EO-PDMS (PUS1 series) and HP-PDMS (PUS2 series)

of the PUS1 series) or hydroxy propyl terminated poly(dimethylsiloxane) (samples of the PUS2 series) were synthesized by a two-step polymerization in solution. In our previous work, PUs were synthesized in melt using BH-20, MDI and two different macrodiols: poly(tetramethylene oxide) and EO-PDMS [15]. However, our results showed that the polymerization in melt and incompatibility of non-polar EO-PDMS with polar reactants, i.e. BH-20 and MDI, led to the formation of heterogeneous PU networks. Therefore, in this work, a two-step polymerization in solution was applied to improve the compatibility between reactants during the synthesis of PUs. The mixture of NMP/THF was used as a reaction medium for the synthesis of PUs. The simplified reaction pathway of the synthesis of PU networks based on EO-PDMS and HP-PDMS is shown in Figure 1.

3.2. FTIR characterization

The chemical structure of PUs was investigated by FTIR spectroscopy. In Figure 2, FTIR spectra of the synthesized PUs and the control sample are given. In the FTIR spectrum of the control sample, the presence of urethane -NH groups at 3320 cm^{-1} can be observed, while the characteristic region at $1700\text{--}1735\text{ cm}^{-1}$ was ascribed to the carbonyl urethane and ester groups. The amide II and amide III bands appeared at 1547 and 1260 cm^{-1} , respectively. The FTIR absorption bands characteristic for the C-O-C groups (1040 and 1120 cm^{-1}), aromatic C=C linkage (1599 and 1411 cm^{-1}) and $\text{-CH}_2\text{-}$ and -CH_3 groups ($2900\text{--}3000\text{ cm}^{-1}$) can also be observed in the FTIR spectrum of the control sample.

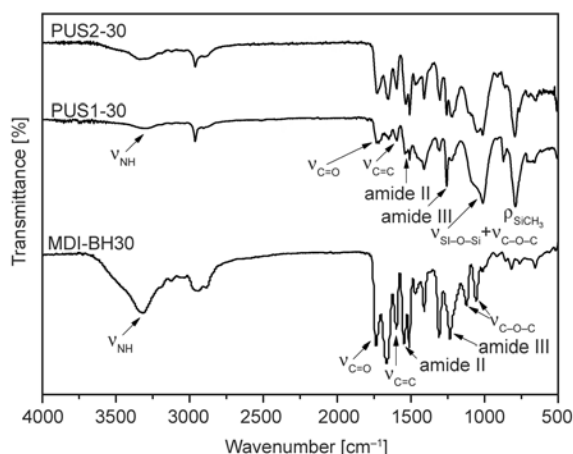


Figure 2. FTIR spectra of the synthesized PUs and the control MDI-BH30 sample

In the FTIR spectra of PUs, peaks corresponding to amide II and amide III vibrations were observed at around 1537 and 1258 cm^{-1} , respectively. The peaks which were ascribed to the C=O and -NH vibrations were detected in the regions $1645\text{--}1735\text{ cm}^{-1}$ and $3100\text{--}3500\text{ cm}^{-1}$, respectively. The absorption bands which were observed at around 1015 and 1080 cm^{-1} represent overlapped bands of Si-O-Si and C-O-C groups, respectively. The absorption band at around 790 cm^{-1} was ascribed to the Si-CH_3 linkage. The presence of the symmetric and asymmetric $\text{-CH}_2\text{-}$ and -CH_3 groups was observed at around 2961 , 2903 and 2875 cm^{-1} . Other bands at around 1596 and 1412 cm^{-1} were assigned to the aromatic C=C . Since no peak was detected at 2260 cm^{-1} in the FTIR spectra of these PUs, it can be concluded that all isocyanate groups were incorporated into the polymer chains.

3.3. Contact angles and surface free energy

Since the synthesized PUs prepared from the soft PDMS and hard MDI-HBP segments were designed to obtain materials for coating applications, their surface energy and wettability play a key role. The results obtained from contact angle measurements and the surface free energy determinations are presented in Tables 3 and 4. Post-hoc Tukey's HSD test at 95% confidence limit was calculated to show significant differences between different samples. The surface energy of the synthesized PUs and control sample is shown in Figure 3.

The water contact angles of PUS2 series were higher than values obtained for samples from PUS1 series. Therefore, the synthesized PUs based on HP-PDMS were more hydrophobic, i.e. had better waterproof properties than PUs based on EO-PDMS. From the results, it is also quite apparent that the synthesized PUs had higher water contact angles than the con-

Table 3. Water contact angle, θ_1 , formamide contact angle, θ_2 , and diiodomethane contact angle, θ_3 , of the synthesized PUs and control sample

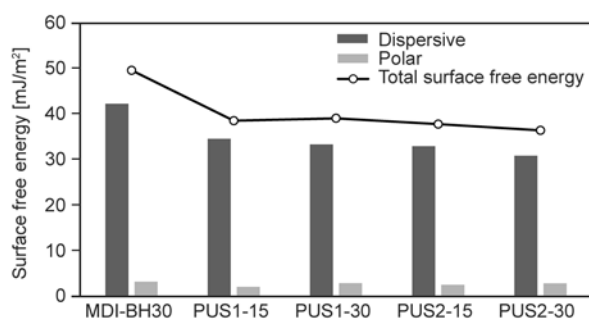
Sample	θ_1 [°]	θ_2 [°]	θ_3 [°]
PUS1-15	86.23 ± 0.90^a	67.75 ± 0.85^c	49.50 ± 0.95^c
PUS1-30	86.78 ± 0.79^{ab}	75.88 ± 1.45^a	51.73 ± 0.79^a
PUS2-15	88.13 ± 0.46^{bc}	74.33 ± 0.51^a	52.40 ± 0.48^a
PUS2-30	89.53 ± 0.92^c	79.70 ± 0.75^d	56.05 ± 0.56^d
MDI-BH30	74.68 ± 0.75^d	62.98 ± 0.72^b	34.50 ± 0.59^b

^{a,b,c,d}Different letters printed in superscript within the same column show significantly different means of observed data (at $p < 0.05$ level, according to post-hoc Tukey's HSD test)

Table 4. Surface free energy and its components of the synthesized PUs and control sample

Sample	γ_s^{LB} [mJ/m ²]	γ_s^{AB} [mJ/m ²]	γ_s^+ [mJ/m ²]	γ_s^- [mJ/m ²]	$\gamma_{s(total)}$ [mJ/m ²]
PUS1-15	34.55±0.53 ^c	2.07±0.14 ^b	1.91±0.14 ^b	3.97±0.15 ^b	38.52±0.58 ^{ab}
PUS1-30	33.30±0.45 ^a	2.89±0.18 ^a	2.83±0.24 ^a	5.72±0.38 ^a	39.03±0.52 ^b
PUS2-15	32.92±0.27 ^a	2.55±0.05 ^c	2.29±0.08 ^c	4.83±0.06 ^c	37.75±0.24 ^a
PUS2-30	30.84±0.32 ^b	2.86±0.07 ^a	2.70±0.14 ^a	5.55±0.09 ^a	36.39±0.34 ^c
MDI-BH30	42.25±0.27 ^d	3.21±0.13 ^d	4.19±0.16 ^d	7.33±0.21 ^d	49.59±0.46 ^d

^{a,b,c,d}Different letters printed in superscript within the same column show significantly different means of observed data (at $p < 0.05$ level, according to post-hoc Tukey's HSD test)

**Figure 3.** Surface free energy of the synthesized PUs and control MDI-BH30 sample

control sample. This behavior may be ascribed to the tendency of the PDMS segments to migrate to the surface, due to the very low surface energy of PDMS, resulting in a part of the PU surfaces being covered by PDMS [31]. As can be seen (Table 3), the change of the formamide and diiodomethane contact angles of PU samples followed the same trend as the water contact angle.

According to the Figure 3, the surface free energy of the samples based on HP-PDMS was lower than that of samples based on EO-PDMS. The dispersive component decreased, but the polar component did not vary for the PUs based on HP-PDMS. The synthesized PU samples had lower values of surface energy compared to the control sample (Table 4). Furthermore, the surface energy values of our PU samples were higher than values presented in the literature for siloxane-urethane coatings (around 25 mJ/m²) [34] and linear high molecular weight PDMS (21 mJ/m²) [35]. In contrast, the surface free energy values of our newly-synthesized PUs were closer to that of the control MDI-BH30 sample (49.6 mJ/m²). These results indicated that PDMS covers only a part of the surface of these novel PUs. Therefore, surface energy studies have confirmed the presence of both hydrophobic PDMS and hydrophilic urethane groups at the surface, giving a slight amphiphilic character to the surface of the PU samples.

The water contact angle of PUs was higher but the surface free energy was lower than the values obtained for previously synthesized PU networks based on EO-PDMS and hyperbranched polyester of the fourth pseudo generation ($\theta_1 = 82.6$ – 87.3° and $\gamma_{s(total)} = 38.7$ – 43.8 mJ/m²) [21].

3.4. XPS analysis

XPS investigation was conducted to provide information of surface elemental composition of PU networks. Figure 4 shows XPS survey spectra and high resolution XPS spectra of the PU films.

The surface elemental composition, calculated from the normalized peak areas of C1s, O1s, N1s and Si2p core level peaks, is listed in Table 5. The surface content of Si is almost constant for most PU samples, excluding PUS1-30. This sample has also a higher concentration of carbon and nitrogen at surface. Probably, the reason for this is the presence of more urethane –NH groups. The content of nitrogen for other PU samples is at the XPS sensitivity limit.

The C1s spectra of all PU samples contain peak centered at 284.8 eV, attributed to C–C and C–H bonds in the polyurethane. Only for PUS1-30 sample the C1s peak shows asymmetry at a higher binding energy side at ~286.5 eV. According to the literature data, this feature could be assigned to the carbon formed C–O bonding [36]. The measured Si2p binding energy for all PU samples at 102.3 eV is consistent with previously published values for PDMS materials [36, 37]. The binding energy of the N1s

Table 5. XPS data of surface composition of the synthesized PUs

Sample	Surface concentration [atomic%]			
	C	O	N	Si
PUS1-15	50.2	24.9	0.2	24.7
PUS1-30	59.2	22.8	2.2	15.8
PUS2-15	51.0	24.5	0.4	24.1
PUS2-30	50.6	24.1	0.3	25.0

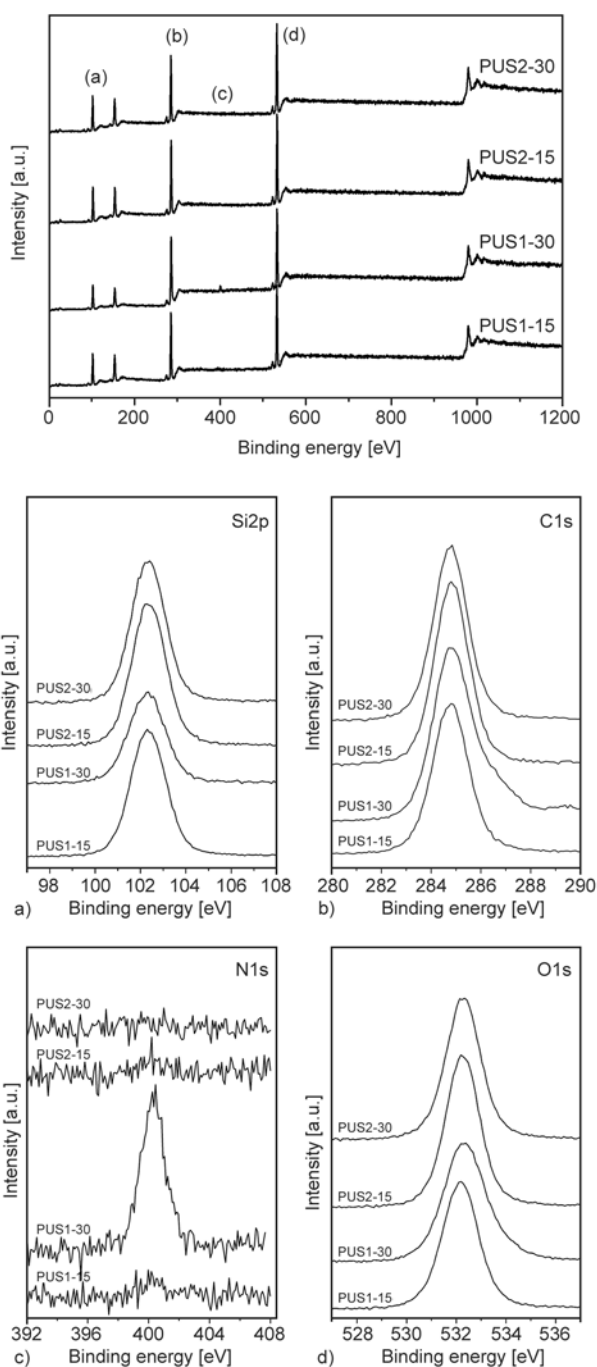


Figure 4. XPS survey spectra and high resolution XPS spectra of PUS1-15, PUS1-30, PUS2-15 and PUS2-30 films: (a) Si2p; (b) C1s; (c) N1s; (d) O1s

peak of the PUS1-30 sample at 400.4 eV is typical for urethane –NH bonds.

The obtained results showed tendency of PDMS segments to migrate to the PU surface. It stemmed from the silico-organic groups with low surface energy, incompatibility with polyurethane and high chain flexibility, which allowed its migration to the surface of PU films [37]. This result was in good agreement with that from the contact angle analysis. On the other hand, the N concentration on the surface

was very low, indicating that the urethane hard segments of samples PUS1-15, PUS2-15 and PUS2-30 were present in a small amount on their surface, except for PUS1-30.

3.5. Morphological investigation by SEM

The surface morphology of PU networks was analyzed by SEM and the obtained microphotographs are shown in Figure 5. The results obtained by SEM analysis revealed the existence of microphase separated morphology of the investigated PUs. Figure 5 shows a typical view of microdomains of hard MDI-HBP segments, hydrogen-bonded in aggregates and irregular in shapes, and unevenly dispersed in the soft PDMS matrix of the PUs, which was consistent with the results for PDMS based PUs [38]. Therefore, the brighter region in the surface view of the PUs represents the aggregates of hard segments in the darker PDMS soft segments that are more pronounced for samples with high soft segment content. This might be because the samples PUS1-30 and PUS2-30 have higher crosslinking density in comparison with PUS1-15 and PUS2-15 (Table 7). With the increase of crosslinking density, there was stronger cohesion force among hard segment chains, leading to an inclination of hard segments aggregation within soft phase. SEM results of the samples PUS1-15 and PUS2-15 indicate increased homogeneity in samples and improved compatibility of all components in comparison to PUS1-30 and PUS2-30.

3.6. AFM analysis

In order to understand the influence of the type of PDMS soft segments on the formation of surface topography and heterogeneity relief of PUs, AFM analysis was performed. The obtained results are shown in Figures 6 and 7 and summarized in Table 6. Based on prior studies, it is known that the bright regions represent the hard phase (hard domains), while the darker regions represent the soft phase in a polyurethane.

Height images, showing surface topography, substantially differ for the synthesized PUs: the topographies of PUS1-15 and PUS1-30 display particulate formations of nm size, while PUS2-15 and PUS2-30 samples show agglomerates of μm size (PUS2-15 is the roughest one). In comparison with samples from PUS1 series, the roughness of PUS2 samples is higher (see Table 6). In addition, the three-dimen-

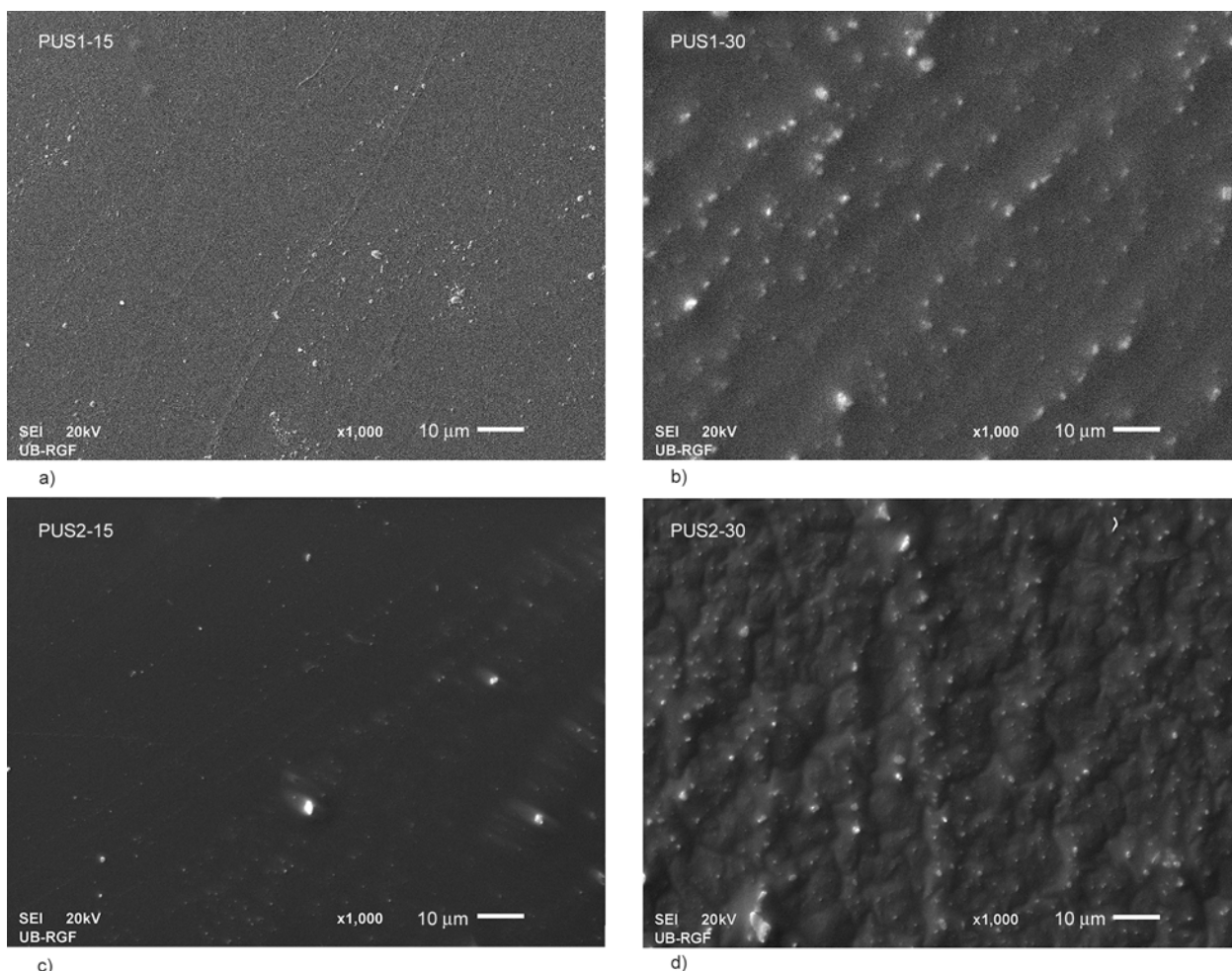


Figure 5. SEM microphotographs of the surface of the synthesized PUs: (a) PUS1-15, (b) PUS1-30, (c) PUS2-15, (d) PUS2-30

Table 6. Roughness values of the synthesized PUs

Sample	Surface area [μm^2]	R_q^* [nm]	R_a^{**} [nm]	R_{max}^{***} [nm]
PUS1-15	106	104	128	1818
PUS1-30	104	101	77	670
PUS2-15	131	839	663	4143
PUS2-30	120	385	294	2533

Surface area: the total area of examined sample surface (the three-dimensional area of a given region expressed as the sum of the area of all the triangles formed by three adjacent data points).

R_q^* (R_{ms}): the standard deviation of the Z values within the given area

R_a^{**} (mean roughness) the mean value of the surface relative to the center place

R_{max}^{***} (max height): the difference in height between the highest and lowest points on the surface relative to the mean plane

Mean: the average of all Z values within the enclosed area.

sional large-scale resolution images clearly show that the surface structure changes and the roughness diminishes with increasing content of the PDMS soft segments. These results are in agreement with those previously reported, based on surface composition

analysis, which showed that PDMS predominates on the surface of block copolymers containing PDMS segments due to its immiscibility with other polymers and its low surface energy [39].

Phase images (i.e., maps of tip-sample interactions) enable qualitative insight into the sample homogeneity relief. The synthesized PUs are characterized by two-phase morphology consisting of a hard segment-rich phase and a soft segment-rich phase. It is evident that the synthesized PU samples are distinguished by heterogeneous character, apparently connected with strong microphase separation. The obtained results showed that the synthesized samples are heterogeneous on nm (PUS1-15) or even on μm level (PUS1-30, PUS2-15 and PUS2-30). Samples PUS1-15, PUS2-15 and PUS2-30 have very sharp interface between both phases, characterized entirely black and/or white localities anticipating strong microphase separation. On the other hand, the phase image of sample PUS1-30 contains also relatively

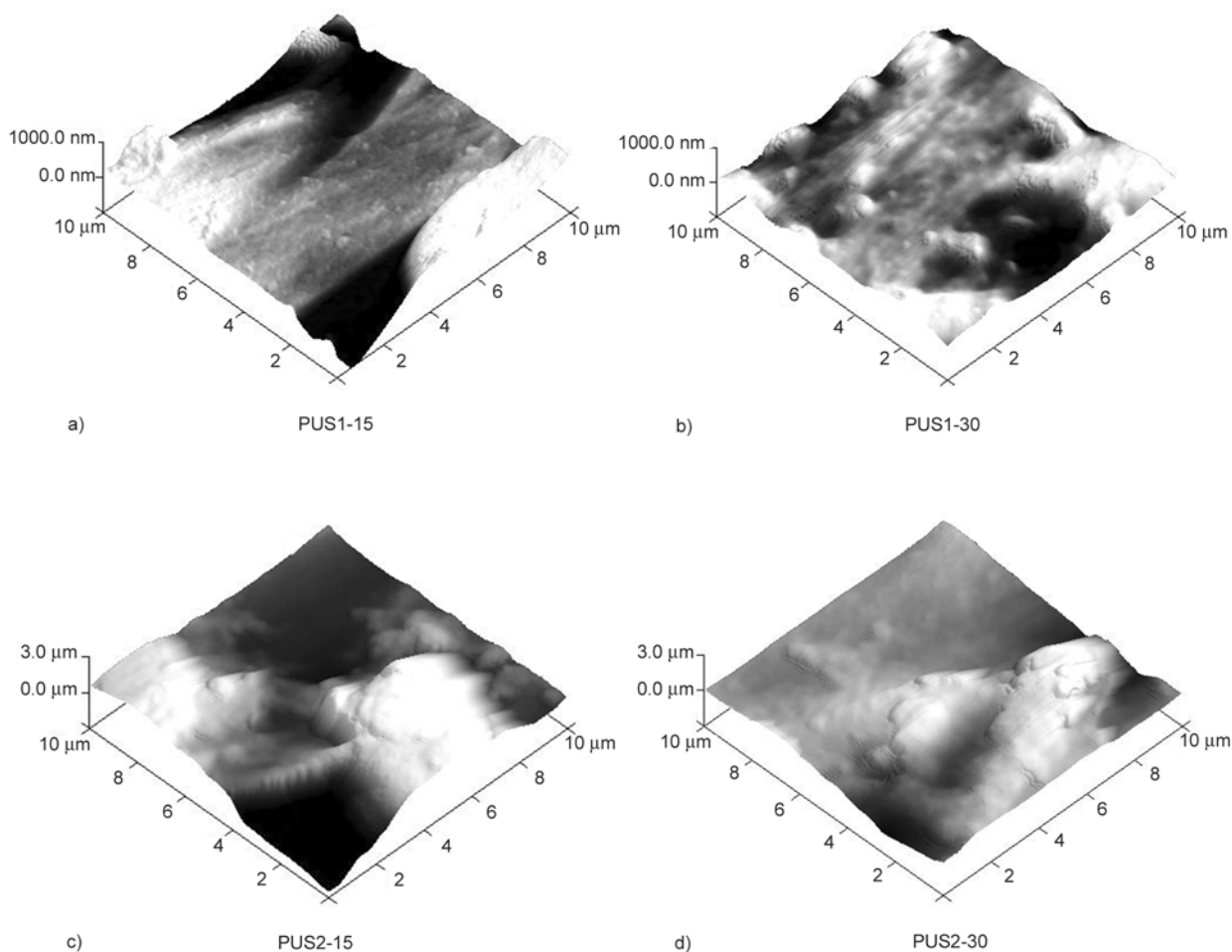


Figure 6. 3D AFM height images of the fractured surface of the synthesized PUs: (a) PUS1-15, (b) PUS1-30, (c) PUS2-15, (d) PUS2-30

Table 7. Glass transition temperatures determined by DSC, temperatures corresponding to the $\tan \delta$ maximum, crosslinking density, ν , and molecular weight of polymer chain between crosslinks, M_c , determined by DMTA of the synthesized PUs

Sample	T_{gSS} (DSC) [°C]	T_{gHS} (DSC) [°C]	$\tan \delta$			$\nu \cdot 10^4$ [mol/cm ³]	M_c [g/mol]
			T_{gSS} [°C]	T_2 [°C]	T_{gHS} [°C]		
PUS1-15	-123	50	-125	-74	45	10.61	1000
PUS1-30	-125	57	-126	-67	50/73	14.32	800
PUS2-15	-124	52	-126	-79	70	14.21	780
PUS2-30	-121	63	-118	-58	84	103.5	110

high part of grey color indicating higher degree of phase mixing compared with samples PUS1-15, PUS2-15 and PUS2-30.

3.7. DMTA and DSC analysis

Dynamic mechanical thermal measurements were used to examine viscoelastic properties of PU samples. The mechanical loss factor, $\tan \delta$, storage modulus, G' , and loss modulus, G'' , of the synthesized PUs are shown in Figures 8 and 9. The PUs exhibited two thermal transitions and probably one sec-

ond relaxation process [13]. The glass transition temperatures of PU networks were affected by the crosslinking density, plus the type and content of soft segment. The values of glass transition temperatures, obtained as the temperature of the $\tan \delta$ maximum, are shown in Table 7. Temperatures of $\tan \delta$ peaks are somewhat higher than temperatures corresponding to the G'' peaks.

The glass transition temperature in the range from -118 to -126°C is associated with the soft PDMS segment (T_{gSS}). $\tan \delta$ curves show a small maxi-

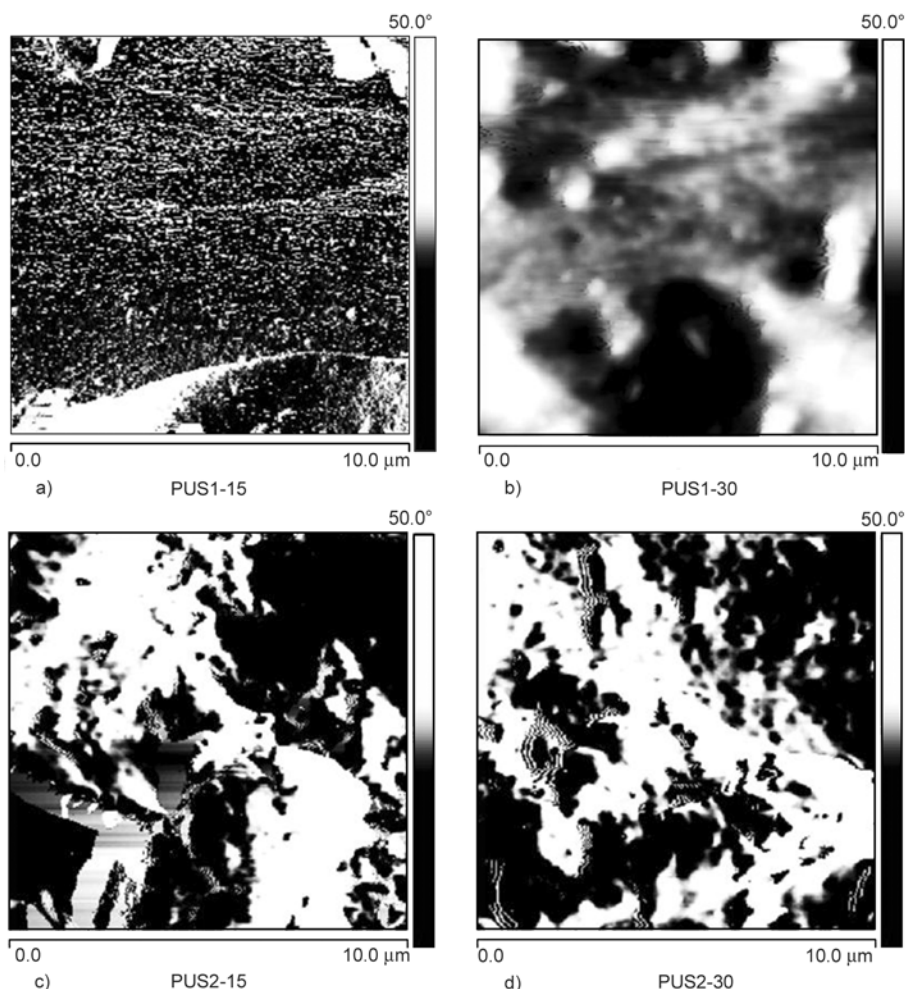


Figure 7. 2D AFM phase images of the fractured surface of the synthesized PUs: (a) PUS1-15, (b) PUS1-30, (c) PUS2-15, (d) PUS2-30

mum at -74 and -67°C for PUS1-15 and PUS1-30 samples, and at -79 and -58°C for PUS2-15 and PUS2-30 samples, respectively, that may be corresponding to the subglass relaxation process (T_2), but this should be studied further. This is probably a consequence of the movement of the part of chain which contains urethane groups connected to the hyperbranched polyester according to the findings of other authors [13]. Due to the steric hindrance, these urethane groups are not involved in the formation of hydrogen bonds and are therefore, more mobile. The samples from the PUS2 series had higher values of T_{gHS} than the samples from the PUS1 series. The presence of terminal ethoxy units in PDMS prepolymer improves miscibility between reactants and, therefore, the PU samples based on EO-PDMS (PUS1 series) had lower T_{gHS} values, and consequently, lower degree of microphase separation. The glass transition temperatures of the hard and soft segments were also determined in DSC thermo-

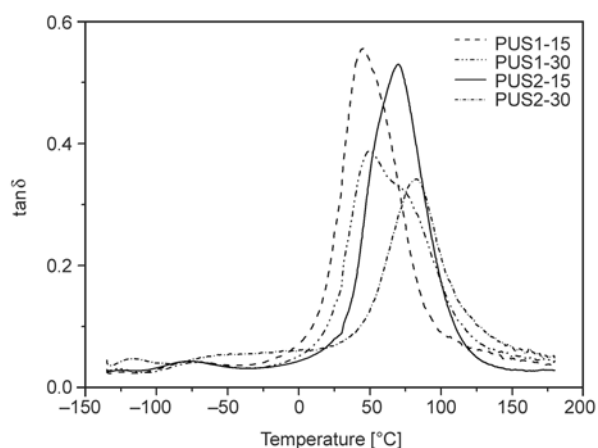


Figure 8. $\tan \delta$ of the synthesized PUs versus temperature

grams of the synthesized PUs (Table 7). The observed trend for T_{gHS} values was consistent with DMTA results. The T_{g} of the PDMS soft segments of the synthesized PUs was between -121 and -125°C . The T_{gSS} values determined as $(\tan \delta)_{\text{max}}$ from DMTA curves are slightly higher than those determined by

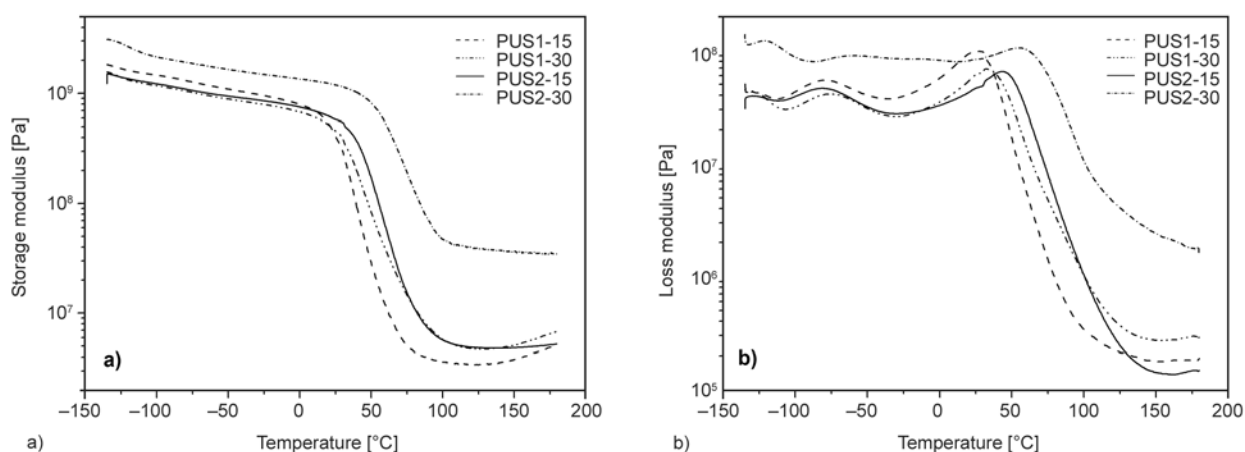


Figure 9. (a) Storage modulus and (b) loss modulus of the synthesized PUs versus temperature

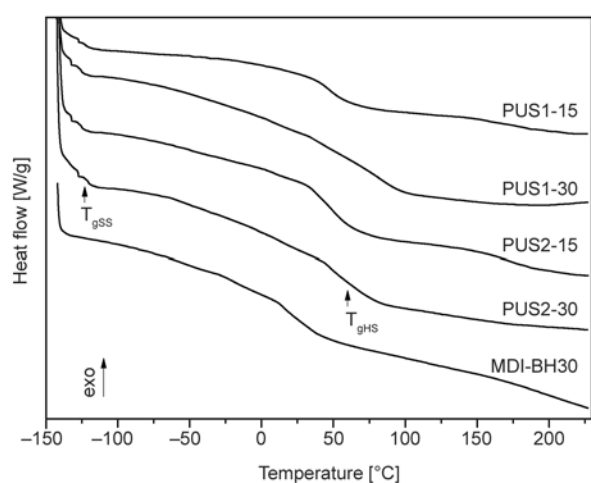


Figure 10. DSC thermograms of the synthesized PUs and control MDI-BH30 sample

DSC. DSC thermograms of the synthesized PUs and control sample, determined from the second heating run, are shown in Figure 10. A T_g value of the control MDI-BH30 sample obtained by DSC analysis was 30°C, which shifted to lower temperature compared with that of the synthesized PUs. The synthesized samples based on PDMS have two T_g s in comparison with the control sample and therefore possess microphase separated structure.

The network homogeneity of each of the PU networks was analyzed by comparing the width of the mechanical loss factor curves [14, 40, 41]. The width of the $\tan \delta$ peak for samples PUS2-15 and PUS2-30 was slightly lower in comparison with PUS1-15 and PUS1-30 samples. The slightly wider peak of $\tan \delta$ obtained for PUS1 samples indicates a less homogeneous distribution of crosslinks than for the samples of PUS2 series.

For PU samples, the storage modulus firstly decreased gradually, and then decreased relatively

fast at temperatures between 20 to 100°C. A rubber elastic plateau was observed at around 120°C for all examined PUs. PU samples based on HP-PDMS had higher G' in the rubbery plateau than the samples based on EO-PDMS (Figure 9), which indicates the higher crosslinking density (Table 7). The results given in Table 7 show that the crosslinking density of PUs based on HP-PDMS was higher, while M_c was lower than values obtained for the EO-PDMS containing PUs. Samples PUS1-30 and PUS2-30 have higher values of the crosslinking density in comparison with PUS1-15 and PUS2-15, and PUS2-30 has the highest crosslinking density of all samples. The reason for higher crosslinking density of PUS1-30 and PUS2-30 samples in comparison with samples PUS1-15 and PUS2-15 may be steric hindrance caused by HBP molecules which is more pronounced in samples with 15 wt% of soft segment because of the greatest amount of BH-30. Therefore, instead of participating in the reaction of crosslinking, $-\text{OH}$ groups of the HBP may be hydrogen bonded. The obtained results also showed that hydroxypropyl terminated PDMS is more efficiently incorporated in the polyurethane networks in comparison with hydroxyethoxy propyl terminated PDMS.

It can be observed (Figure 9a) that the rubbery plateau modulus of the investigated PU networks was higher than values of the order of 10⁶ Pa obtained for other crosslinked PUs based on hydroxybutyl-PDMS [42] and based on poly(propylene oxide) or hyperbranched polyester [14]. Therefore, the incorporation of the PDMS macrodiols into PU networks based on BH-30 as the crosslinker improved the thermomechanical and surface properties of the synthesized PUs.

4. Conclusions

Polyurethane networks based on different PDMS macrodiols and hyperbranched polyester of the third pseudo generation were synthesized using two-step polymerization in solution. The results clearly demonstrated that the type of the PDMS macrodiols incorporated in the PUs influenced the morphology, surface and thermomechanical properties of the synthesized PU networks. DMTA showed that the synthesized PU networks based on EO-PDMS or HP-PDMS have two glass transition temperatures and a microphase separated structure. Microphase separation, where the hard MDI-HBP domains are dispersed in a soft matrix, was also confirmed by SEM and AFM analyses. Better thermomechanical properties, higher crosslinking density, more hydrophobicity and better waterproof properties were obtained for PU samples based on HP-PDMS than for EO-PDMS-based PUs. The surface energy values of the samples based on HP-PDMS were lower than values obtained for the samples based on EO-PDMS. Evaluation of all synthesized PU samples also revealed that their surface energy values were closer to the value obtained for the control sample prepared without PDMS macrodiol and were higher than those of siloxane-urethane coatings and linear PDMS presented in the literature. The obtained results showed the presence of both the hydrophobic PDMS and hydrophilic urethane groups at the surface, giving a slight amphiphilic nature to the surface of the synthesized PUs. The results in this study clearly demonstrate that the synthesis of polyurethanes based on PDMS and hyperbranched polyester leads to the creation of networks with improved surface and thermomechanical properties, which can be easily tailored by changing the type of soft PDMS segment for specific applications.

Acknowledgements

This work was financially supported by the Ministry of Education, Science and Technological Development of the Republic of Serbia (Project No. 172062) and Czech Science Foundation (GACR, Project No. P108/10/0195). The authors thank Prof. Dr Petar Jovančić (Faculty of Technology and Metallurgy, University of Belgrade) for making instruments for contact angle measurements available.

References

- [1] Dodge J.: Synthesis methods in step-growth polymers. Wiley, New Jersey (2003).
- [2] Chattopadhyay D. K., Raju K. V. S. N.: Structural engineering of polyurethane coatings for high performance applications. *Progress in Polymer Science*, **32**, 352–418 (2007).
DOI: [10.1016/j.progpolymsci.2006.05.003](https://doi.org/10.1016/j.progpolymsci.2006.05.003)
- [3] Kazmierczak M. E., Fornes R. E., Buchanan D. R., Gilbert R. D.: Investigations of a series of PPDI-based polyurethane block copolymers. II. Annealing effects. *Journal of Polymer Science Part B: Polymer Physics*, **27**, 2189–2202 (1989).
DOI: [10.1002/polb.1989.090271103](https://doi.org/10.1002/polb.1989.090271103)
- [4] Mishra A. K., Narayan R., Raju K. V. S. N., Aminabhavi T. A.: Hyperbranched polyurethane (HBPU)-urea and HBPU-imide coatings: Effect of chain extender and NCO/OH ratio on their properties. *Progress in Organic Coatings*, **74**, 134–141 (2012).
DOI: [10.1016/j.porgcoat.2011.11.027](https://doi.org/10.1016/j.porgcoat.2011.11.027)
- [5] Mahesh K. P. O., Alagar M., Kumar S. A.: Mechanical, thermal and morphological behavior of bismaleimide modified polyurethane-epoxy IPN matrices. *Polymers for Advanced Technologies*, **14**, 137–146 (2003).
DOI: [10.1002/pat.341](https://doi.org/10.1002/pat.341)
- [6] Rahman M. M., Chun H. H., Park H.: Waterborne poly-siloxane-urethane-urea for potential marine coatings. *Journal of Coatings Technology and Research*, **8**, 389–399 (2011).
DOI: [10.1007/s11998-010-9307-9](https://doi.org/10.1007/s11998-010-9307-9)
- [7] Lee Y-H., Kim E-J., Kim H-D.: Synthesis and properties of waterborne poly(urethane urea)s containing polydimethylsiloxane. *Journal of Applied Polymer Science*, **120**, 212–219 (2011).
DOI: [10.1002/app.33007](https://doi.org/10.1002/app.33007)
- [8] Yilgör I., McGrath J.: Polysiloxane containing copolymers: A survey of recent developments. *Advances in Polymer Science*, **86**, 1–86 (1988).
DOI: [10.1007/BFb0025274](https://doi.org/10.1007/BFb0025274)
- [9] Dvornić P. R., Lenz R. W.: High temperature siloxane elastomers. Hüthing Wepf, Heidelberg (1990).
- [10] Bokobza L., Diop A. L.: Reinforcement of poly(dimethylsiloxane) by sol-gel *in situ* generated silica and titania particles. *Express Polymer Letters*, **4**, 355–363 (2010).
DOI: [10.3144/expresspolymlett.2010.45](https://doi.org/10.3144/expresspolymlett.2010.45)
- [11] Žagar E., Žigon M.: Aliphatic hyperbranched polyesters based on 2,2-bis(methylol)propionic acid – Determination of structure, solution and bulk properties. *Progress in Polymer Science*, **36**, 53–88 (2011).
DOI: [10.1016/j.progpolymsci.2010.08.004](https://doi.org/10.1016/j.progpolymsci.2010.08.004)
- [12] Maji P. K., Bhowmick A. K.: Influence of number of functional groups of hyperbranched polyol on cure kinetics and physical properties of polyurethanes. *Journal of Polymer Science Part A: Polymer Chemistry*, **47**, 731–745 (2009).
DOI: [10.1002/pola.23185](https://doi.org/10.1002/pola.23185)

- [13] Czech P., Okrasa L., Ulanski J., Boiteux G., Mechin F., Cassagnau P.: Studies of the molecular dynamics in polyurethane networks with hyperbranched crosslinkers of different coordination numbers. *Journal of Applied Polymer Science*, **105**, 89–98 (2007).
DOI: [10.1002/app.26106](https://doi.org/10.1002/app.26106)
- [14] Asif A., Shi W., Shen X., Nie K.: Physical and thermal properties of UV curable waterborne polyurethane dispersions incorporating hyperbranched aliphatic polyester of varying generation number. *Polymer*, **46**, 11066–11078 (2005).
DOI: [10.1016/j.polymer.2005.09.046](https://doi.org/10.1016/j.polymer.2005.09.046)
- [15] Vuković J., Pergal M., Jovanović S., Vodnik V.: Crosslinked polyurethanes based on hyperbranched polymers. *Hemijška Industrija*, **62**, 353–359 (2008).
DOI: [10.2298/HEMIND0806353V](https://doi.org/10.2298/HEMIND0806353V)
- [16] Pergal M. V., Džunuzović J. V., Kićanović M., Vodnik V., Pergal M. M., Jovanović S.: Thermal properties of poly(urethane-ester-siloxane)s based on hyperbranched polyester. *Russian Journal of Physical Chemistry A*, **85**, 2251–2256 (2011).
DOI: [10.1134/S0036024411130243](https://doi.org/10.1134/S0036024411130243)
- [17] Džunuzović J. V., Pergal M. V., Jovanović S., Vodnik V. V.: Synthesis and swelling behavior of polyurethane networks based on hyperbranched polymer. *Hemijška Industrija*, **65**, 637–644 (2011).
DOI: [10.2298/HEMIND110902071D](https://doi.org/10.2298/HEMIND110902071D)
- [18] Pergal M. V., Džunuzović J. V., Ostojić S., Pergal M. M., Radulović A., Jovanović S.: Poly(urethane-siloxane)s based on hyperbranched polyester as crosslinking agent: Synthesis and characterization. *Journal of the Serbian Chemical Society*, **77**, 919–935 (2012).
DOI: [10.2298/JSC111013006P](https://doi.org/10.2298/JSC111013006P)
- [19] Džunuzović J. V., Pergal M. V., Poręba R., Ostojić S., Lazić N., Špírková M., Jovanović S.: Studies of the thermal and mechanical properties of poly(urethane-siloxane)s cross-linked by hyperbranched polyesters. *Industrial and Engineering Chemistry Research*, **51**, 10824–10832 (2012).
DOI: [10.1021/ie300927z](https://doi.org/10.1021/ie300927z)
- [20] Džunuzović J. V., Pergal M. V., Poręba R., Vodnik V. V., Simonović B. R., Špírková M., Jovanović S.: Analysis of dynamic mechanical, thermal and surface properties of poly(urethane-ester-siloxane) networks based on hyperbranched polyester. *Journal of Non-Crystalline Solids*, **358**, 3161–3169 (2012).
DOI: [10.1016/j.jnoncrysol.2012.09.013](https://doi.org/10.1016/j.jnoncrysol.2012.09.013)
- [21] Pergal M. V., Džunuzović J. V., Poręba R., Ostojić S., Radulović A., Špírková M.: Microstructure and properties of poly(urethane-siloxane)s based on hyperbranched polyester of the fourth pseudo generation. *Progress in Organic Coatings*, **76**, 743–756 (2013).
DOI: [10.1016/j.porgcoat.2013.01.007](https://doi.org/10.1016/j.porgcoat.2013.01.007)
- [22] Vučković M. V., Antić V. V., Govedarica M. N., Djonlagić J.: Synthesis and characterization of copolymers based on poly(butylene terephthalate) and ethylene oxide-poly(dimethylsiloxane)-ethylene oxide. *Journal of Applied Polymer Science*, **115**, 3205–3216 (2010).
DOI: [10.1002/app.31416](https://doi.org/10.1002/app.31416)
- [23] Malmström E., Johansson M., Hult A.: Hyperbranched aliphatic polyesters. *Macromolecules*, **28**, 1698–1703 (1995).
DOI: [10.1021/ma00109a049](https://doi.org/10.1021/ma00109a049)
- [24] Vuković J.: Synthesis and characterization of aliphatic hyperbranched polyesters. PhD thesis, University of Osnabrück, Germany (2006).
- [25] Pergal M. V., Antić V. V., Govedarica M. N., Goševac D., Ostojić S., Djonlagić J.: Synthesis and characterization of novel urethane-siloxane copolymers with a high content of PCL-PDMS-PCL segments. *Journal of Applied Polymer Science*, **122**, 2715–2730 (2011).
DOI: [10.1002/app.33926](https://doi.org/10.1002/app.33926)
- [26] Pergal M. V., Antić V. V., Tovilović G., Nestorov J., Vasiljević-Radović D., Djonlagić J.: *In vitro* biocompatibility evaluation of novel urethane-siloxane copolymers based on poly(ϵ -caprolactone)-block-poly(dimethylsiloxane)-block-poly(ϵ -caprolactone). *Journal of Biomaterials Science: Polymer Edition*, **23**, 1629–1657 (2012).
DOI: [10.1163/092050611X589338](https://doi.org/10.1163/092050611X589338)
- [27] Pergal M. V., Antić V. V., Ostojić S., Marinović-Cincović M., Djonlagić J.: Influence of the content of hard segments on the properties of novel urethane-siloxane copolymers based on a poly(ϵ -caprolactone)-b-poly(dimethylsiloxane)-b-poly(ϵ -caprolactone) triblock copolymer. *Journal of the Serbian Chemical Society*, **76**, 1703–1723 (2011).
DOI: [10.2298/JSC110307146P](https://doi.org/10.2298/JSC110307146P)
- [28] Marand Ā., Dahlin J., Karlsson D., Skarping G., Dalene M.: Determination of technical grade isocyanates used in the production of polyurethane plastics. *Journal of Environmental Monitoring*, **6**, 606–614 (2004).
DOI: [10.1039/B402775B](https://doi.org/10.1039/B402775B)
- [29] Gindl M., Sinn G., Gindl W., Reiterer A., Tschegg S.: A comparison of different methods to calculate the surface free energy of wood using contact angle measurements. *Colloids and Surfaces A: Physicochemical and Engineering Aspects*, **181**, 279–287 (2001).
DOI: [10.1016/S0927-7757\(00\)00795-0](https://doi.org/10.1016/S0927-7757(00)00795-0)
- [30] van Oss C. J., Good R. J., Chaudhury M. K.: Additive and nonadditive surface tension components and the interpretation of contact angles. *Langmuir*, **4**, 884–891 (1988).
DOI: [10.1021/la00082a018](https://doi.org/10.1021/la00082a018)
- [31] Hwang H-D., Kim H-J.: Enhanced thermal and surface properties of waterborne UV-curable polycarbonate-based polyurethane (meth)acrylate dispersion by incorporation of polydimethylsiloxane. *Reactive and Functional Polymers*, **71**, 655–665 (2011).
DOI: [10.1016/j.reactfunctpolym.2011.03.004](https://doi.org/10.1016/j.reactfunctpolym.2011.03.004)

- [32] Vince J., Orel B., Vilčnik A., Fir M., Vuk A. Š., Jovanovski V., Simončić B.: Structural and water-repellent properties of a urea/poly(dimethylsiloxane) sol-gel hybrid and its bonding to cotton fabric. *Langmuir*, **22**, 6489–6497 (2006).
DOI: [10.1021/la060694a](https://doi.org/10.1021/la060694a)
- [33] Bulacovschi V., Stanciu A., Rusu I., Căilean A., Ungureanu F.: Thermal stability and the behaviour in organic solvents of some poly(ester-siloxane)urethanes. *Polymer Degradation and Stability*, **60**, 487–491 (1998).
DOI: [10.1016/S0141-3910\(97\)00112-2](https://doi.org/10.1016/S0141-3910(97)00112-2)
- [34] Majumdar P., Stafslieen S., Daniels J., Webster D. C.: High throughput combinatorial characterization of thermosetting siloxane–urethane coatings having spontaneously formed microtopographical surfaces. *Journal of Coatings Technology and Research*, **4**, 131–138 (2007).
DOI: [10.1007/s11998-007-9015-2](https://doi.org/10.1007/s11998-007-9015-2)
- [35] Jalbert C., Koberstein J. T., Yilgor I., Gallagher P., Krukoniš V.: Molecular weight dependence and end-group effects on the surface tension of poly(dimethylsiloxane). *Macromolecules*, **26**, 3069–3074 (1993).
DOI: [10.1021/ma00064a012](https://doi.org/10.1021/ma00064a012)
- [36] Wang H. H., Mou J., Ni Y. H., Fei G. Q., Si C. L., Zou J.: Phase behavior, interaction and properties of acetic acid lignin-containing polyurethane films coupled with aminopropyltriethoxy silane. *Express Polymer Letters*, **7**, 443–455 (2013).
DOI: [10.3144/expresspolymlett.2013.41](https://doi.org/10.3144/expresspolymlett.2013.41)
- [37] Jiang H., Zheng Z., Song W., Li Z., Wang X.: Alkoxysilane functionalized polyurethane/polysiloxane copolymers: Synthesis and the effect of end-capping agent. *Polymer Bulletin*, **59**, 53–63 (2007).
DOI: [10.1007/s00289-007-0748-y](https://doi.org/10.1007/s00289-007-0748-y)
- [38] Madhavan K., Reddy B. S. R.: Poly(dimethylsiloxane-urethane) membranes: Effect of hard segment in urethane on gas transport properties. *Journal of Membrane Science*, **283**, 357–365 (2006).
DOI: [10.1016/j.memsci.2006.07.005](https://doi.org/10.1016/j.memsci.2006.07.005)
- [39] Mahoney C. M., Gardella Jr J. A., Rosenfeld J. C.: Surface characterization and adhesive properties of poly(imidesiloxane) copolymers containing multiple siloxane segment lengths. *Macromolecules*, **35**, 5256–5266 (2002).
DOI: [10.1021/ma010353y](https://doi.org/10.1021/ma010353y)
- [40] Chiou B-S., Schoen P. E.: Effects of crosslinking on thermal and mechanical properties of polyurethanes. *Journal of Applied Polymer Science*, **83**, 212–223 (2002).
DOI: [10.1002/app.10056](https://doi.org/10.1002/app.10056)
- [41] Pusztai E., Kenyó Cs., Nagy J., Wagner Ö.: The effect of some disiloxane chain extenders on the thermal and mechanical properties of cross-linked poly(siloxane-urethane)s. *Express Polymer Letters*, **7**, 456–470 (2013).
DOI: [10.3144/expresspolymlett.2013.42](https://doi.org/10.3144/expresspolymlett.2013.42)
- [42] Alexandru M., Cazacu M., Cristea M., Nistor A., Grigoras C., Simionescu B. C.: Poly(siloxane-urethane) crosslinked structures obtained by sol-gel technique. *Journal of Polymer Science Part A: Polymer Chemistry*, **49**, 1708–1718 (2011).
DOI: [10.1002/pola.24602](https://doi.org/10.1002/pola.24602)

Crystallization kinetics and morphology of melt spun poly(ethylene terephthalate) nanocomposite fibers

R. R. Hegde¹, G. S. Bhat^{1*}, B. Deshpande²

¹Department of Materials Science and Engineering, The University of Tennessee, Knoxville TN 37996, USA

²Techmer PM, #1 Quality Circle, Clinton TN 37716, USA

Received 16 March 2013; accepted in revised form 14 June 2013

Abstract. Natural nanoclay closite Na⁺ incorporated melt spun poly(ethylene terephthalate) (PET) fibers were investigated for crystallization kinetics and morphology. Nature of clay dispersion and nanocomposite morphology were assessed using wide angle X-ray diffraction (WAXD) and transmission electron microscopy (TEM). Fiber mechanical properties were measured using single fiber tensile test. Combination of scanning electron microscopy (SEM) and energy dispersive spectroscopy (EDS) was used to investigate the fiber failure mode. Among nanocomposite PET fibers, sample with 1% clay performed better. WAXD and TEM micrographs of the fibers revealed intercalated and delaminated morphology. Size of agglomerate increased with percentage of add-on. SEM surface images showed significant variation in fiber diameter, voids and imperfections. Cross-sections of fractured surfaces revealed the presence of clay agglomerates at failure spots. Nanoclay reinforcement did not incur mechanical property benefits due to increase in voids and agglomerates in fiber section, especially at loading levels higher than one percent.

Keywords: nanocomposites, nanoclay, morphology, poly (ethylene terephthalate)

1. Introduction

Poly (ethylene terephthalate) (PET) is a low cost, engineering polymer that is used for making fibers, films, tapes, pressurized liquid containers and extruded parts. The microstructure and mechanical properties of PET can be significantly controlled by tailoring crystallization rate and degree of crystallinity with use of additives [1–5].

Nanoclay based on montmorillonite is a layered mineral deposit of smectite family extracted from volcanic ash. Unique features of nanoclay additives are; high modulus, its ability to be dispersed in platelet form within polymer matrix, and individual clay particle has very high aspect ratio with surface area of around 600 nanometers square and thickness of only one to a few nanometers. Earlier studies have reported improved properties in the final

products derived by clay loading as low as 0.5 wt% compared to conventional composites with a large amount of fillers [6–11].

Earlier studies report improved mechanical and thermal stability properties [5, 12–14]. In order to see the property benefits, the nanoclay additive has to be uniformly dispersed within the matrix [15]. Based on the extent of dispersion of additives, there are three known morphologies of nanocomposites; exfoliated, intercalated and agglomerated, which are elucidated in our earlier paper [7]. Thermodynamically, the strongly hydrophilic clay and hydrophobic polymers lack attractive enthalpic forces to overcome the electrostatic force which pulls sheets together. The net effect is that the free energy of mixing between clay and polymer is positive, and so the mixing is not thermodynamically favorable.

*Corresponding author, e-mail: gghat@utk.edu

© BME-PT

In melt compounded systems with non-polar olefins, a favorable enthalpic interaction is achieved by addition of ‘compatibilizer’ like maleated polypropylene. Few studies also report organically modified nanoclay additives to increase the spacing between clay layers and achieve better dispersion [16].

There have been few attempts to describe the effect of nanoclay additives on crystallization, thermal and mechanical properties and morphology of PET fibers. Nucleating effect of clay additives in polyester systems has been studied before [17, 18]. Authors have reported two mutually opposite effects; nucleating ability of additive and growth retardation due to lack of diffusion [19]. Up to three times higher crystallization rate has been reported for PET nanocomposites compared to that of pure PET [1]. Compared to the large distinct spherulite in case of pure PET, PET-nanoclay nanocomposites formed small sized spherulites. Detailed crystallization kinetics and influence of clay additives on the spherulite formation is reported in earlier literature [20]. Presence of nanoclay not only promotes nucleation, but the huge surface area for platelet structure supports crystal growth [1, 21].

Earlier studies on mechanical properties give conflicting opinion about the improved mechanical property benefits. Xiao *et al.* [3] reported that the strong interaction between MMT layer and PET chains decreased the degree of orientation and crystallinity. Compared to non-polar olefins it’s relatively easy to disperse nanoclay within the PET matrix due to strong interaction between nanoclay layer and PET molecules. Bizarria *et al.* [4] reported that mechanical properties of PET/organoclay nanocomposites were superior to that of the recycled PET in terms of strength and elasticity modulus. Chang *et al.* [2] produced and characterized PET-organoclay dodecyltriphenylphosphonium-mica hybrid fibers. They found that the strengths of the fibers increased up to a critical clay loading and then properties decreased above that critical clay concentration. Lu and Hay reported that the mechanism of deformation changed from ductile shear yielding to craze-crack growth due to presence of nanoclay [22].

Structure and morphology of polypropylene fiber nanocomposites, nonwoven nanocomposites: spun bond and melt blown nonwovens, has been reported before [7–9]. However, influence of additives on the structure and properties of PET fiber nanocom-

posites, and crystallization kinetics PET nanocomposites is not reported anywhere in detail.

In this research, melt spun PET/Cloisite Na⁺ composite fibers with additive wt% ranging from 1 to 5 wt % were characterized for crystallization kinetics, structure, morphology and mechanical properties.

2. Experimental

2.1. Materials and methods

PET-nanoclay concentrates with nanoclay additive wt% ranging from 1 to 5 wt.% were supplied by Techmer PM (Clinton, Tennessee, USA). PET resin (DAK Americas, Wilmington, NC, USA) had density of 1.35 g/cm³ and intrinsic viscosity of 0.68. The natural nanoclay additives (density 2.86 g/cc, moisture content 4–9%, particle size <25 μm) were purchased by Techmer PM from Southern Clay Products of Gonzales, Texas. Cloisite Na⁺ a natural montmorillonite produced from highly refined bentonite was used for this study. Bentonite is acceptable for use as a direct food substance affirmed as generally recognized as safe by the FDA under 21CFR 184.115 [23].

The filaments were melt spun at 270°C, using a Hills melt spinning unit with 41 round hole die. The spinning conditions were adjusted (speed in range of 220 meters/min (mpm) to 890 mpm, and draw ratio of 4:1) to get consistent filaments without breakage. The composition of fibers is included in Table 1.

2.2. Testing and characterization

2.2.1. Wide angle X-ray diffraction (WAXD)

WAXD scans of the chopped fiber samples were conducted in reflection mode using the Phillips X Pert Pro X-ray diffraction system with CuK_α radiation (45 kV, 40 mA) of wavelength 1.542 Å. Samples were scanned in 2θ range of 2 to 40° and step size of 0.02° for 1 sec at each step.

2.2.2. Transmission electron microscopy (TEM)

Ultra thin sections (less than 70 nm thick) were obtained using a RMC Power tome CRX microtome equipped with diamond knife. Nanocomposite fibers were doped within the epoxy block and the epoxy block with the fibers was used for sectioning. Details of sample preparation is discussed in earlier publications [8, 9]. Specimen temperature was –100°C and Glass knife temperature was set to –103°C.

Sections were mounted on standard 400 mesh Cu grids and TEM images were taken using the Hitachi H-800 Electron Microscope operated at 200 kV.

2.2.3. Single fiber tensile test

Single fiber tensile test was carried out using a Thwing-Albert EJA 1000 (West Berlin, NJ, USA) tensile tester equipped with a 2000 g load cell as per ASTM 3822 [24]. Single fibers taken from various portions of the yarn were pasted on cardboard templates as shown in Figure 1. To avoid jaw-slipping, fibers were glued using epoxy resin and allowed to cure before testing. After mounting the template within the jaws of the tensile tester, template is cut off to test the single fiber only at a gauge length of 2.5 cm at a speed of 2.5 cm/min. Average of 10 readings is reported for tenacity and breaking elongation. Tenacity is defined as the breaking force in grams per denier. Tensile modulus was calculated from the initial region of load-elongation plots up to 2% elongation.

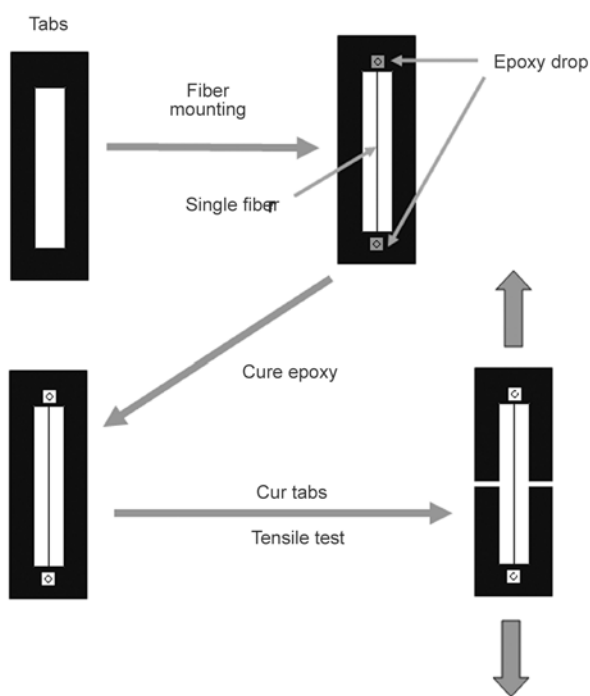


Figure 1. Schematic of sample preparation steps used for the single fiber tensile test

2.2.4. Scanning electron microscopy

Scanning Electron Microscopy (SEM) images of the fiber surface, and tensile failed fiber cross-sections were taken using the Leo 1215 Field emission gun. The samples were gold coated for 10 seconds using

the SPI sputter coater to minimize charging. Image magnification was in the range of 100 to 1700 \times .

2.2.5. Energy dispersive spectrometers (EDS)

The Oxford Pentafet EDS system was used to evaluate chemical composition in failure spots of nanocomposite. ZAF Quantitative method: ZAF (3 iterations) with the system resolution of 127 eV and running Link ISIS software were used for data analysis. Presence of agglomerates at the fiber cross-sections was analyzed using EDS.

2.2.6. Differential scanning calorimetry (DSC)

Thermal analysis was carried out using the Mettler Toledo (Mettler, Columbus, OH, USA) DSC 822e. Samples were heated in the temperature range of 40 to 300 $^{\circ}$ C at a heating rate of 10 $^{\circ}$ C per minute in the N₂ atmosphere, held at 300 $^{\circ}$ C for 10 min and cooled to room temperature at a cooling rate of 20 $^{\circ}$ C per minute. Percentage of crystallinity $X_c\%$, of samples were calculated from enthalpies of crystallization using Equation (1):

$$X_c\% = \frac{\Delta H}{(1 - \phi)\Delta H_{100\%}} \cdot 100 \quad (1)$$

where ΔH is the measured heat of fusion of the sample and $\Delta H_{100\%}$ the heat of fusion of the 100% crystalline PET, taken as 115 J/g for this study and ϕ is the weight fraction of nanoclay additive. For isothermal relative crystallization studies, fiber samples were heated from 40 to 300 $^{\circ}$ C at a heating rate of 50 $^{\circ}$ C/min, held at 300 $^{\circ}$ C for 10 min to erase all previous thermal history, and cooled at the rate of -80 $^{\circ}$ C/min from 300 $^{\circ}$ C to crystallization temperature of 215, 220 and 225 $^{\circ}$ C and held for 20 min at each crystallization temperature. The isothermal crystallization kinetics was analyzed by evaluating degree of crystalline conversion as a function of time at a constant temperature. The relative crystallinity at different crystallization time $X(t)$, was obtained from the ratio of the area of the exotherm up to time t divided by the total exotherm given by Equation (2), where Q_t and Q_{∞} are the heat generated at time t and infinite time, respectively, and dh/dt is the heat flow rate [25]. Assuming that the relative crystallinity increases as a function of time, time-dependent relative crystallinity $X(t)$ was estimated by Avrami Equation (3). The Avrami equation in the simple form represents unimpeded spherical crystal

growth [26]. Equation (3) can be rearranged in double logarithmic form as Equation (4):

$$X(t) = \frac{Q_t}{Q_\infty} = \frac{\int_0^t \left(\frac{dh}{dt}\right) dt}{\int_0^\infty \left(\frac{dh}{dt}\right) dt} \quad (2)$$

$$1 - X(t) = \exp(-Kt^n) \quad (3)$$

$$\log[-\ln(1 - X(t))] = \log K + n \log t \quad (4)$$

From the plot of $\log[-\ln(1 - X(t))]$ versus $\log(t)$, value of n (slope) and K (y-intercept) was determined. In this equation, n is the Avrami exponent which corresponds to nucleation and growth parameter and K is the rate constant that describes the crystallization rate and, t is the crystallization time [27].

3. Results and discussion

WAXD scans of neat nanoclay additives control PET and nano-composite fibers of different clay composition are shown in Figure 2. Nanoclay additives show peak corresponding to (100) plane at 2θ of 6.96° , which correspond to $d_{(100)}$ spacing of 1.26 nm. Nanocomposite fiber WAXD scans do not show any peak corresponding to (100) plane of nanoclay. This disappearance of clay signature in the nanocomposite fiber is due to high shear stress involved in the melt spinning extruder. Similar results were observed in case of polypropylene melt spun fibers [7], melt blown nanocomposites webs [8] and spun bond nanocomposites [9]. Peak at $2\theta = 17.8^\circ$, corresponds to the (010) diffraction plane of the triclinic crystal of PET [28]. Sample PETFC5 showed lower crystallinity in XRD analysis.

TEM micrographs of PETFC1, PETFC2 and PETFC5 are shown in Figures 3a–3i. Micrographs reveal intercalated and delaminated structure of platelets. Fiber cross section showed particle size in range of 200–300 nm for PETFC1, 300 nm to 1 μm for PETFC2 and 1 to 3 μm for PETFC5. Each of these clay platelets at high magnification show significant polymer chain intercalation. Platelets are delaminated and lack the ordered structure.

Micrographs also reveal difference in the clay stack distribution along the fiber cross-section (Figure 3a). Clay stacks near the fiber diameter are smaller fragments whereas the particles at center portion of the fiber are larger and randomly oriented. This differ-

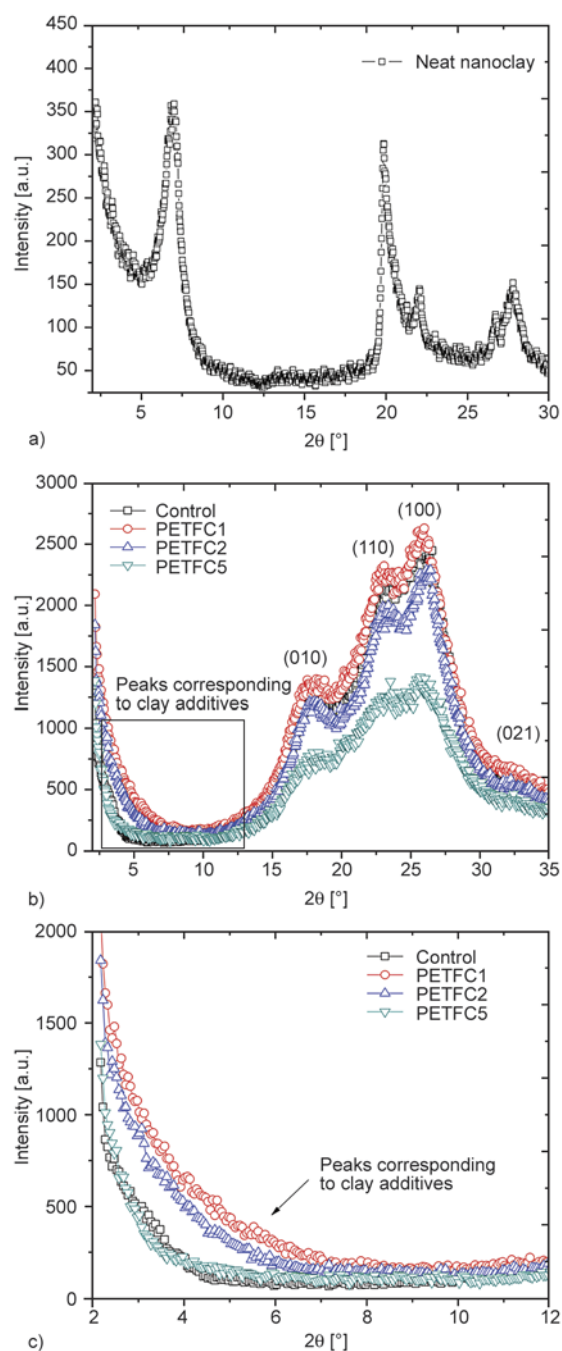


Figure 2. WAXD of (a) nanoclay additive, (b) PET nano-composite fibers, (c) the peak corresponding to (100) plane of nanoclay in lower 2θ range

ence in the additive distribution is due to the ‘wall effect’, an effect which leads to reduction in concentration of suspension adjacent to the solid wall of flow channel. Also, the particles near fiber surface of PETFC1 and PETFC2 have higher polymer chain intercalation compared with ones at the center as shown in Figure 3d, 3e. This higher chain intercalation in conformity to other literature data [8, 9] is due to the higher shear rate experienced by polymer melt near the wall of the spinneret hole.

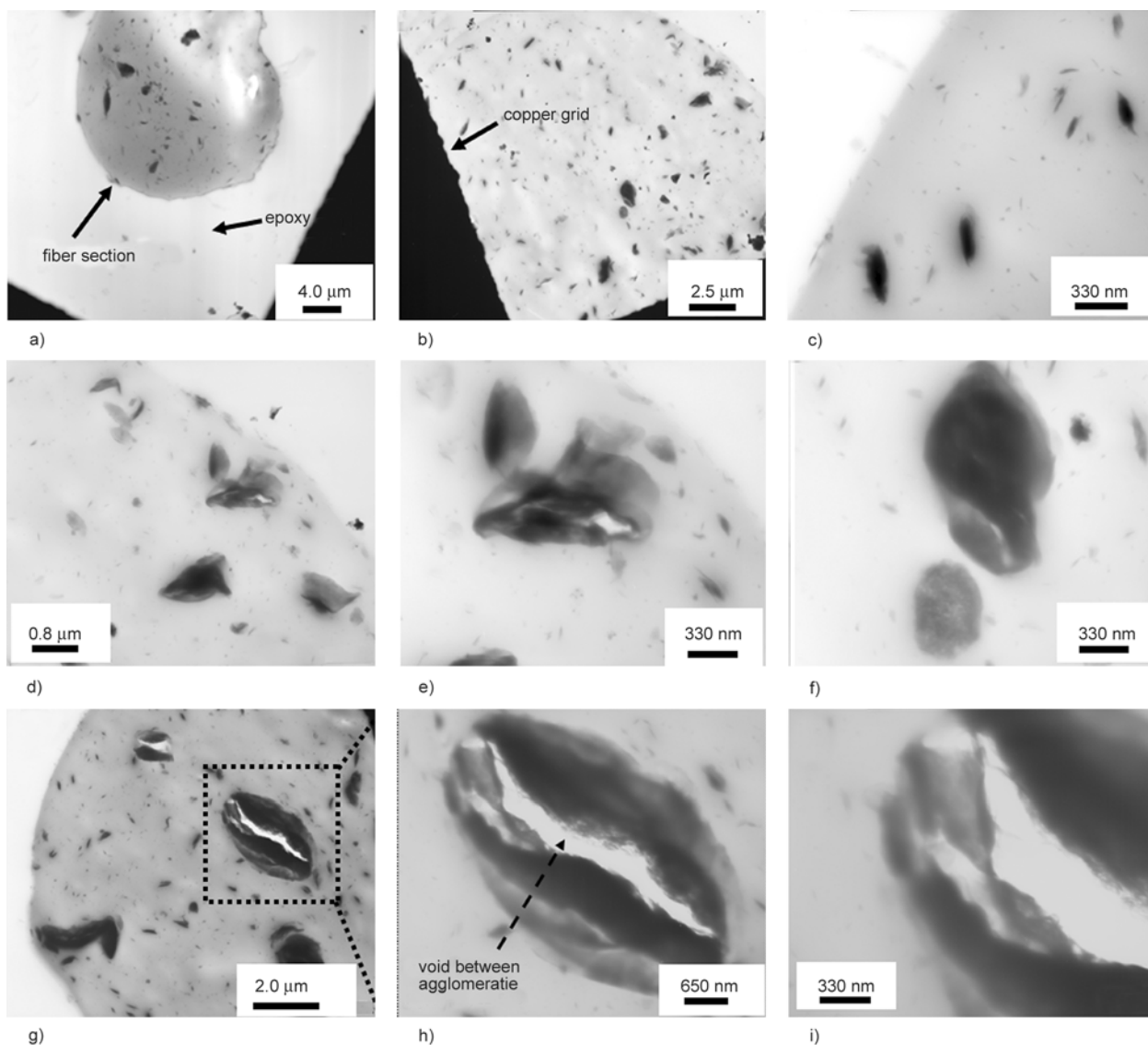


Figure 3. TEM image of a), b), c) PETFC1 (fiber with 1 wt% clay additive), d), e), f) PETFC2 (fiber with 2 wt% clay additive), g), h), i) PETFC5 (fiber with 5 wt% clay additive)

At higher weight %, clay causes increased amount of voids and weak spots within the fiber as observed from TEM images of fiber section (Figure 3 g, 3h and 3i). Most of the micrographs of PETFC5 indicate that the tactoids had voids as shown in Figure 3g. We anticipate this void generation might have developed due to die swell or extrudate swell. Die swell is a phenomenon related to entropy and occurs due to relaxation of polymer melt as it comes out of spinneret orifice. It is well known that there

is strong interaction between PET chains and clay platelets, whereas between clay platelets force is just weak Van der Waals force. Hence, during die swelling, tactoids in PETFC5 might have split open to develop voids as shown in Figures 3g and 3h.

Results of thermal analysis obtained from differential scanning calorimetry (DSC) cooling segment are summarized in Table 1. Onset of crystallization and peak crystallization temperature are 4 to 8°C higher for samples with additives, which indicates

Table 1. DSC thermal analysis results of PET fibers in cooling segment

Sample	Clay wt. [%]	Onset [°C]	Peak [°C]	Heat flow [J/g]	Crystallinity [%]
Control PET	0	221	212	199	44
PETFC1	1	224	221	216	47
PETFC2	2	224	220	215	47
PETFC5	5	224	220	215	48

nucleating ability of nanoclay. Crystallinity wt% of samples is slightly higher for samples with clay additives.

Results of crystallization kinetics are shown in Figure 4. For nanocomposites, crystallinity begins and reaches saturation about 40 seconds before control PET. The relative crystallinity results for samples are shown in Figure 4b. All samples exhibit sigmoid shaped time dependence, which indicates two different stages of crystallization. Initial faster slope change represents nucleation and subsequent slower slope change represents growth and impingement of growing spherulites. Avrami plot is shown in Figure 4c. Avrami exponent n , growth parameter K and half time of crystallization $t_{(1/2)}$ values are listed in Table 2. Avrami exponent n varies from 1 to 3. The n value of 3 corresponds to three dimensional sphere like growth form and lower n value indicates heterogeneous two dimensional rod-like growth forms [26–30]. Compared to control PET, crystallization half time $t_{(1/2)}$ is lower for nanocomposites. Also with increase in temperature, K value decreases and $t_{(1/2)}$ increases which indicates decrease in crystallization rate.

Single fiber tensile strength results are summarized in Figure 5 and Table 3. Nanocomposite fiber strength is less than that of the control PET fiber, which is probably due to non-uniform dispersion and agglomerations even at lower weight percentage add on as shown in TEM micrographs (Figure 3). Among nanocomposite fibers, sample with 1% clay showed higher tenacity but lower elongation compared to sample with 2 wt% clay which indicates excessive variability in all the samples. The variation in properties is due to agglomerates of nanoclay as observed by TEM. Tenacity depends

on the peak stress, which in turn depends on the reinforcing effect and extent of load transfer between nano platelets and matrix, whereas the elongation depends on the extent of drawdown of fibers. Elongation or extent of drawdown depends on the continuity in the molecular network. Even though sam-

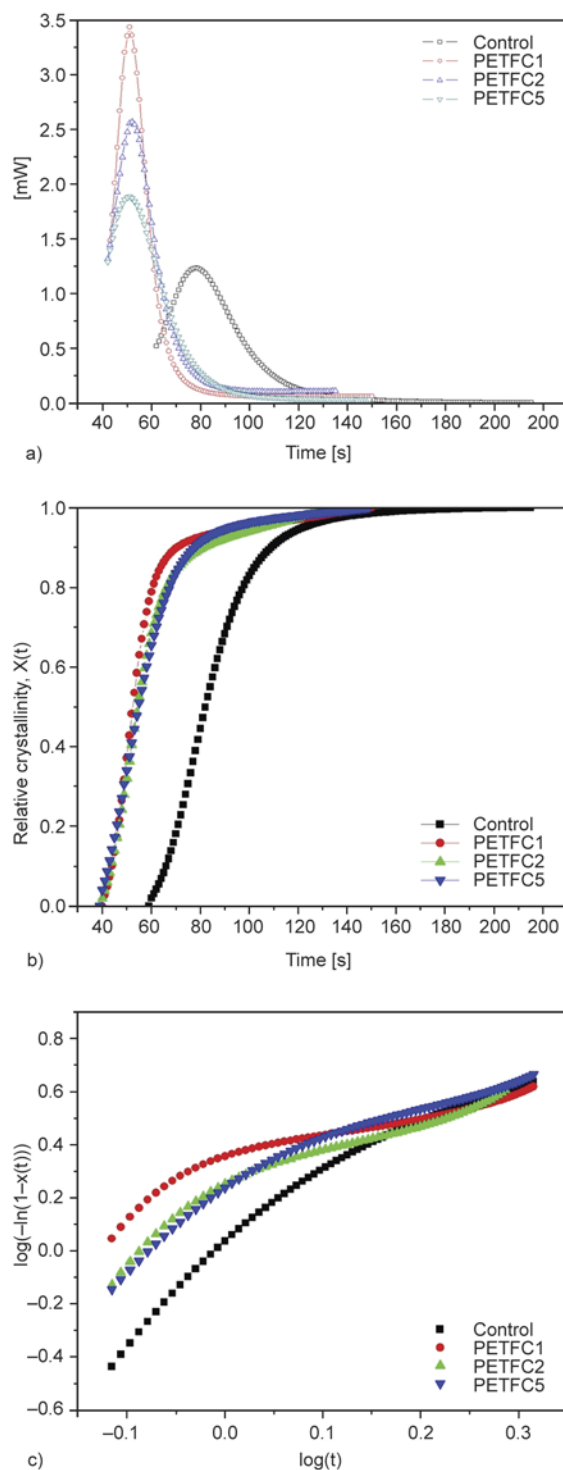


Figure 4. Results from crystallization kinetics study at 215°C (a) degree of crystalline conversion as a function of time, (b) relative crystallinity $X(t)$ for different PET fibers, and (c) Avrami plots

Table 2. The crystallization half time – $t_{(1/2)}$ at 215°C.

Sample	T [°C]	n	K	$t_{(1/2)}$ [s]
Control	215	3.2	0.8	83
	220	3.3	0.3	112
	225	1.1	0.3	198
PETFC1	215	2.3	1.3	53
	220	2.7	0.4	64
	225	0.7	0.4	100
PETFC2	215	2.9	0.8	55
	220	3.4	0.5	62
	225	0.7	0.2	68
PETFC5	215	2.5	1.0	55
	220	2.5	0.2	80
	225	0.7	0.2	110

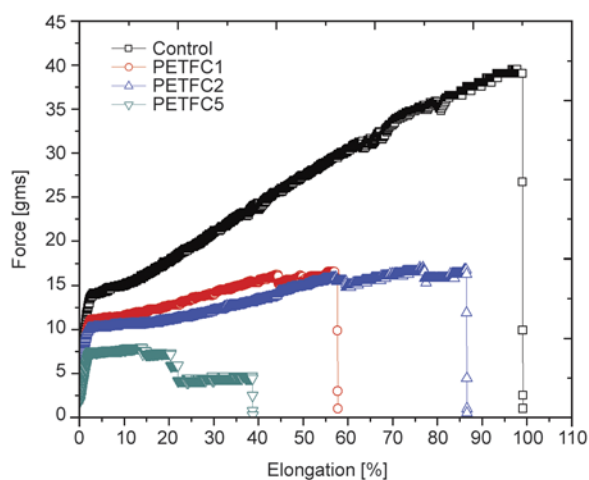


Figure 5. Single fiber tensile test results

ple with 1 wt% clay showed higher tenacity decrease in elongation indicates that the continuity in molecular network is lower compared to control PET fibers.

SEM micrographs of surface of PET fiber PETFC5 with 5 wt % clay sample are shown in Figure 6. It is evident that the fiber diameter varies along the fiber surface. These surface imperfections are due to the protrusion of tactoids near fiber surface as shown in Figure 6a and 6b. Such imperfections contribute to deterioration in tensile properties as observed.

Failure mode was also different for the fibers with 5 wt% clay additives. Fibers showed brittle failure compared to ductile elongation and failure of control PET fibers. SEM and EDS analysis of ($n = 10$) tensile failed PET nanocomposite fiber failure spot

Table 3. Single fiber tensile properties of PET fibers

Sample	Peak load [gms]	Peak elongation [%]	Tenacity [gms/den]
Control PET	35	78	3.6
PETFC1	16	42	1.7
PETFC2	16	57	1.6
PETFC5	10	14	1.0

is shown in Figure 7a and 7b. Agglomerate particulate of 6μ was observed in the failure spot. These particulates were rich in nanoclay chemistry as revealed from EDS scans as shown in Figure 7c.

The structure and morphology of semi crystalline fiber is developed due to the stress-induced crystallization and molecular orientation in semi molten state immediately after extrusion of melt from orifice just before complete solidification. Semi-crystalline polymer fibers or products in molecular level consist of highly ordered crystalline segments, relatively unstable incomplete crystalline regions, transition segments between relatively unstable crystalline and amorphous regions, and unstable oriented amorphous fractions [31]. Mechanical properties like stiffness, strength and elongation exhibited by the fibers depend on the completeness and continuity between these four molecular segments. Transition in different molecular segments in a melt spun fiber subjected to tensile test is illustrated in Figures 8a to 8d.

In the melt spun fibers, additive agglomerates in fiber easily reach order of fiber magnitude [32]. Uniform dispersion of platelets is the key to achieve tensile

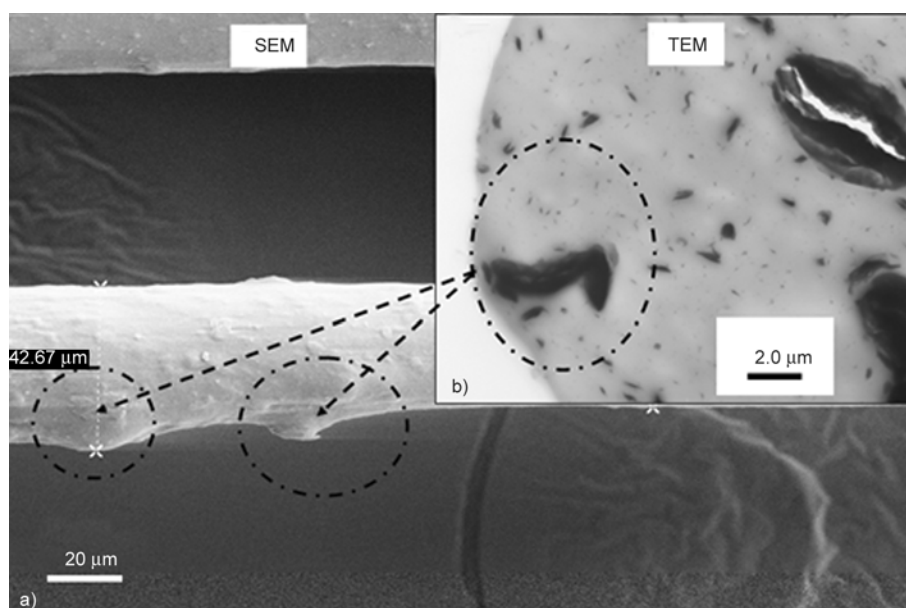


Figure 6. (a) SEM surface image of PETFC5, (b) TEM micrograph of PETFC5 with protrusion of agglomerate out of fiber surface

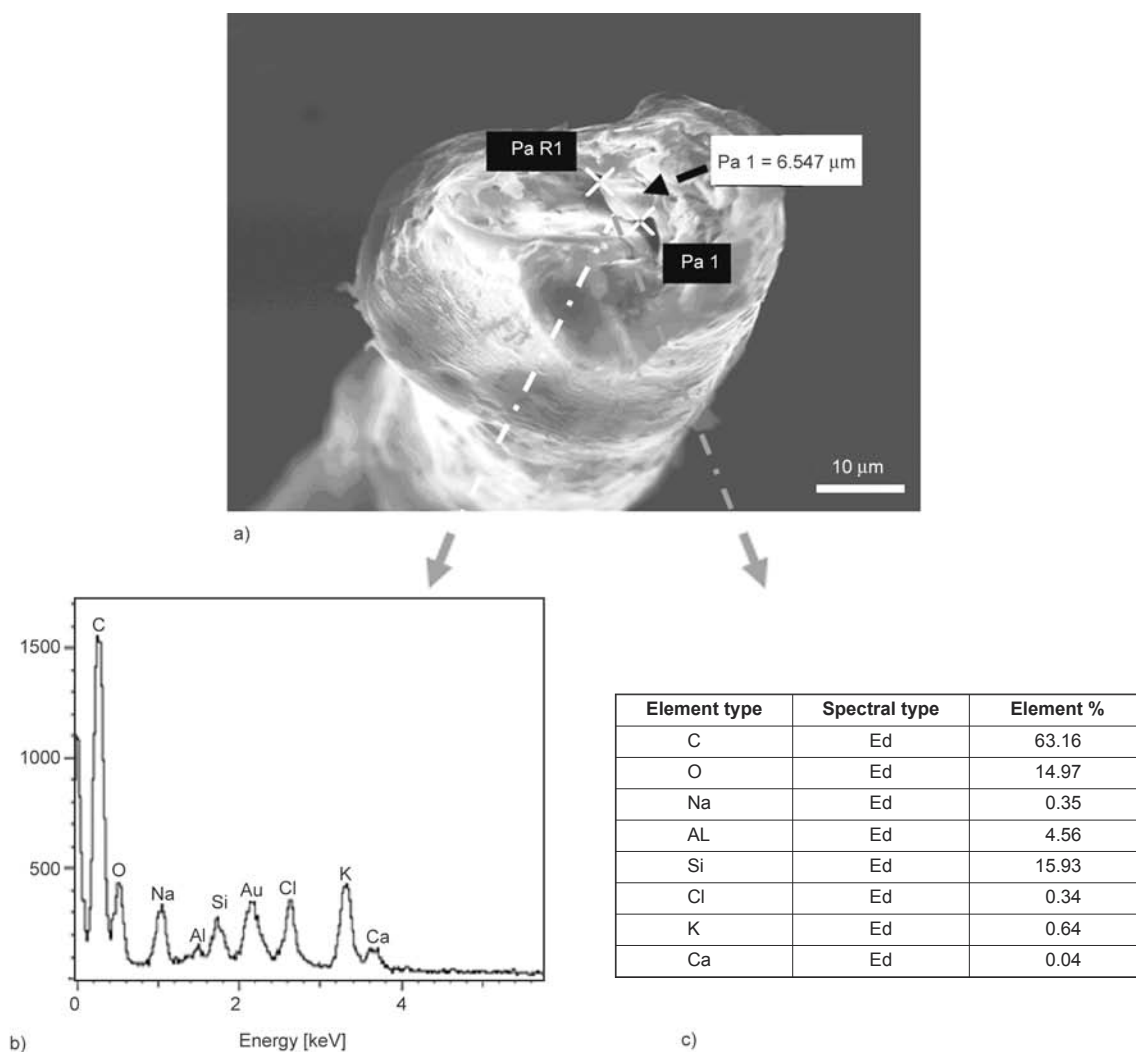


Figure 7. (a) SEM micrograph of PETFC5 failure spot with 5 wt % clay, (b) EDS scan of particulate in failure spot, (c) Elemental composition of particulate

property improvement. At lower weight percentage add on levels, as shown in Figure 8a–8e, if clay platelets are well dispersed in matrix, there will be a good load transfer between filler and matrix, which leads to increase in tensile strength. Also stiffness of fiber increases due to reinforcement in molecular network by high modulus nanoclay additives [13]. At higher weight percentage (Figure 8f), continuity in molecular network is lost because of generation of voids, which act as stress concentrates and lead to a brittle failure [3].

As revealed by SEM and TEM micrographs, fiber cross-section consists of significant tactoids and agglomerates even at lower weight % add on level. TEM micrograph of fiber with 5 wt% clay has larger agglomerates or tactoids as shown in Figure 3g. These tactoids have voids between their plates as shown in enlarged image in Figure 3h.

It is well known that there exist strong interactions between PET and the nano-sized platelets of MMT. The strong interactions between the PET molecule and clay platelets act as crosslink points and reinforce the molecular network. These physical cross linked points make the molecular network more complete and restrict the motion of molecules. Also, having additives may help cool the melt faster compared to control PET due to heat dissipation by nanoclay additives. Faster cooling and the strong interaction with the clay platelets will not allow the molten polymer to go through stress induced orientation and crystallization, which is required for the formation of strong melt spun fibers [14, 33]. In between the clay platelets, force of attraction is only the weak van der Waals forces. So with the applied load, slippage of tactoids leads to voids formation. When subjected to drawing during tensile

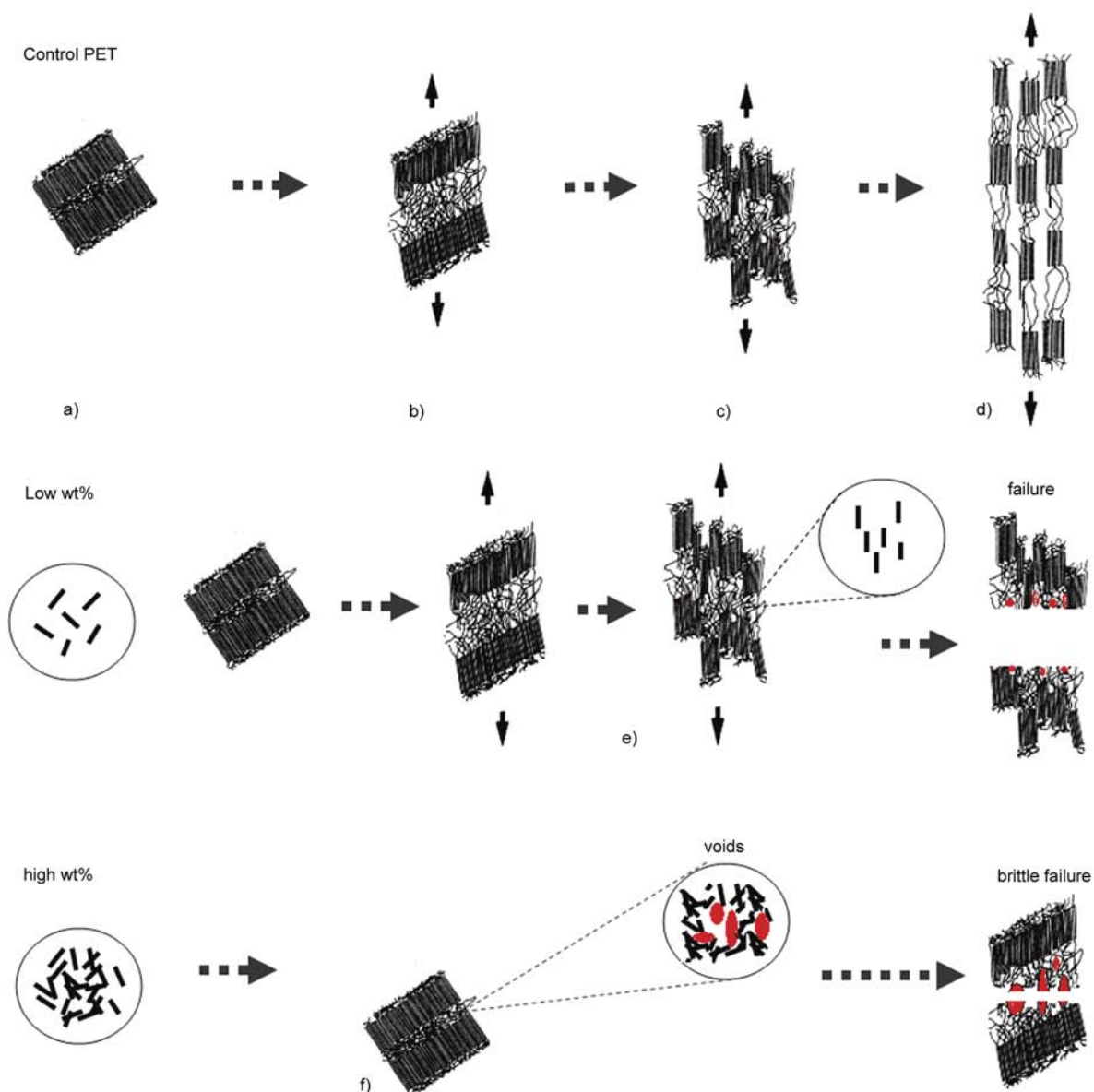


Figure 8. Schematic of morphology and transition in different molecular segments in a melt spun fiber nanocomposite subjected to tensile test, (a) stretching of amorphous segment, (b) shear yielding in crystalline, (c) void formation (d) re-crystallization with orientation (e) in case of fiber with lower weight percentage loading, there is reorientation of platelets in matrix, (f) in case of fiber with higher weight percentage reinforcement, agglomerates lead to amplification of voids and brittle failure

testing, these voids further get enlarged and act as stress concentrates. So, decrease in mechanical properties of fiber with higher wt% clay is due to debonding between platelets in tactoids and defect sites.

It is clear that, nanoclay additives do not always lead to improved mechanical properties in products. Observed behavior is a direct result of non-homogeneous dispersion, and agglomerates formed within the fiber. In melt spun fibers, lower weight percentage add-on levels, uniform dispersion, and process-

ing optimization is necessary to obtain the property benefits from additives.

4. Conclusions

Structure and mechanical properties of nanoclay incorporated melt spun PET nanocomposite fibers were investigated. TEM micrographs revealed presence of tactoids in fibers with additives at all add on levels. Clay platelets showed difference in distribution due to ‘wall effect’ and extent of intercalation at near fiber surface and at fiber center due to higher

shear rate near fiber surface. WAXD scans did not show any peak corresponding to clay platelets because the clay tactoids were delaminated and lacked ordered structure. Extent of dispersion of clay in the fiber matrix could not be detected from WAXD scans. Clay additives acted as nucleating agents and increased the overall crystallization kinetics. Even though nanoclay additives acted as nucleating agents, with accelerated crystallization kinetics, mechanical property benefits were not seen in fibers due to agglomeration. In the case of fibers with clay additives, strength and elongation dropped, and brittle failure mode was observed.

References

- [1] Ke Y., Long C., Qi Z.: Crystallization, properties, and crystal and nanoscale morphology of PET–clay nanocomposites. *Journal of Applied Polymer Science*, **71**, 1139–1146 (1999).
DOI: [10.1002/\(SICI\)1097-4628\(19990214\)71:7<1139::AID-APP12>3.0.CO;2-E](https://doi.org/10.1002/(SICI)1097-4628(19990214)71:7<1139::AID-APP12>3.0.CO;2-E)
- [2] Chang J-H., Mun M. K., Lee I. C.: Poly(ethylene terephthalate) nanocomposite fibers by *in situ* polymerization: The thermomechanical properties and morphology. *Journal of Applied Polymer Science*, **98**, 2009–2016 (2005).
DOI: [10.1002/app.22382](https://doi.org/10.1002/app.22382)
- [3] Xiao W., Yu H., Han K., Yu M.: Study on PET fiber modified by nanomaterials: Improvement of dimensional thermal stability of PET fiber by forming PET/MMT nanocomposites. *Journal of Applied Polymer Science*, **96**, 2247–2252 (2005).
DOI: [10.1002/app.21703](https://doi.org/10.1002/app.21703)
- [4] Bizarria M. T. M., de M. Giraldo A. L. F., de Carvalho C. M., Velasco J. I., d'Ávila M. A., Mei L. H. I.: Morphology and thermomechanical properties of recycled PET–organoclay nanocomposites. *Journal of Applied Polymer Science*, **104**, 1839–1844 (2007).
DOI: [10.1002/app.25836](https://doi.org/10.1002/app.25836)
- [5] Svoboda P., Zeng C., Wang H., Lee L. J., Tomasko D. L.: Morphology and mechanical properties of polypropylene/organoclay nanocomposites. *Journal of Applied Polymer Science*, **85**, 1562–1570 (2002).
DOI: [10.1002/app.10789](https://doi.org/10.1002/app.10789)
- [6] Picard E., Vermogen A., Gérard J-F., Espuche E.: Barrier properties of nylon 6-montmorillonite nanocomposite membranes prepared by melt blending: Influence of the clay content and dispersion state: Consequences on modelling. *Journal of Membrane Science*, **292**, 133–144 (2007).
DOI: [10.1016/j.memsci.2007.01.030](https://doi.org/10.1016/j.memsci.2007.01.030)
- [7] Bhat G., Hegde R. R., Kamath M. G., Deshpande B.: Nanoclay reinforced fibers and nonwovens. *Journal of Engineered Fibers and Fabrics*, **3**, 22–34 (2008).
- [8] Hegde R. R., Bhat G. S.: Nanoparticle effects on structure and properties of polypropylene meltblown webs. *Journal of Applied Polymer Science*, **115**, 1062–1072 (2009).
DOI: [10.1002/app.31089](https://doi.org/10.1002/app.31089)
- [9] Hegde R. R., Bhat G. S.: Nanoparticle effects on the morphology and mechanical properties of polypropylene spunbond webs. *Journal of Applied Polymer Science*, **118**, 3141–3155 (2010).
DOI: [10.1002/app.32304](https://doi.org/10.1002/app.32304)
- [10] Kojima Y., Usuki A., Kawasumi M., Okada A., Fukushima Y., Kurauchi T., Kamigaito O.: Mechanical properties of nylon 6-clay hybrid. *Journal of Materials Research*, **85**, 1185–1189 (1993).
DOI: [10.1557/JMR.1993.1185](https://doi.org/10.1557/JMR.1993.1185)
- [11] Rangasamy L., Shim E., Pourdeyhimi B.: Structure and tensile properties of nanoclay–polypropylene fibers produced by melt spinning. *Journal of Applied Polymer Science*, **121**, 410–419 (2011).
DOI: [10.1002/app.33619](https://doi.org/10.1002/app.33619)
- [12] Yuan Q., Misra R. D. K.: Impact fracture behavior of clay–reinforced polypropylene nanocomposites. *Polymer*, **47**, 4421–4433 (2006).
DOI: [10.1016/j.polymer.2006.03.105](https://doi.org/10.1016/j.polymer.2006.03.105)
- [13] Kawasumi M., Hasegawa N., Kato M., Usuki A., Okada A.: Preparation and mechanical properties of polypropylene–clay hybrids. *Macromolecules*, **30**, 6333–6338 (1997).
DOI: [10.1021/ma961786h](https://doi.org/10.1021/ma961786h)
- [14] Tjong S. C.: Structural and mechanical properties of polymer nanocomposites. *Materials Science and Engineering R: Reports*, **53**, 73–197 (2006).
DOI: [10.1016/j.mser.2006.06.001](https://doi.org/10.1016/j.mser.2006.06.001)
- [15] Alexandre M., Dubois P.: Polymer-layered silicate nanocomposites: Preparation, properties and uses of a new class of materials. *Materials Science and Engineering*, **28**, 1–63 (2000).
DOI: [10.1016/S0927-796X\(00\)00012-7](https://doi.org/10.1016/S0927-796X(00)00012-7)
- [16] Aranda P., Ruiz-Hitzky E.: Poly(ethylene oxide)-silicate intercalation materials. *Chemistry of Materials*, **4**, 1395–1403 (1992).
DOI: [10.1021/cm00024a048](https://doi.org/10.1021/cm00024a048)
- [17] Mayhan K. G., James W. J., Bosch W.: Poly(ethylene terephthalate). I. Study of crystallization kinetics. *Journal of Applied Polymer Science*, **9**, 3605–3616 (1965).
DOI: [10.1002/app.1965.070091110](https://doi.org/10.1002/app.1965.070091110)
- [18] Van Antwerpen F., Van Krevelen D. W.: Influence of crystallization temperature, molecular weight, and additives on the crystallization kinetics of poly(ethylene terephthalate). *Journal of Polymer Science: Polymer Physics Edition*, **10**, 2423–2435 (1972).
DOI: [10.1002/pol.1972.180101211](https://doi.org/10.1002/pol.1972.180101211)
- [19] Kang X., He S., Zhu C., Wang L., Lü L., Guo J.: Studies on crystallization behaviors and crystal morphology of polyamide 66/clay nanocomposites. *Journal of Applied Polymer Science*, **95**, 756–763 (2005).
DOI: [10.1002/app.21257](https://doi.org/10.1002/app.21257)

- [20] Hegde R. R., Spruiell J. E., Bhat G. S.: Different crystallization mechanisms in polypropylene–nanoclay nanocomposite with different weight percentage of nanoclay additives. *Journal of Materials Research*, **27**, 1360–1371 (2012).
DOI: [10.1557/jmr.2012.37](https://doi.org/10.1557/jmr.2012.37)
- [21] Jimenez G., Ogata N., Kawai H., Ogihara T.: Structure and thermal/mechanical properties of poly (ϵ -caprolactone)-clay blend. *Journal of Applied Polymer Science*, **64**, 2211–2220 (1997).
DOI: [10.1002/\(SICI\)1097-4628\(19970613\)64:11<2211::AID-APP17>3.0.CO;2-6](https://doi.org/10.1002/(SICI)1097-4628(19970613)64:11<2211::AID-APP17>3.0.CO;2-6)
- [22] Lu X. F., Hay J. N.: Isothermal crystallization kinetics and melting behaviour of poly (ethylene terephthalate). *Polymer*, **42**, 9423–9431 (2001).
DOI: [10.1016/S0032-3861\(01\)00502-X](https://doi.org/10.1016/S0032-3861(01)00502-X)
- [23] Code of Federal Regulations, Food and Drug Administration: 21CFR 184.1155: Bentonite. (2012).
- [24] ASTM D3822: Standard test method for tensile properties of single textile fibers (2007).
- [25] Weng W., Chen G., Wu D.: Crystallization kinetics and melting behaviors of nylon 6/foiled graphite nanocomposites. *Polymer*, **44**, 8119–8132 (2003).
DOI: [10.1016/j.polymer.2003.10.028](https://doi.org/10.1016/j.polymer.2003.10.028)
- [26] Mucha M., Królikowski Z.: Application of DSC to study crystallization kinetics of polypropylene containing fillers. *Journal of Thermal Analysis and Calorimetry*, **74**, 549–557 (2003).
DOI: [10.1023/B:JTAN.0000005193.66789.ea](https://doi.org/10.1023/B:JTAN.0000005193.66789.ea)
- [27] Avrami M.: Kinetics of phase change. I General theory. *Journal of Chemical Physics*, **7**, 1103–1112 (1939).
DOI: [10.1063/1.1750380](https://doi.org/10.1063/1.1750380)
- [28] Sharples A.: Introduction to polymer crystallization. St Martin's Press, New York (1966).
- [29] Schultz J. M.: Polymer crystallization. Oxford University Press, Washington (2001).
- [30] Jiang X. L., Luo S. J., Sun K., Chen X. D.: Effect of nucleating agents on crystallization kinetics of PET. *Express Polymer Letters*, **1**, 245–251 (2007).
DOI: [10.3144/expresspolymlett.2007.37](https://doi.org/10.3144/expresspolymlett.2007.37)
- [31] Friedrich K., Karsch U. A.: Failure processes in particulate filled polypropylene. *Fibre Science and Technology*, **18**, 37–52 (1981).
DOI: [10.1016/0015-0568\(83\)90049-0](https://doi.org/10.1016/0015-0568(83)90049-0)
- [32] Ergungor Z., Cakmak M., Batur C.: Effect of processing conditions on the development of morphology in clay nanoparticle filled nylon 6 fibers. *Macromolecular Symposia*, **185**, 259–276 (2002).
DOI: [10.1002/1521-3900\(200208\)185:1<259::AID-MASY259>3.0.CO;2-0](https://doi.org/10.1002/1521-3900(200208)185:1<259::AID-MASY259>3.0.CO;2-0)
- [33] Hegde R. R., Bhat G. S., Deshpande B.: Morphology and properties of nylon 6 blown films reinforced with different weight percentage of nanoclay additives. *International Journal of Polymer Science*, 959035/1–959035/14 (2012).
DOI: [10.1155/2012/959035](https://doi.org/10.1155/2012/959035)

Metal adsorption behavior of 2,4-dinitrophenyl hydrazine modified polyacrylonitrile nanofibers

S. Jitjaicham¹, P. Kampalanonwat², P. Supaphol^{1*}

¹The Petroleum and Petrochemical College, Chulalongkorn University, Phyathai Road, Pathumwan, 10330 Bangkok, Thailand

²Rajamangala University of Technology Rattanakosin, Thanon Phutthamonthon Sai 5 Salaya Phutthamonthon Nakhon 73170 Pathom, Thailand

Received 22 March 2013; accepted in revised form 18 June 2013

Abstract. Electrospun polyacrylonitrile nanofiber mats (es-PAN nanofiber mats) were surface modified by 2,4-dinitrophenyl-hydrazine (2,4-DNPH) to yield the metal ion adsorption material (es-PAN-DNPH nanofiber mats) and were investigated their adsorption behaviors. Functional modification of the es-PAN nanofiber mats and conventional polyacrylonitrile fibers (c-PAN fibers) were prepared by using 4% (w/v) of 2,4-DNPH in 1,2-ethandiol at 110°C for 6 h to obtained c-PAN-DNPH fibers. The average diameter of the es-PAN-DNPH nanofiber mats was 0.25 μm , which was comparatively smaller than the es-PAN precursor. Their functional groups were confirmed by Fourier transform infrared spectroscopy (FT-IR) and their adsorption behaviors to trace Ag(I), Bi(III), Ga(III), and In(III) from aqueous solutions and were investigated by the induced couple plasma technique. The FT-IR spectra showed the existence of $\text{NN}=\text{C}-\text{NHNH}-$, $\text{O}=\text{C}-\text{NHNH}-$, and $-\text{NO}_2$ functional groups for metal complexes. The adsorption capacities of the obtained es-PAN-DNPH were 7.14 to 36.36% higher than those of c-PAN-DNPH fibers. All adsorption plots onto es-PAN-DNPH nanofiber mats and c-PAN-DNPH fibers followed the Langmuir isotherm and indicated monolayer adsorption characteristics.

Keywords: nanomaterials, electrospinning, polyacrylonitrile (PAN)

1. Introduction

Because of current environmental awareness, trace element contaminants in natural water and discharged industrial effluents have been monitored to determine the accepted quantities [1]. Practices in water purification or waste water treatment are based on ion-exchange resins and fibers. The ion-exchange resins often contain specific functional ligands such as iminodiacetic acid (IDA) [2–4], amino-phosphonic acid [5], and amidoxime [6–9], which can readily react with heavy metal ions to form stable coordinate covalent bonds [4]. Fibrous ion-exchangers are characterized by a high specific surface site, good kinetic properties, and a ready-made structure of a variety of fibers for different fabrications [10,

11]. Most acrylonitrile-based synthetic fiber is made by reactions with specific aqueous reagents – 2-aminoimidazole [12], aminourea [13], 2,4-dinitrophenylhydrazine [14], phenylhydrazine [15], and ethylenediamine [16] – to yield polyfunctional fibers for pre-concentration and separation of trace metal ions. Polymers based on the acrylonitrile group present reactive pendant cyano groups which can readily be modified by different kinds of reagents through nucleophilic addition and cyclo addition reactions [9]. A variety of chemically active textile materials based on polypropylene (PP) and polyacrylic have been developed for ion-exchange applications and under the registered trademark of FIBAN [17]. Additionally, Dominguez *et al.* [10] synthesized polyvinyl

*Corresponding author, e-mail: pitt.s@chula.ac.th
© BME-PT

alcohol mercaptyl fibers coated on fiberglass non-woven mats for removing arsenite (As^{3+}) from water; Liao *et al.* [18] prepared an affinity membrane system on the basis of condensed tannins and natural collagen fiber membranes and investigated the adsorption-desorption behaviors of UO_2^{2+} . Nishiyama *et al.* [19] also prepared a chelated polyethylene porous hollow-fiber membrane containing an iminodiethanol (IDE) group whereas Yuan *et al.* [20] successively applied electrospun metal oxide- TiO_2 nanofiber for elemental mercury removal from flue gas. Recently several researchers have utilized electrospun fibrous mat for ion removal [20–26].

The electrospun fibrous material is prepared by a simple method, namely electrostatic spinning technique. This electrospinning technique has proven to be relatively easy, shows adaptability, and versatility to fabricate non-woven fibrous mats with different forms of fibers- single fibers, hollow fibers, and sheath-core fibers [27–29]. Various polymers have been effectively electrospun under optimal conditions, which vary from polymer to solution properties, processing parameters, and ambient parameters. The electrospun nanofiber web contains porous structures with high porosity, inter-connectivity, micro interstitial spaces and a large surface-to-volume ratio. Potential applications for the electrospun fibers range from material science and technology applications to life science and clinical medicine applications, environmental engineering applications to energy conservation, and biotechnology to defense and security applications where the high ratio of the surface area to mass is of primary importance [27, 28, 30]. The introduction of specific functional groups onto the electrospun nanofibers and composite nanofibers have been gaining attention for the removal of specific matters from aqueous solutions [20, 22, 31–33]. During the electrospinning process, a polymer droplet at the open end of a capillary is subjected to an electric field. Under applied electric field, the charge induced on the liquid surface causes reciprocal charge repulsion and subsequently destabilizes the pendant drop of polymer. Thus the rounded meniscus of the polymer droplet at the tip of the aperture elongates into a conical shape known as Taylor's cone [34]. At the critical electric field a repulsive electric force rises above the surface tension of the polymer. A charged jet of polymer is ejected from the apex of Taylor's

cone and travels to a grounded collector. While the jet stream travels through the atmosphere, evaporation of solvent takes place leading to the deposition of solid polymer fibers on the collector [35]. Stretching and elongation of charged streams into a straight jet arises from gravitational, electrostatic, and Coulombic repulsion forces; entanglement of the polymer chains, surface tension, and drag forces prevent the jet from breaking up [36]. As a result, the electrically charged jet travels in a straight flight for a short distance before bending and splitting into ultrafine fibers, which randomly deposit in nonwoven patterns [37].

In the present study, electrospun poly(acryldinitrophenylamidrazone-dinitro acrylphenylhydrazine) nanofibers mat (es-PAN-DNPH nanofiber mats) were prepared by chemical modification of the electrospun polyacrylonitrile (es-PAN), and conventional polyacrylonitrile (c-PAN) with 2,4-dinitrophenylhydrazine (DNPH) through a one-step process [14]. The es-PAN-DNPH chelating nanofiber mats possessed a large surface to volume mass. The functional groups in the fiber were verified by Fourier transform infrared spectroscopy (FT-IR) and fiber morphology was depicted by the scanning electron microscope (SEM). Inductively coupled plasma spectrometry (ICP) was employed to determine the adsorption capacities for the Ag(I), Bi(III), Ga(III), and In(III) ions, and their adsorption isotherms were also investigated. The recovery factors and adsorption kinetic behaviors of both the es-PAN-DNPH nanofiber mats and c-PAN-DNPH fibers were compared.

2. Experimental

2.1. Materials and preparation

Commercial grade of PAN fibers was obtained from Thai Acrylic Fibre Co., Ltd [conventional textile fiber, with diameters of individual fibers = $13.7 \pm 2.7 \mu\text{m}$, containing acrylonitrile monomer and methylacrylate comonomer (91.4:8.6 wt%) with M_w 55,500 g/mol]. All reagents used throughout the experiments were analytical-reagent grade without further purification. A mixed standard stock solution containing Ag, Bi, Ga, and In ions, 100 ppm each, was prepared by adding 10 mL of 1000 ppm mixed standard ion solution and diluting to 100 mL with distilled water.

2.2. Electrospinning set-up for producing es-PAN nanofiber mats

The electrospinning set-up in this work was basically similar to earlier studies [38]. A polymer solution, contained in a 10 mL standard glass syringe with a blunt-end stainless steel needle (gauge no. 20; OD 0.91 mm), was used as a nozzle. The spinning geometry was 45° from the horizontal baseline. A positive polarity electrode of a power supply (Gamma High Voltage Research D-ES30P-5W DC) was connected to the nozzle. The ground electrode was connected to the collective target- a rotating cylinder (OD 15 cm, width 15 cm, ~40–50 rpm) wrapped with aluminum foil. Polyacrylonitrile in dimethylformamide solution (10 wt%) was prepared for electrospinning under fixed processing parameters of 15 kV of applied voltage, a 20 cm collecting distance and 48 hours of continuous spinning time.

2.3. Preparation of PAN-DNPH fibers and nanofiber mats

The preparation of PAN-DNPH fiber involved the conversion of the nitrile groups presented in the PAN fiber to the DNPH groups by using 2,4-DNPH as described by Chang *et al.* [14]. A 0.5 g piece of es-PAN nanofiber mats or c-PAN fibers were immersed in a flask containing 50 mL of 4 % (w/v) of 2,4-DNPH in 1,2-ethandiol solution and sealed. The mixture was placed in a temperature/time-controlled shaker bath and heated to 110°C and held there for 6 h. After the reaction complete, the product was extracted with absolute alcohol to remove free agents, then washed with distilled water until neutral (pH 7.0) and dried in an oven (60°C, overnight). The reaction is depicted in Figure 1.

2.4. Characterization of es-PAN and es-PAN-DNPH chelating nanofiber mats

The morphology of the obtained nanofiber mats were investigated using a JEOL JSM-6400 scanning electron microscope (SEM) and SemAfore 4.0 software. The functional groups of the nanofiber mats were characterized by a FT-IR spectroscopy (Perkin-Elmer Spectrum 100 and Spectrum software) at a resolution of 4 cm⁻¹ and a wavenumber range of 4000 to 650 cm⁻¹. The adsorption capacities of es-PAN-DNPH to Ag, Bi, Ga, and In ions were determined by an inductively coupled plasma atomic emission spectrometer (ICP-AES, PerkinElmer Plasma-1000).

2.5. Effect of initial pH on metal ions adsorption onto es-PAN-DNPH chelating nanofiber mats

The mixed standard stock solutions containing certain metal ions (Ag, Bi, Ga, and In ions) were adjusted to pH 2–6, and pH 4.5 with 0.1 M HCl. Then effect of the initial pH on metal ions adsorption were investigated by placing 30 mg of es-PAN-DNPH mat in each bottle containing 10 mL of a 100 ppm mixed standard stock solution at various pH ranges. The mixtures were shaken at 30°C for 24 hours in a shaker bath with a shaker speed of 100 rpm. The amounts of Ag, Bi, Ga, and In ions adsorbed onto the es-PAN-DNPH nanofiber mats were verified from the initial and final concentrations of the metal ions in the aqueous solutions. The residual concentration of Ag, Bi, Ga, and In ions in the solutions were determined by ICP spectrometry, and the adsorption capacity [mg/g] of es-PAN-DNPH to Ag, Bi, Ga, and In ions were calculated using Equation (1) [35]:

$$q = \frac{(C_0 - C_e)V}{M} \quad (1)$$

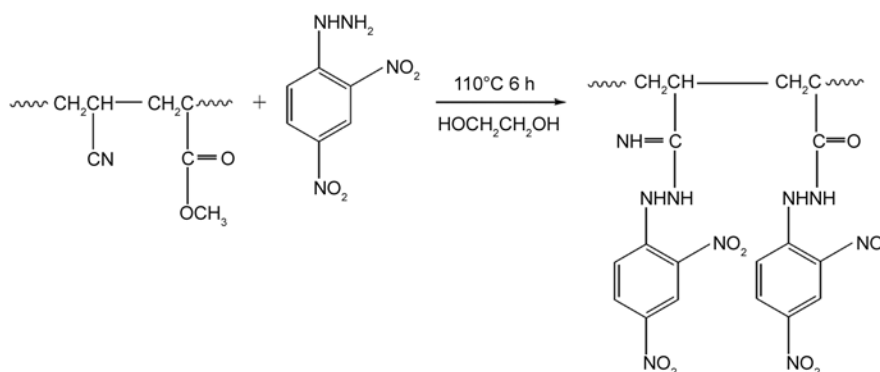


Figure 1. Reaction of es-PAN with 2,4-DNPH to produce poly(acryldinitrophenyl amidrazone-dinitroacrylphenylhydrazine)

where q is the amount adsorbed [mg/g], C_0 is the initial metal-ion concentration [mg/L], C_e is the equilibrium metal-ion concentration [mg/L], V is the solution volume [L], and t is the amount of adsorbent used [g].

2.6. The recovery factors, adsorption kinetics and equilibrium isotherm of metal ions onto PAN-DNPH fibers and nanofiber mats

Dried samples of PAN-DNPH fibers or nanofiber mats (0.1 g) were shaken in 20 mL mixed standard metal ions stock solution (containing 200 ppm of Ag, Bi, Ga, and In ions each) by the batch technique for different time durations at 30°C for 24 hours. The rate constant of adsorption was calculated using Equation (2):

$$-\ln(1 - F) = Kt \quad (2)$$

where F is q_t/q_e and q_e is the saturation adsorption capacity [mg/g], q_t is the adsorption capacity at t min [mg/g], K is the rate constant.

Equilibrium adsorption isotherms were also studied as a function of the concentration of the metal ion stock solutions (20–300 ppm of Ag, Bi, Ga, and In ions each) at 30°C for 24 hours. After equilibration, the concentrations of the different metal ions in the solutions were determined by ICP spectrometer. The adsorption equilibrium [mg/g] of PAN-DNPH to Ag(I), Bi(III), Ga(III), and In(III) ions were analyzed according to the Langmuir adsorption isotherm Equation (3) as follows:

$$\frac{C_e}{q_e} = \frac{1}{K_L q_m} + \frac{C_e}{q_m} \quad (3)$$

where q_e is the equilibrium quantity of the metal adsorbed on the PAN-DNPH chelating fiber [mg/g], C_e is the equilibrium concentration [mg/L], and q_m and K_L are the maximal adsorption capacity of the metal ions on the adsorbent [mg/g] and the adsorption equilibrium constant [mL/mg], respectively. The recovery factor of each metal ion is calculated with Equation (4) [6]:

$$\%R = \frac{C_a}{C_0} \cdot 100 \quad (4)$$

where $\%R$ is the recovery factor, C_a , the amount of metal ion adsorbed, is calculated from the differ-

ence between the initial concentration (C_0) and the residual concentration at equilibrium (C_e).

3. Results and discussion

PAN-DNPH chelating fiber synthesized from PAN fibers was effectively used for enrichment and separation of traces of metal ions from solution samples.

3.1. Characterization of es-PAN and es-PAN-DNPH chelating nanofiber mats

The FT-IR spectra (Figure 2) of es-PAN nanofiber mat exhibits characteristic bands of nitrile (2243 cm^{-1}), carbonyl (1732 cm^{-1}), and ether (~ 1201 and $\sim 1172\text{--}1071 \text{ cm}^{-1}$) groups; carbonyl and ether bands came from the methylacrylate comonomer [31]. The FT-IR spectra of es-PAN-DNPH shows all the characteristic bands of the functional groups of es-PAN with additional peaks around 3400 to 3200 cm^{-1} (the stretching vibration of NH, =NH or Ar-NH), 1539 cm^{-1} [the asymmetric stretching vibration of $\text{NO}_2(\text{Ar})$], 1520 cm^{-1} (the rocking bending vibration of =NH), 1223 cm^{-1} (the stretching vibration of C-N, or N-C=O), 923 cm^{-1} (the twisting bending vibration of NH or =NH), and 835 cm^{-1} (the bending vibration of C- NO_2), respectively [14]. The intensity of the nitrile (2243 cm^{-1}) and carbonyl (1732 cm^{-1}) peaks of es-PAN decreased with the introduction of dinitrophenylhydrazine by chemical treatment of the acrylonitrile and methylacrylate groups. From the FT-IR spectra of the es-PAN-DNPH nanofiber mats, the introduction of DNPH groups onto es-PAN nanofiber mats was confirmed.

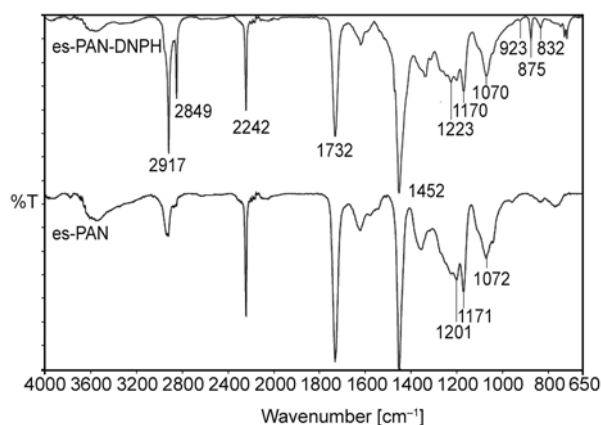


Figure 2. The FT-IR spectra of the es-PAN, and es-PAN-DNPH chelating nanofiber

3.2. Morphologies of the es-PAN and es-PAN-DNPH nanofiber mats

Under the applied electrospinning set-up, smooth continuous fiber webs were obtained with the diameter of the fibers ranging from 0.31 to 0.49 μm (Figure 3a). The surface of the es-PAN-DNPH nanofiber mats were still smooth, similar to those of the original es-PAN, but the average diameter of the obtained es-PAN-DNPH nanofiber mats were 0.25 μm (0.16 to 0.29 μm), which was a \sim 40% reduction (Figure 3b). This reduction in diameter was a consequence of the high temperature treatment resulting in the shrinking of fiber diameter [39]. The es-PAN-DNPH were used as adsorption media by immersing them in a mixed metal ion standard solution for 24 h, the webs shrunk and become denser. However, the average fiber diameter of the es-PAN-DNPH after metal solution adsorption was 0.23 μm (0.15 to 0.34 μm) which was comparable to their precursors (Figure 3c).

3.3. Effect of initial pH on metal ions adsorption onto es-PAN-DNPH chelating nanofiber mats

DNPH modified-PAN showed relatively high recoveries (more than 92%) of trace metal ions (Au, Ru, In, Bi, Zr, V, Ga, and Ti ions) at pH 4–5 [14]. Thus, the pH range of 2–6 and pH 4.5 were employed to study the effect of the initial pH on the adsorption of Ag(I), Bi(III), Ga(III), and In(III) onto the es-PAN-DNPH chelating nanofiber mats. Due to the protonation and deprotonation properties of the functional groups in the es-PAN-DNPH, Figure 4 shows that the initial pH effects the adsorption properties of the es-PAN-DNPH in a slightly different manner. In most cases, the adsorption amounts were small at $<$ pH 4, then increasing to \sim pH 4.5. At pH values higher than 5, the adsorption of Ag(I), Ga(III), and In(III) decreased, whereas that of Bi(III) continuously increased to pH 6. At pH 2, H^+ from the solution could readily occupy the surface of es-PAN-DNPH, resulting in a repulsive barrier to the metal cations; thus, small amounts of metal ions were adsorbed. At pH 4 the metal adsorption increased considerably because the attraction between the positive charges of the metal ions and the lone-pair electrons of the nitrogen ligands overcame the

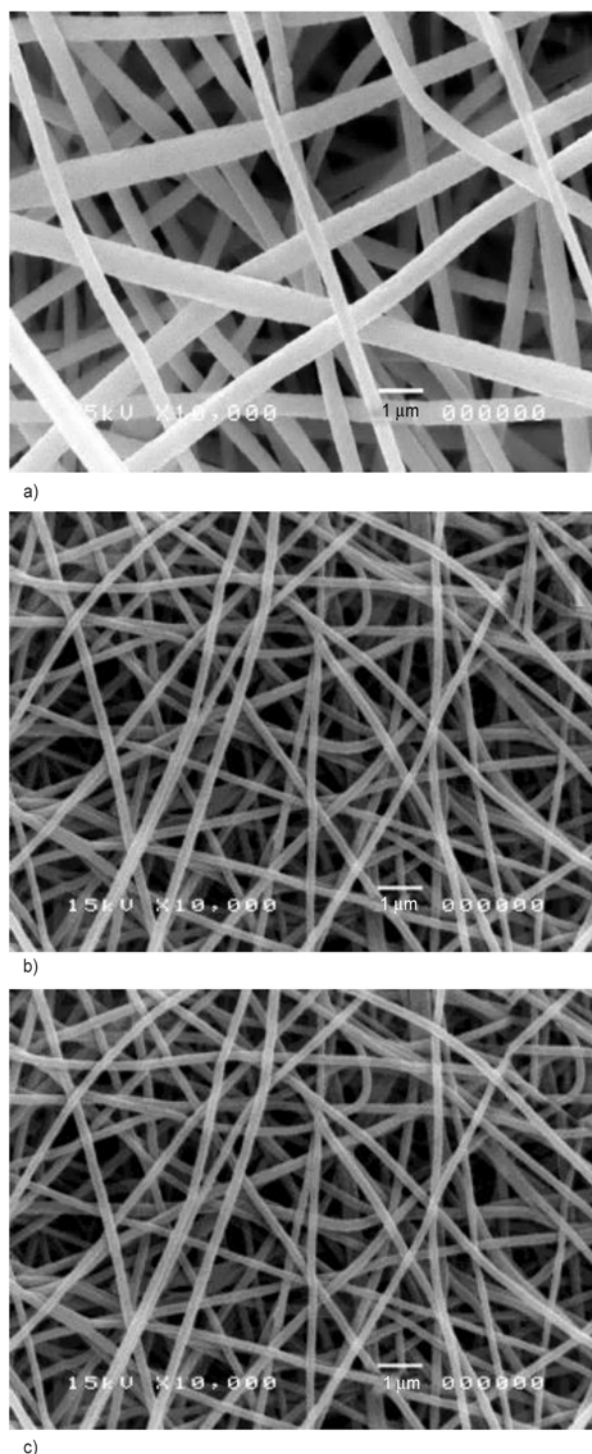


Figure 3. SEM images: (a) es-PAN, (b) es-PAN-DNPH nanofiber mats, and (c) es-PAN-DNPH fibers after adsorption of the metal solution

repulsive protonation. Beyond pH 5 the concentration of OH^- was high enough to interact with the free metal ions, thus the amount of adsorbed metal ions decreased.

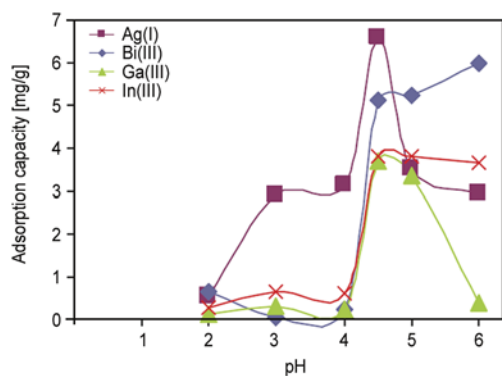


Figure 4. The effect of initial pH on the adsorption of Ag(I), Bi(III), Ga(III), and In(III) onto the es-PAN-DNPH chelating nanofiber mats

3.4. Recovery factors, adsorption kinetics and equilibrium isotherm of the metal ions onto PAN-DNPH chelating fiber

The adsorption capacities of Ag(I), Bi(III), Ga(III), and In(III) onto the es-PAN-DNPH nanofiber mats and c-PAN-DNPH fibers in a 200 ppm mixed standard stock solution as a function of time (to 24 hours) were depicted in mg/g (Figure 5). The equilibrium adsorption of Ag(I), Bi(III), Ga(III), and In(III) onto the es-PAN-DNPH were 0.045, 0.030, 0.042 and 0.023 mmole, respectively, where those onto the c-PAN-DNPH were 0.042, 0.022, 0.038 and 0.019 mmole, respectively (Table 1). The adsorption of Ag(I) and Bi(III) onto both the es-PAN-DNPH and the c-PAN-DNPH increased

Table 1. Maximum adsorption capacities of es-PAN-DNPH and c-PAN-DNPH to metal ions

Metal ions adsorbed	es-PAN-DNPH		c-PAN-DNPH	
	[mg/g]	[mmole/g]	[mg/g]	[mmole/g]
Ag(I)	4.865	0.045	4.481	0.042
Bi(III)	6.309	0.030	4.685	0.022
Ga(III)	2.960	0.042	2.666	0.038
In(III)	2.630	0.023	2.173	0.019

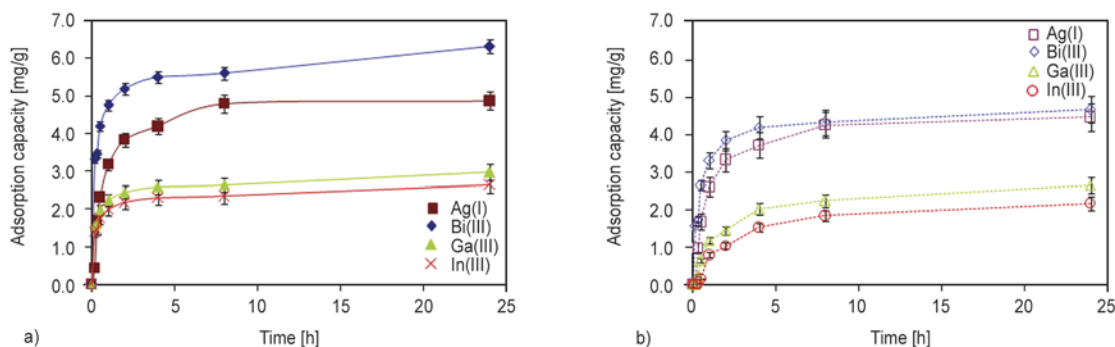


Figure 5. The adsorption of Ag(I), Bi(III), Ga(III), and In(III) onto (a) the es-PAN-DNPH nanofiber mats, and (b) c-PAN-DNPH fibers as a function of time (to 24 hours)

more sharply than Ga(III) and In(III) in the first 2 hours. After 8 hours, the adsorption capacity of the metal ions leveled off. The increases to 8 hours were attributed to the free binding sites on the surface of the adsorbents, after those binding sites were occupied, the adsorption capacities became saturated. The saturated adsorption capacities decreased in the following sequence: Bi(III) > Ag(I) > Ga(III) > In(III), which corresponded to the electronegativity value of each metal $2.02 > 1.93 > 1.81 > 1.78$, respectively. However, 0.045 mmole/g of Ag(I), which was the highest, adsorbed onto the es-PAN-DNPH and 0.042 mmole/g of Ag(I) adsorbed onto the c-PAN-DNPH. This might be due to the 1:1 complexation between metal ion group IB of the periodic table and es-PAN-DNPH. The amount of Ga(III) adsorbed onto the es-PAN-DNPH was nearly 2 times higher than the adsorbed In(III) [though both Ga(III) and In(III) are metal ions in the same group (IIIA) of the periodic table]. This might be due to the lighter molecular mass of Ga(III), which led to fast, easy adsorption. According to Liu *et al.* [11], the binding capacity of the chelating ion exchange media for each metal ion depends on the affinity of the functional groups towards the metal ion. The strength of the affinity can be expressed as the complex formation constant.

The adsorption kinetics of Ag(I), Bi(III), Ga(III), and In(III) onto the es-PAN-DNPH can be determined from the slope of the plot between $-\ln(1 - F)$ in relation to time (Figure 6). It was found that the adsorption rate of Ag(I) > Bi(III) ~ In(III) ~ Ga(III) (values were shown in Table 2). It is possibly because Ag(I) has the largest ionic radius of 115 pm [Bi(III) 103 pm, In(III) 80 pm, Ga(III) 62 pm]. The adsorption kinetics of Ag(I), Bi(III), Ga(III), and In(III) onto the c-PAN-DNPH are depicted in Figure 7. It was found that the adsorption rate of Ag(I) > Bi(III)

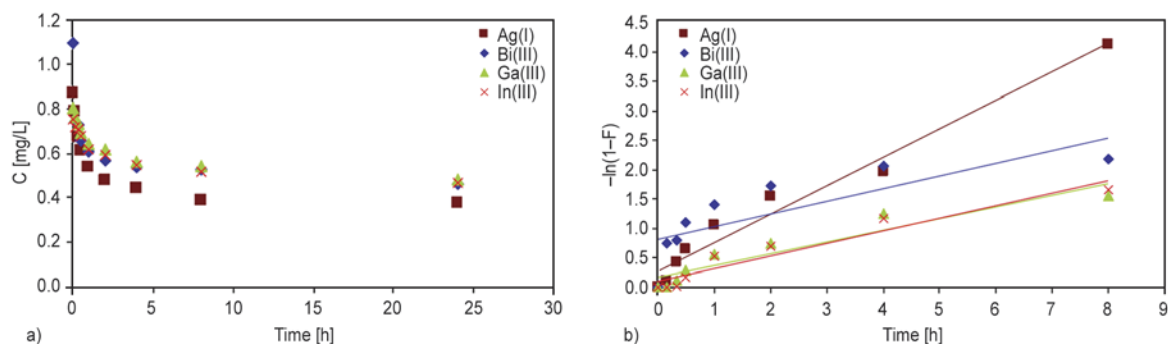


Figure 6. (a) metal ions solution concentration and (b) the adsorption kinetic of metal ions onto the es-PAN-DNPH nanofiber mats as a function of time (to 24 hrs)

Table 2. Rate constant of metal ion adsorption onto the es-PAN-DNPH and c-PAN-DNPH chelating fiber

Metal ion adsorbed	es-PAN-DNPH		c-PAN-DNPH	
	Rate constant [hr ⁻¹]	R ²	Rate constant [hr ⁻¹]	R ²
Ag(I)	0.484	0.9693	0.371	0.9468
Bi(III)	0.215	0.6446	0.291	0.7860
Ga(III)	0.199	0.8875	0.241	0.9164
In(III)	0.214	0.9283	0.252	0.9650

~In(III)~Ga(III) onto the c-PAN-DNPH was similar to the es-PAN-DNPH.

Figure 8 illustrates the equilibrium adsorption isotherm (24 hours of adsorption time) and Langmuir

plot of Ag(I), Bi(III), Ga(III), and In(III) ion onto the es-PAN-DNPH chelating nanofiber mats under various equilibrium concentrations (20–300 ppm). The formation of chelated structure between the metal ions and the es-PAN-DNPH (Figure 9) may be comparable with Ga(III) or In(III) – poly(acryl-phenylamidrazonophenylhydrazide) chelated complexes as reported by Chang *et al.* [16]. Because of the combination of nitrogen atoms in N–H and =N–H, and of oxygen atom in O=C–N with Ga(III) and In(III) to form cyclic compounds. The Langmuir constant q_m and K_L in Table 3 are calculated from the slope and intercept of the C_e/q_e versus C_e plot.

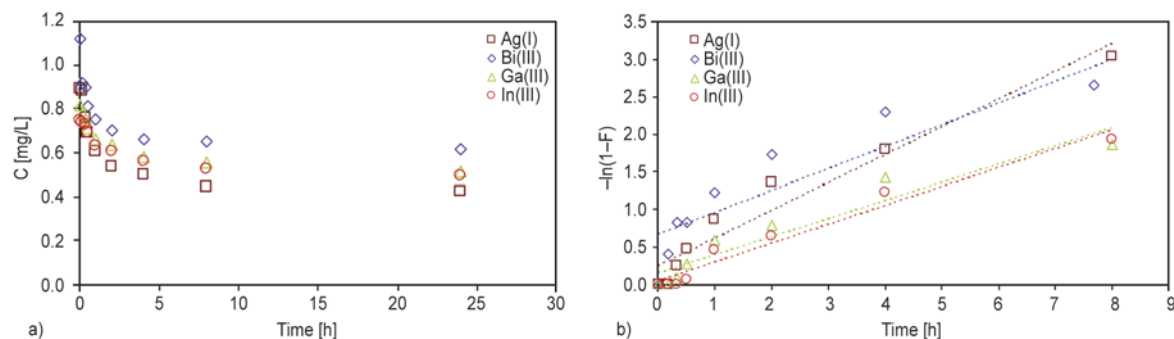


Figure 7. (a) metal ions solution concentration and (b) the adsorption kinetic of metal ions onto the c-PAN-DNPH fibers as a function of time (to 24 hrs)

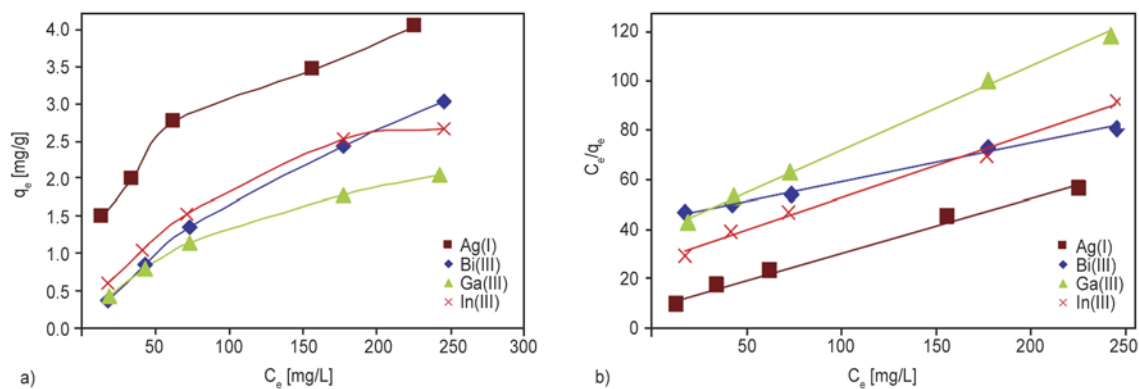


Figure 8. (a) Equilibrium adsorption isotherm of metal ions and (b) Langmuir plot of metal ions onto the es-PAN-DNPH nanofiber mats

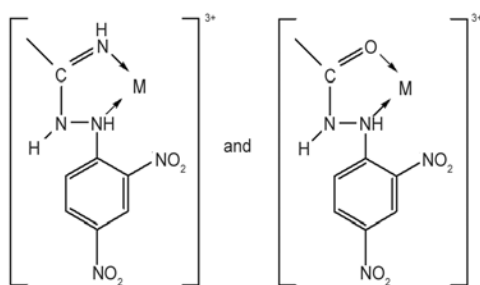


Figure 9. The formation of chelate structure between metal ions and the es-PAN-DNPH nanofiber mats

Table 3. Langmuir isotherm constants and correlation coefficients of metal ion adsorption onto the es-PAN-DNPH nanofiber mats

Metal ion adsorbed	Langmuir model		
	q_m [mg/g]	K_L [mL/mg]	R^2
Ag(I)	4.587	0.026	0.9887
Bi(III)	6.494	0.004	0.9951
Ga(III)	2.959	0.009	0.9977
In(III)	3.861	0.010	0.9929

The linear plot indicates that of all observed metal ions, adsorption followed the Langmuir isotherm. The basic assumption of the Langmuir theory is that adsorption takes place at specific homogeneous sites within the adsorbent [32]. The saturated adsorption constant, q_m of metal ions onto the es-PAN-DNPH were $\text{Bi(III)} > \text{Ag(I)} > \text{In(III)} > \text{Ga(III)}$. The saturated adsorption capacities of Bi(III) onto the es-PAN-DNPH were the highest. However, K_L of Ag(I) onto the es-PAN-DNPH were the highest, which revealed binding energy of Ag(I) to this specifically modified fiber. It is assumed that once a metal ion occupied a reaction site, no further adsorption can occur at that location.

The recovery factor of Bi(III), Ag(I), Ga(III), and In(III) onto the es-PAN-DNPH were 58.01, 56.57, 39.85, and 38.12%, respectively, which were about half less than those reported by continuous flow process. The recovery factor of Bi(III), Ag(I), Ga(III), and In(III) onto the c-PAN-DNPH were 45.15, 52.50, 36.85, and 33.70%, respectively. It was found that a high surface to volume ratio of the es-PAN-DNPH directly resulted in a higher recovery factor. Though there were large area of contact between the metal ions and the modified electrospun fiber mat, but the es-PAN-DNPH shrank when immersed in the solution. The saturated adsorption capacities of Ag(I) and Bi(III) onto the c-PAN-DNPH were lower than the es-PAN-DNPH results.

4. Conclusions

The es-PAN-DNPH nanofiber mats were successfully prepared by electrospinning a solution of conventional PAN fibers and converting the nitrile groups present in the fiber into metal ion affinity functional groups by chemical modification with 2,4-DNPH. The FT-IR spectra revealed the existence of $\text{NN}=\text{C}-\text{NHNH}-$, $\text{O}=\text{C}-\text{NHNH}-$, and $-\text{NO}_2$ functional groups for metal complexes. Certain metal ions – Ag(I), Bi(III), Ga(III), and In(III) – were adsorbed, with the initial pH of 4.5 being the optimal value where the es-PAN-DNPH nanofiber mats showed high adsorption toward all four types of the metal ions. The saturated adsorption capacities decreased as $\text{Bi(III)} > \text{Ag(I)} > \text{Ga(III)} > \text{In(III)}$, which corresponded to the electronegativity value of each metal. The adsorption of these metal ions was fitted well with the Langmuir equation, with the maximal adsorption capacities being 6.50, 4.59, 2.96 and 3.87 $\text{mg}\cdot\text{g}^{-1}$ for Bi(III), Ag(I), Ga(III) and In(III) ions, respectively, indicating monolayer adsorption manner. The obtained results suggested that the es-PAN-DNPH nanofiber mats possess a tremendous potential for use as an adsorbent for metal ions in wastewater effluents.

Acknowledgements

The authors acknowledge support from the Petroleum and Petrochemical College, and the Scientific and Technological Research Equipment Center, Chulalongkorn University.

References

- [1] Ministry of Science, Technology and Environment: Notification the Ministry of Science, Technology and Environment, No.3, B.E.2539 (1996) issued under the Enhancement and Conservation of the National Environmental Quality Act B.E.2535 (1992). The Royal Government Gazette, 113 Part13D, B.E.2539 (1996).
- [2] Pesavento M., Biesuz R., Gallorini M., Profumo A.: Sorption mechanism of trace amounts of divalent metal ions on a chelating resin containing iminodiacetate groups. *Analytical Chemistry*, **65**, 2522–2527 (1993). DOI: [10.1021/ac00066a021](https://doi.org/10.1021/ac00066a021)
- [3] Agrawal A., Sahu K. K.: Separation and recovery of lead from a mixture of some heavy metals using Amberlite IRC 718 chelating resin. *Journal of Hazardous Materials*, **133**, 299–303 (2006). DOI: [10.1016/j.jhazmat.2005.08.029](https://doi.org/10.1016/j.jhazmat.2005.08.029)

- [4] Lin L.-C., Li J.-K., Juang R.-S.: Removal of Cu(II) and Ni(II) from aqueous solutions using batch and fixed-bed ion exchange processes. *Desalination*, **225**, 249–259 (2008).
DOI: [10.1016/j.desal.2007.03.017](https://doi.org/10.1016/j.desal.2007.03.017)
- [5] Liu R., Tang H., Zhang B.: Removal of Cu(II), Zn(II), Cd(III) and Hg(II) from waste water by poly(acrylamino-phosphonic)-type chelating fiber. *Chemosphere*, **38**, 3169–3179 (1999).
DOI: [10.1016/S0045-6535\(98\)00506-2](https://doi.org/10.1016/S0045-6535(98)00506-2)
- [6] Hubicki Z., Leszczyńska M., Łodyga B., Łodyga A.: Palladium(II) removal from chloride and chloride–nitrate solutions by chelating ion-exchangers containing N-donor atoms. *Minerals Engineering*, **19**, 1341–1347 (2006).
DOI: [10.1016/j.mineng.2006.01.004](https://doi.org/10.1016/j.mineng.2006.01.004)
- [7] Egawa H., Nakayama M., Nonaka T., Sugihara E.: Recovery of uranium from sea water. IV. Influence of crosslinking reagent of the uranium adsorption of macroreticular chelating resin containing amidoxime groups. *Journal of Applied Polymer Science*, **33**, 1993–2005 (1987).
DOI: [10.1002/app.1987.070330613](https://doi.org/10.1002/app.1987.070330613)
- [8] Egawa H., Kabay N., Shuto T., Jyo A.: Recovery of uranium from seawater. XII. Preparation and characterization of lightly crosslinked highly porous chelating resins containing amidoxime groups. *Journal of Applied Polymer Science*, **46**, 129–142 (1992).
DOI: [10.1002/app.1992.070460113](https://doi.org/10.1002/app.1992.070460113)
- [9] Liu X., Chen H., Wang C., Qu R., Ji C., Sun C., Zhang Y.: Synthesis of porous acrylonitrile/methyl acrylate copolymer beads by suspended emulsion polymerization and their adsorption properties after amidoximation. *Journal of Hazardous Materials*, **175**, 1014–1021 (2010).
DOI: [10.1016/j.jhazmat.2009.10.111](https://doi.org/10.1016/j.jhazmat.2009.10.111)
- [10] Dominguez L., Yue Z., Economy J., Mangun C. L.: Design of polyvinyl alcohol mercaptal fibers for arsenite chelation. *Reactive and Functional Polymers*, **53**, 205–215 (2002).
DOI: [10.1016/S1381-5148\(02\)00174-8](https://doi.org/10.1016/S1381-5148(02)00174-8)
- [11] Liu R. X., Zhang B. W., Tang H. X.: Synthesis and characterization of poly(acrylamino-phosphonic-carboxyl-hydrazide) chelating fibre. *Reactive and Functional Polymers*, **39**, 71–81 (1999).
DOI: [10.1016/S1381-5148\(97\)00174-0](https://doi.org/10.1016/S1381-5148(97)00174-0)
- [12] Gong B.: Synthesis of polyacrylaminoimidazole chelating fiber and properties of concentration and separation of trace Au, Hg and Pd from samples. *Talanta*, **57**, 89–95 (2002).
DOI: [10.1016/S0039-9140\(02\)00005-X](https://doi.org/10.1016/S0039-9140(02)00005-X)
- [13] Gong B., Li X., Wang F., Xu H., Chang X.: Synthesis of polyacrylamino-urea chelating fiber and properties of concentration and separation of trace metal ions from samples. *Analytica Chimica Acta*, **427**, 287–291 (2001).
DOI: [10.1016/S0003-2670\(00\)01198-3](https://doi.org/10.1016/S0003-2670(00)01198-3)
- [14] Chang X., Su Q., Liang D., Wei X., Wang B.: Efficiency and application of poly(acryldinitrophenylamidrazone-dinitroacrylphenylhydrazine) chelating fiber for pre-concentrating and separating trace Au(III), Ru(III), In(III), Bi(III), Zr(IV), V(V), Ga(III) and Ti(IV) from solution samples. *Talanta*, **57**, 253–261 (2002).
DOI: [10.1016/S0039-9140\(02\)00032-2](https://doi.org/10.1016/S0039-9140(02)00032-2)
- [15] Chang X., Yang X., Wei X., Wu K.: Efficiency and mechanism of new poly(acryl-phenylamidrazone phenylhydrazide) chelating fiber for adsorbing trace Ga, In, Bi, V and Ti from solution. *Analytica Chimica Acta*, **450**, 231–238 (2001).
DOI: [10.1016/S0003-2670\(01\)01387-3](https://doi.org/10.1016/S0003-2670(01)01387-3)
- [16] Chang X., Li Y., Zhan G., Luo X., Gao W.: Synthesis of poly(N-aminoethyl)acrylamide chelating fiber and properties of concentration and separation of noble metal ions from samples. *Talanta*, **43**, 407–413 (1996).
DOI: [10.1016/0039-9140\(95\)01732-1](https://doi.org/10.1016/0039-9140(95)01732-1)
- [17] Soldatov V. S., Shunkevich A. A., Elinson I. S., Johann J., Iraushek H.: Chemically active textile materials as efficient means for water purification. *Desalination*, **124**, 181–192 (1999).
DOI: [10.1016/S0011-9164\(99\)00103-4](https://doi.org/10.1016/S0011-9164(99)00103-4)
- [18] Liao X., Ma H., Wang R., Shi B.: Adsorption of UO₂²⁺ on tannins immobilized collagen fiber membrane. *Journal of Membrane Science*, **243**, 235–241 (2004).
DOI: [10.1016/j.memsci.2004.06.025](https://doi.org/10.1016/j.memsci.2004.06.025)
- [19] Nishiyama S.-Y., Saito K., Saito K., Sugita K., Sato K., Akiba M., Saito T., Tsuneda S., Hirata A., Tamada M., Sugo T.: High-speed recovery of antimony using chelating porous hollow-fiber membrane. *Journal of Membrane Science*, **214**, 275–281 (2003).
DOI: [10.1016/S0376-7388\(02\)00558-6](https://doi.org/10.1016/S0376-7388(02)00558-6)
- [20] Yuan Y., Zhao Y., Li H., Li Y., Gao X., Zheng C., Zhang J.: Electrospun metal oxide–TiO₂ nanofibers for elemental mercury removal from flue gas. *Journal of Hazardous Materials*, **227–228**, 427–435 (2012).
DOI: [10.1016/j.jhazmat.2012.05.003](https://doi.org/10.1016/j.jhazmat.2012.05.003)
- [21] Irani M., Keshtkar A. R., Moosavian M. A.: Removal of cadmium from aqueous solution using mesoporous PVA/TEOS/APTES composite nanofiber prepared by sol–gel/electrospinning. *Chemical Engineering Journal*, **200–202**, 192–201 (2012).
DOI: [10.1016/j.cej.2012.06.054](https://doi.org/10.1016/j.cej.2012.06.054)
- [22] Zhang C., Li X., Bian X., Zheng T., Wang C.: Polyacrylonitrile/manganese acetate composite nanofibers and their catalysis performance on chromium (VI) reduction by oxalic acid. *Journal of Hazardous Materials*, **229–230**, 439–445 (2012).
DOI: [10.1016/j.jhazmat.2012.05.085](https://doi.org/10.1016/j.jhazmat.2012.05.085)
- [23] Taha A. A., Wu Y.-N., Wang H., Li F.: Preparation and application of functionalized cellulose acetate/silica composite nanofibrous membrane via electrospinning for Cr(VI) ion removal from aqueous solution. *Journal of Environment Management*, **112**, 10–16 (2012).
DOI: [10.1016/j.jenvman.2012.05.031](https://doi.org/10.1016/j.jenvman.2012.05.031)

- [24] Ramakrishna S., Fujihara K., Teo W-E., Yong T., Ma Z., Ramaseshan R.: Electrospun nanofibers: Solving global issues. *Materials Today*, **9**, 40–50 (2006). DOI: [10.1016/S1369-7021\(06\)71389-X](https://doi.org/10.1016/S1369-7021(06)71389-X)
- [25] Kampalananwat P., Supaphol P.: Preparation and adsorption behavior of aminated electrospun polyacrylonitrile nanofiber mats for heavy metal ion removal. *ACS Applied Materials and Interface*, **2**, 3619–3627 (2010). DOI: [10.1021/am1008024](https://doi.org/10.1021/am1008024)
- [26] Kampalananwat P., Supaphol P.: Preparation of hydrolyzed electrospun polyacrylonitrile fiber mats as chelating substrates: A case study on copper(II) ions. *Industrial and Engineering Chemistry Research*, **50**, 11912–11921 (2011). DOI: [10.1021/ie200504c](https://doi.org/10.1021/ie200504c)
- [27] Reneker D. H., Yarin A. L.: Electrospinning jets and polymer nanofibers. *Polymer*, **49**, 2387–2425 (2008). DOI: [10.1016/j.polymer.2008.02.002](https://doi.org/10.1016/j.polymer.2008.02.002)
- [28] Sill T. J., von Recum H. A.: Electrospinning: Applications in drug delivery and tissue engineering. *Biomaterials*, **29**, 1989–2006 (2008). DOI: [10.1016/j.biomaterials.2008.01.011](https://doi.org/10.1016/j.biomaterials.2008.01.011)
- [29] Shin Y. M., Hohman M. M., Brenner M. P., Rutledge G. C.: Experimental characterization of electrospinning: The electrically forced jet and instabilities. *Polymer*, **42**, 9955–9967 (2001). DOI: [10.1016/s0032-3861\(01\)00540-7](https://doi.org/10.1016/s0032-3861(01)00540-7)
- [30] Saeed K., Haider S., Oh T-J., Park S-Y.: Preparation of amidoxime-modified polyacrylonitrile (PAN-oxime) nanofibers and their applications to metal ions adsorption. *Journal of Membrane Science*, **322**, 400–405 (2008). DOI: [10.1016/j.memsci.2008.05.062](https://doi.org/10.1016/j.memsci.2008.05.062)
- [31] Sang Y., Li F., Gu Q., Liang C., Chen J.: Heavy metal-contaminated groundwater treatment by a novel nanofiber membrane. *Desalination*, **223**, 349–360 (2008). DOI: [10.1016/j.desal.2007.01.208](https://doi.org/10.1016/j.desal.2007.01.208)
- [32] Ma Z., Masaya K., Ramakrishna S.: Immobilization of cibacron blue F3GA on electrospun polysulphone ultra-fine fiber surfaces towards developing an affinity membrane for albumin adsorption. *Journal of Membrane Science*, **282**, 237–244 (2006). DOI: [10.1016/j.memsci.2006.05.027](https://doi.org/10.1016/j.memsci.2006.05.027)
- [33] Yarin A. L., Koombhongse S., Reneker D. H.: Taylor cone and jetting from liquid droplets in electrospinning of nanofibers. *Journal of Applied Physics*, **90**, 4836–4846 (2001). DOI: [10.1063/1.1408260](https://doi.org/10.1063/1.1408260)
- [34] Doshi J., Reneker D. H.: Electrospinning process and applications of electrospun fibers. *Journal of Electrostatics*, **35**, 151–160 (1995). DOI: [10.1016/0304-3886\(95\)00041-8](https://doi.org/10.1016/0304-3886(95)00041-8)
- [35] Wannatong L., Sirivat A., Supaphol P.: Effects of solvents on electrospun polymeric fibers: Preliminary study on polystyrene. *Polymer International*, **53**, 1851–1859 (2004). DOI: [10.1002/pi.1599](https://doi.org/10.1002/pi.1599)
- [36] Reneker D. H., Yarin A. L., Fong H., Koombhongse S.: Bending instability of electrically charged liquid jets of polymer solutions in electrospinning. *Journal of Applied Physics*, **87**, 4531–4547 (2000). DOI: [10.1063/1.373532](https://doi.org/10.1063/1.373532)
- [37] Jarusuwannapoom T., Hongrojjanawiwat W., Jitjaicham S., Wannathong L., Nithitanakul M., Pattamaprom C., Koombhongse P., Rangkupan R., Supaphol P.: Effect of solvents on electro-spinnability of polystyrene solutions and morphological appearance of resulting electrospun polystyrene fibers. *European Polymer Journal*, **41**, 409–421 (2005). DOI: [10.1016/j.eurpolymj.2004.10.010](https://doi.org/10.1016/j.eurpolymj.2004.10.010)
- [38] Pattamaprom C., Hongrojjanawiwat W., Koombhongse P., Supaphol P., Jarusuwannapoom T., Rangkupan R.: The influence of solvent properties and functionality on the electrospinnability of polystyrene nanofibers. *Macromolecular Materials and Engineering*, **291**, 840–847 (2006). DOI: [10.1002/mame.200600135](https://doi.org/10.1002/mame.200600135)
- [39] Park S-J., Im S-H.: Electrochemical behaviors of PAN/Ag-based carbon nanofibers by electrospinning. *Bulletin of the Korean Chemical Society*, **29**, 777–781 (2008). DOI: [10.5012/bkcs.2008.29.4.777](https://doi.org/10.5012/bkcs.2008.29.4.777)

Synthesis and characterization of naphthalene diimide polymers based on donor-acceptor system for polymer solar cells

Q. Xu¹, J. Wang², S. Chen^{1*}, W. Li², H. Wang¹

¹State Key Laboratory for Modification of Chemical Fibers and Polymer Materials, The Key Laboratory of High-Performance Fiber and Product, Ministry of Education, College of Materials Science and Engineering, Donghua University, 201620 Shanghai, P R China

²Laboratory of Materials Science, Shanghai Institute of Organic Chemistry, Chinese Academy of Sciences (CAS), 345 Lingling Road, 200032 Shanghai, China

Received 1 April 2013; accepted in revised form 22 June 2013

Abstract. Three donor-acceptor (D–A) naphthalene diimide copolymers, poly {thieno[3,2-b]thiophene-diyl-alt-N,N'-bis(2-octyldodecyl)-naphthalene-1,4,5,8-bis(dicarboximide)} (**P1**), poly {4,8-dioctyloxybenzo[1,2-b;3,4-b']dithiophene-diyl-alt-N,N'-bis(2-octyldodecyl)-naphthalene-1,4,5,8-bis(dicarboximide)} (**P2**), and poly {4,8-bis(2-ethylhexyloxy)benzo[1,2-b;4,5-b']dithiophene-diyl-alt-N,N'-bis(2-octyldodecyl)-naphthalene-1,4,5,8-bis(dicarboximide)} (**P3**), were synthesized by Stille coupling reaction. All copolymers showed good solubility in common organic solvents with broad absorption region and narrow optical band gap. The electrochemical properties of the polymers can be adjusted by changing the donor segment. **P1** showed n-type characteristic while **P2** and **P3** showed p-type characteristic. All-polymer solar cells using P3HT as the donor and **P1** as the acceptor were fabricated and the highest power conversion efficiencies (PCEs) of 0.068% were obtained under the preliminary condition. Moreover, p-type naphthalene diimide copolymers (**P2** and **P3**) based on D–A system were used as donors to fabricate bulk heterojunction polymer solar cells (BHJ, PSCs) for the first time, and the maximum power conversion efficiencies PCEs were about 0.021 and 0.017%, respectively.

Keywords: Tailor-made polymers, polymer solar cells (PSCs), naphthalene diimide, donor-acceptor

1. Introduction

The continually growing demand for energy throughout the world has attracted great attention on the exploration of new energy types. The utilization of the photovoltaic effect to generate electricity from solar energy, which is known as a clean and renewable energy source, represents an effective way to solve the energy shortage [1]. Polymer solar cells have drawn considerable attention because of their low-cost, light weight, flexibility, inkjet printing process and large-area fabrication [2–4]. Over the last decade, the performance of polymer solar cells

(PSCs) has been significantly improved owing to the synthesis of novel photovoltaic materials, as well as device optimization. Nevertheless, there are still several issues regarding to PSCs such as solution processing, low power conversion efficiencies and stability compared with silicon solar cells [5]. So far, bulk heterojunction solar cells, which are composed of an interpenetrating network of donors and acceptors, have played a leading role in fabricating PSCs due to better performance at carrier transmission [6]. The most typical bulk heterojunction (BHJ) solar cells are using poly(3-hexylthio-

*Corresponding author, e-mail: chensy@dhu.edu.cn
© BME-PT

phene) (P3HT) as donor and [6,6]-phenyl-C61-butyric acid methyl ester (PC₆₁BM) as acceptor, however, it's challenging to improve the power conversion efficiencies (PCEs) over 5% due to the intrinsic absorption limit of P3HT and the weak absorption in the visible region of PC₆₁BM [7].

Therefore, it is necessary to design and synthesize conjugated polymers with expected properties, such as low band gap, broad absorption range, high mobility, appropriate molecular energy levels and easy processing. Recently, some excellent works with the PCEs over 7% have been extensively reported, such as Yu *et al.* reported a PCE of 7.4% [8]. In order to improve the absorption property, introducing the D–A system to the polymers has been proved to be an efficient approach, in which conjugated electron-rich (donor) and electron-deficient (acceptor) units are alternatively copolymerized to manipulate optical band gap and optimize the HOMO and LUMO energy levels via intramolecular charge transfer (ICT) [9]. Semiconducting materials with strong electron-withdrawing groups comprising the structure of naphthalene diimide (NDI) and perylene diimide (PDI) have been used as acceptor units in the conjugated polymers [10]. In particular, NDI based polymers attract a great deal of attention recently due to the reports on the merit of their facile soluble processing for organic field effect transistors (OFETs) and PSCs device [11, 12]. As an acceptor unit, NDI can be copolymerized easily with a wide variety of donor units to adjust the optoelectronic properties of the resulting polymers [13, 14]. This NDI unit has a large planar structure which is favorable for the electron delocalization along the polymeric backbone [15].

In this study, we synthesized three NDI-based polymers by combination of NDIs with different donor segments, including thienothiophene and dibenzothiophene derivatives. We obtained **P1** as n-type polymer, **P2** and **P3** as p-type polymers. **P1** with a rigid structure has a better absorption in the visible region than PC₆₁BM. In addition, it shows good solubility in common organic solvents comparing with PC₆₁BM, so it was used as acceptor unit and P3HT as donor unit to fabricate all-polymer blends PSCs. For different alkoxy side chain, **P2** and **P3** show excellent solubility and they have closed energy level with a lower band gap than P3HT, so they were used as donor unit and PC₆₁BM as acceptor unit to fabricate PSCs. The PCEs of the PSCs based on **P1**,

P2 and **P3**, under standard global AM 1.5 solar conditions, were 0.068, 0.021 and 0.017%, respectively. As all of the devices have very low short-circuit density, and the performance of the devices has big improvement possibility. We consider that the reason could be the difficulty in forming the interpenetrating networks which are necessary for efficient transport of both electrons and holes to the electrodes.

2. Experimental

2.1. Measurements and characterization

¹H NMR (300 or 400 MHz) spectra were measured in CDCl₃ on Varian Mercury (300 or 400 MHz) instruments, using tetramethylsilane as an internal standard. Elemental analyses were performed on an Elementar Vario EL III elemental analyzer. Electronic absorption spectra were measured on a U-3900 UV-vis spectrophotometer. TGA measurements were carried out on a TA Q500 instruments under a dry nitrogen flow at a heating rate of 10°C/min, from room temperature to 500°C. DSC analyses were performed on a TA Q20 instrument under nitrogen atmosphere at a heating (cooling) scan rate of 10°C/min (0–280°C). Cyclic voltammetric measurements were carried out in a conventional three-electrode cell using a platinum button working electrode of 2 mm diameter, a platinum wire counter electrode, and a silver-silver chloride reference electrode on a computer-controlled CHI610D instruments. AFM was recorded on a Nanoscope IIIa atomic force microscopy (AFM) in tapping mode.

2.2. Materials

1,4,5,8-Naphthalenetetracarboxylic dianhydride (NTCDA, 95%) was purchased from Aladdin (China). 3-Bromothiophene (97%) was purchased from Alfa Aesar. Benzo[1,2-b:4,5-b']dithiophene-4,8-dione (97%) and trimethyltin chloride (1.0 M in hexanes) were purchased from Aldrich. All the chemicals not mentioned before were purchased from Sinopharm Chemical Reagent Co. (China) and used as received. Tetrahydrofuran (THF), diethyl ether and toluene were dried by distillation from sodium/benzophenone under nitrogen. Similarly, N, N-dimethyl formamide (DMF) was distilled from CaH₂ under nitrogen. The following compounds were synthesized according to the procedures in the literatures: 2,6-dibromonaphthalene-1,4,5,8-tetracarboxydianhydride, 2-octyldodecylamine, 2,5-dibromothieno

[3,2-*b*]thiophene, 4,8-dioctyloxybenzo[1,2-*b*;3,4-*b'*]dithiophene [16–21].

2.3. Photovoltaic devices fabrication and characterization

The solar cells were fabricated with a device structure ITO/poly(3,4-ethylenedioxythiophene):poly(styrenesulfonate)(PEDOT:PSS)/Polymer:PC₆₁BM Blend/Ca/Al. The ITO glass substrates were pre-cleaned by detergent, acetone and boiling in H₂O₂. PEDOT:PSS as a hole-conducting layer was spin-casted (4000 rpm) at a thickness of about 30 nm from aqueous solution. The substrate was annealed at 150°C for 20 min on a hot plate. The active layer contained a blend of copolymers as electron donor or electron acceptor, which was prepared with different weight ratios of the copolymers (1:1, 1:2, 1:3, w/w) in chlorobenzene (8 mg/mL). The active layers were obtained by spin coating of the blend solutions at 4000 rpm for 30 s and the thickness of films were 80 nm, as measured with the Veeco DecTak 150 profilometer IV. Subsequently, Ca (10 nm) and Al (100 nm) electrodes were deposited via thermal evaporation in vacuum (5·10⁻⁴ Pa). The active area was about 7 mm². Current-voltage (*J-V*) characteristics were recorded using Oriol So13A solar simulator in dark and under 100 Mw/cm² simulated AM 1.5G irradiation. All the measurements were performed under nitrogen atmosphere at room temperature.

2.4. Synthesis

N,N'-bis(2-octyldodecyl)-2,6-dibromonaphthalene-1,4,5,8-bis(dicarboximide) (**1**)

A mixture of 2,6-dibromonaphthalene-1,4,5,8-tetracarboxydianhydride (1.28 g, 3 mmol), 2-octyldodecylamine (2.68 g, 9 mmol), *o*-xylene (30 mL), and propionic acid (10 mL) was stirred at 140°C for 2 h. Upon cooling to ambient temperature, most of solvents were removed in vacuum, and the residue was purified by column chromatography on silica gel using a mixture of dichloromethane: hexane (1:3, v/v) as eluent. Compound **1** was obtained as a slightly yellow solid (544.4 mg, 18.3%). ¹H NMR (300 MHz, CDCl₃) δ 0.86–0.87 (m, 6H), 1.23–1.29 (br, 32H), 1.98 (m, 1H), 4.13–4.16 (d, 2H), 9.00 (s, 2H).

2,5-Bis(trimethylstannyl)thieno[3,2-*b*]thiophene(2) n-Butyllithium (1.6 mL, 2.5 mol/L, 4 mmol) was added dropwise to a mixture of 2,5-dibromothieno[3,2-*b*]thiophene (596 mg, 2 mmol) and THF (20 mL) at –78°C and the resulting mixture was stirred for a further 1.5 h at this temperature. Then trimethyltinchloride (4 ml, 1 mol/L, 4 mmol) was added and stirred for about 6 h at ambient temperature. Then H₂O (20 mL) was added to the mixture, extracted with diethyl ether, dried (MgSO₄), filtered and concentrated in vacuum. The residue was purified by column chromatography on neutral aluminium oxide using a mixture of triethylamine: hexane (1:20, v/v) as eluent, then the obtained product **2** was recrystallized in ethanol to from a white crystal (0.31 g, 33.3%). ¹H NMR (300 MHz, CD₃COCD₃) δ 0.39 (s, 18H), 7.37 (s, 2H).

2,6-Bis(trimethyltin)-4,8-dioctyloxybenzo[1,2-*b*;3,4-*b'*]dithiophene(3a)

n-Butyllithium (4.4 mL, 2.4 mol/L, 10.5 mmol) was added dropwise to a stirred solution of 4,8-dioctyloxybenzo [1,2-*b*;3,4-*b'*] dithiophene (2.23 g, 5 mmol) in THF (50 mL) at –78°C and the resulting mixture was stirred for another hour at this temperature. Trimethyltinchloride (10.5 mL, 1 mol/L, 10.5 mmol) was added and stirred for about 12 h at ambient temperature. At last H₂O (30 mL) was added to the mixture, then extracted with CH₂Cl₂, dried (MgSO₄), filtered and concentrated in vacuum. The residue was purified by column chromatography on neutral aluminium oxide using a mixture of triethylamine : hexane (1:20, v/v) as eluent, then the obtained product **3a** was recrystallized in isopropyl alcohol to from a white crystal (3.2 g, 82.8%). ¹H NMR (300 MHz, CDCl₃): δ 0.44 (s, 18H), 0.86–0.92 (t, 6H), 1.31–1.42 (br, 20H), 1.57–1.60 (m, 4H), 4.27–4.30 (d, 4H), 7.51 (s, 2H).

2,6-Bis(trimethyltin)-4,8-bis(2-ethylhexyloxy)benzo [1,2-*b*:4,5-*b'*]dithiophene(3b)

Compound **3b** was synthesized according to the similar procedure as described for compound **3a** as a white crystal (1.67 g, 86%). ¹H NMR (300 MHz, CDCl₃): δ 0.44 (s, 18H), 0.85–1.07 (m, 12H), 1.28–1.49 (m, 16H), 1.74–1.88 (m, 2H), 4.17–4.22 (d, 4H), 7.52 (s, 2H).

*Poly{thieno[3,2-*b*]thiophene-diyl-alt-*N,N'*-bis(2-octyldodecyl)-naphthalene-1,4,5,8-bis(dicarboximide)}* (**P1**)

Monomer **2** (95 mg, 0.204 mmol), monomer **1** (200 mg, 0.203 mmol), Pd₂(dba)₃ (10 mg, 5%) and P(*o*-tol)₃ (10 mg, 15%) were added to a 50 mL flask. The reaction container was flushed with N₂ for 20 min to remove oxygen, then dry toluene (25 mL) was added and heated under reflux for 2 days. The reactant was cooled to ambient temperature and was added dropwise to methanol (200 mL). The precipitate was filtered and then dissolved in CHCl₃ and quickly passed through a silica column to remove the metal catalyst. Then, the obtained **P1** was subjected to Soxhlet extractions and refluxed with acetone, hexane, and CHCl₃ in succession to from a dark blue solid (191.4 mg, 96.4%). ¹H NMR (400 MHz, CDCl₃): δ 0.84–0.98 (m, 12H), 1.09–1.42 (br, 64H), 2.47 (m, 2H), 4.11 (d, 2H), 7.66 (s, 2H), 8.87 (s, 2H). Anal. Calcd. For C₆₀H₈₈N₂O₄S₂ (%): C, 74.64; H, 9.19; N, 2.90. Found (%): C, 74.63; H, 9.28; N, 2.49.

*Poly{4,8-dioctyloxybenzo[1,2-*b*;3,4-*b'*] dithiophene-diyl-alt-*N,N'*-bis(2-octyldodecyl)-naphthalene-1,4,5,8-bis(dicarboximide)}* (**P2**)

The synthetic procedure for **P2** was carried out according to the aforementioned synthesis of **P1**. **P2** was obtained as a dark green solid (120 mg, 51.2%). ¹H NMR (400 MHz, CDCl₃): δ 0.78–0.97 (br, 18H), 1.23–1.49 (br, 84H), 1.89–2.04 (br, 6H), 4.13–4.40(d, 8H), 7.69 (s, 2H), 8.96 (s, 2H). Anal. Calcd. For C₈₀H₁₂₂N₂O₆S₂ (%): C, 75.54; H, 9.67; N, 2.20. Found (%): C, 75.47; H, 9.66; N, 1.89.

*Poly{4,8-bis(2-ethylhexyloxy)benzo[1,2-*b*:4,5-*b'*] dithiophene-diyl-alt-*N,N'*-bis(2-octyldodecyl)-naphthalene-1,4,5,8-bis(dicarboximide)}* (**P3**)

The synthetic procedure for **P3** was carried out according to the aforementioned synthesis of **P1**. **P3** was obtained as a dark green solid (213 mg, 90.7%). ¹H NMR (400 MHz, CDCl₃): δ 0.74–0.95 (br, 24H), 1.11–1.44 (br, 78H), 1.68 (br, 2H), 1.86–2.04 (br, 4H), 4.11–4.31 (br, 8H), 7.67 (s, 2H), 8.96 (s, 2H). Anal. Calcd. For C₈₀H₁₂₂N₂O₆S₂ (%): C, 75.54; H, 9.67; N, 2.20. Found (%): C, 75.38; H, 9.42; N, 2.14.

3. Results and discussion

3.1. Synthesis and characterization

The synthetic routes for all the polymers are illustrated in Figure 1. Monomer **1** was synthesized in a mixed solvent according to previously published reports [16, 17]. Monomer **2** was synthesized in a multistep synthesis by the reported methods in five steps shown in supporting information [18, 19]. Monomer **3a** and **3b** were synthesized with good yields using the same method, starting from commercially available 8-dihydrobenzo[1,2-*b*:4,5-*b'*] dithiophene-4,8-dione [20, 21]. Copolymers of **P1**, **P2** and **P3** were synthesized through Stille coupling reaction of monomer **1** and **2**, monomer **1** and **3a**, monomer **1** and **3b**, respectively. All the polymers have good solubility in chloroform, chlorobenzene, and dichlorobenzene, and the good solubility endowing them with easy soluble processibility for the applications in organic photovoltaics (OPVs) and other optoelectronic devices. The number-average molecular weight (*M_n*) and weight-average molecular weights (*M_w*) of **P1**, **P2** and **P3** were determined by gel permeation chromatography (GPC) using polystyrene as standard in THF eluent, and the detailed GPC data are listed in Table 1. As shown in Table 1 *M_n* and *M_w* of **P1** are much bigger than those of **P2** and **P3**. It might be ascribed to less side chain of **P1**, which affected the arrangement of the polymer. Moreover, the steric hindrance of side chain could produce detrimental effects on polymerization [22]. Thermal stability of the copolymers was investigated with thermogravimetric analysis (TGA) and the data are listed in Table 1. The TGA analysis reveals that the onset points of the weight loss with 5% weight-loss temperature (*T_d*) for **P1**, **P2** and **P3** are 438, 325 and 322°C in the nitrogen, which indicated that all of them have good thermal stability [23]. From the DSC measurement, a glass transition temperature was not observed from the ambient temperature to 280°C for all of the polymers.

3.2. Optical properties

Figures 2 and 3 show the UV-vis absorption spectra of **P1**, **P2** and **P3**, which were measured in both dilute CHCl₃ and in the thin films, respectively. The optical properties of the main parameters are listed

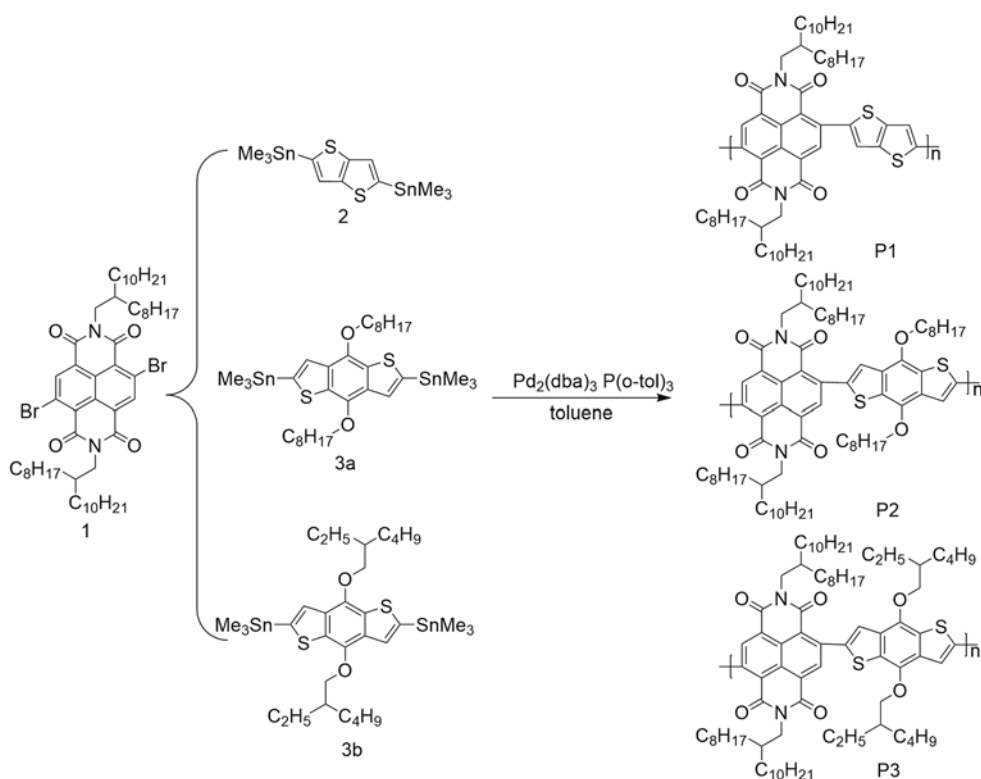


Figure 1. Synthesis routes for **P1**, **P2** and **P3**

in Table 2. It can be shown in Figure 2 that **P1** showed a maximum absorption around 654 nm in thin film, which undergoes a red-shift of 17 nm compared to that in CHCl₃ solution, indicating a somewhat greater degree of organization in the thin film

Table 1. Polymerization results and thermal properties of **P1**, **P2** and **P3**

Polymer	Mn [10 ³]	Mw [10 ³]	PDI	Td [°C]
P1	97.18	348.52	3.59	438
P2	32.42	123.38	3.81	325
P3	20.63	53.95	2.62	322

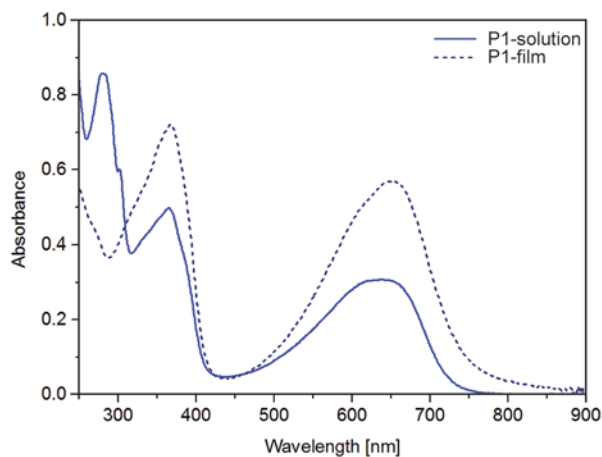


Figure 2. UV-vis absorption spectra of **P1** in the CHCl₃ solution and the thin film

[24]. The band gap of **P1** calculated from the onset of the absorption maxima is about 1.67 eV. From Figure 3, we can see that **P2** and **P3** have one band in the shorter wavelengths region (400–500 nm) with the absorption peaks around 479 and 472 nm, respectively. These peaks are attributed to localized π - π^* transitions (LT), and the peaks at longer wavelengths (500–700 nm) are due to intramolecular charge transfer (ICT) band between donors units and naphthalene diimide acceptors units. The maximum absorption peak of **P2** shifted toward longer wavelengths for about 11 nm from the solution state

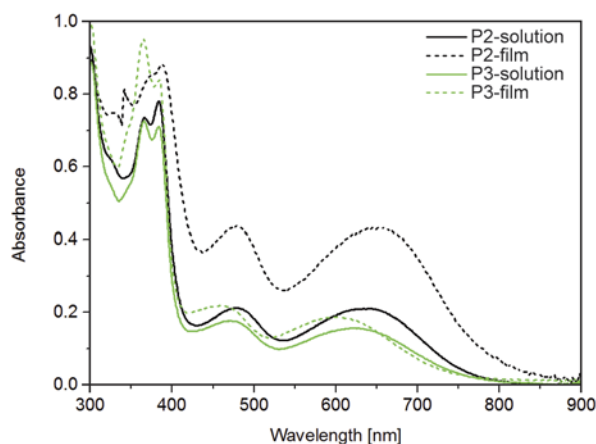


Figure 3. UV-vis absorption spectra of **P2** and **P3** in the CHCl₃ solution and the thin film

Table 2. Optical properties of **P1**, **P2** and **P3**

Polymer	Chloroform solution			Thin film		
	λ_{\max} [nm]	λ_{onset} [nm] ^a	E_g^{opt} [eV]	λ_{\max} [nm]	λ_{onset} [nm]	E_g^{opt} [eV] ^b
P1	637	726	1.71	654	744	1.67
P2	641	768	1.61	652	792	1.57
P3	621	759	1.63	600	733	1.69

^aCalculated from the onset of the absorption maxima in the CHCl₃ solution.

^bCalculated from the onset of the absorption maxima in the thin films prepared by spin-coating.

to the solid state, indicating the formation of inducing strong π - π^* stacked structure [25]. In contrast, the maximum absorption peak of **P3** shifted toward shorter wavelengths for about 21 nm from the solution state to the solid state. This phenomenon may be attributed to the irregular molecular arrangement of the more branched chains in **P3**, which leads to the decreased intramolecular charge transfer [26]. The band gap (E_g) of **P2** and **P3** calculated from the onset of the absorption maxima are according to the Equation (1).

The E_g of **P2** and **P3** were 1.57 and 1.69 eV, respectively:

$$E_g = \frac{1240}{\lambda_{\text{onset}}} \quad (1)$$

3.3. Electrochemical properties

Cyclic voltammetry (CV) was employed to examine the electrochemical properties and evaluate the HOMO and LUMO levels of the polymers. Figures 4 and 5 show the cyclic voltammograms of **P1**, **P2** and **P3** films on the platinum button working elec-

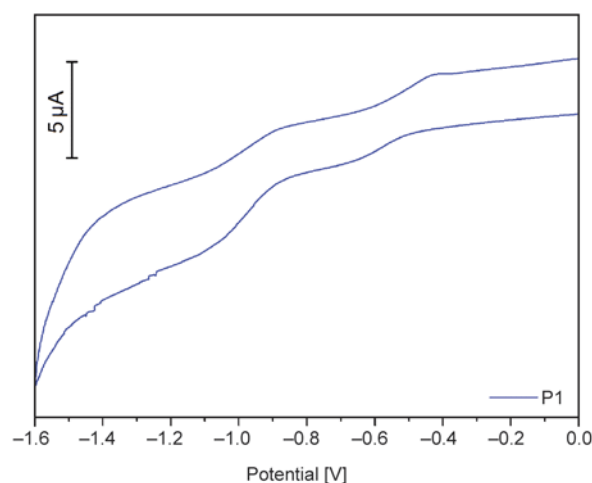


Figure 4. Cyclic voltammograms of **P1**, measured in 0.1 mol/L Bu₄NPF₆ acetonitrile solution, scan rate = 100 mV/s

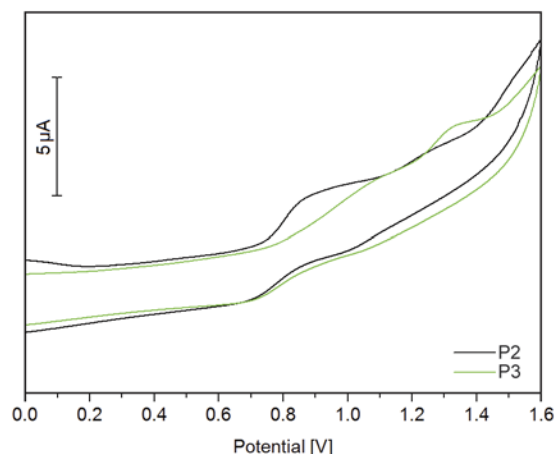


Figure 5. Cyclic voltammograms of **P2** and **P3**, measured in 0.1 mol/L Bu₄NPF₆ acetonitrile solution, scan rate = 100 mV/s

Table 3. Electrochemical properties of **P1**, **P2** and **P3**

Polymer	E_{ox} [eV]	E_{red} [eV]	HOMO [eV]	LUMO [eV]
P1	–	–0.52	–5.49	–3.82
P2	0.74	–	–5.08	–3.51
P3	0.77	–	–5.11	–3.42

trode of 2 mm diameter, using a platinum wire counter electrode, and an Ag/AgCl reference electrode in a 0.1 mol/L Bu₄NPF₆ acetonitrile solution. (Fc/Fc⁺) was used as the internal standard. The results of the electrochemical measurements are listed in Table 3. HOMO and LUMO energy levels as well as the band gap were calculated according to the Equation (2), (3) and (4) [27]:

$$\text{HOMO [eV]} = -e(E_{\text{ox}}^{\text{onset}} + 4.34) \text{ [eV]} \quad (2)$$

$$\text{LUMO [eV]} = -e(E_{\text{red}}^{\text{onset}} + 4.34) \text{ [eV]} \quad (3)$$

$$E_g \text{ [eV]} = -(\text{HOMO [eV]} - \text{LUMO [eV]}) \quad (4)$$

On the cathodic sweep, **P1** showed an onset reduction potential of –0.52 V. According to the equations, the LUMO energy level of **P1** is –3.82 eV, and the HOMO energy level of **P1** is –5.49 eV. The deep HOMO levels of **P1** should be beneficial to its chemical stability in ambient conditions. Zhou *et al.* [28], reported that LUMO energy levels of perylene diimide based polymers are lower than 3.6 eV as acceptors for application in PSCs, so we used **P1** as an acceptor in the active layer blend. In contrast, the anodic sweep showed onset oxidation potentials of 0.74 V for **P2** and 0.77 V for **P3**. The HOMO energy

levels of **P2** and **P3** are at -5.08 and -5.11 eV, respectively. The LUMO levels of **P2** and **P3** are at -3.51 and -3.42 eV, respectively, which implies that they could have more effective charge transfer to PC₆₁BM than P3HT's charge transfer to PC₆₁BM [29].

3.4. Photovoltaic properties

To investigate the photovoltaic properties of the polymers, we fabricated OPV devices, and the structures of the devices were ITO/PEDOT:PSS/P3HT:**P1**/Ca/Al and ITO/PEDOT:PSS/**P2**(**P3**):PC₆₁BM/Ca/Al. Figures 6 and 7 show the current-voltage (J - V) curves of PSCs based on **P1**, **P2** and **P3**. The photovoltaic parameters of the PSCs are summarized in Table 4. The active layer blends for all polymers were spin coated from chlorobenzene solution. We optimized the ratio of P3HT to **P1** (1:1 to 4:1) in the active layer and the ratio of **P2** and **P3** to PC₆₁BM

Table 4. Photovoltaic properties of the photovoltaic cells

Polymer	D:A ratio	V _{oc} [V]	J _{sc} [mA/cm ²]	FF [%]	PCE [%]
P1 ^a	3:1	0.47	0.29	49.5	0.068
P2 ^b	1:3	0.56	0.14	27.1	0.021
P3 ^b	1:3	0.49	0.12	27.2	0.017

^a**P1** as acceptor and P3HT as donor.

^b**P2** and **P3** as donor and PC₆₁BM as acceptor.

(1:1 to 1:3). And all the devices were annealed at 120°C for 10 min.

From the cyclic voltammetry test, we can see that **P1** showed n-type semiconductor properties. So **P1** can be used as the acceptor in the active layer to fabricate the devices. Under standard global AM 1.5 solar conditions, the photovoltaic cells based on P3HT:**P1** with a ratio of 3:1 showed the highest PCE of 0.068%. Compared with these reported polymers, **P1** had longer alkyl chains which can lead to good solubility [28, 30, 31]. However, larger alkyl chains may affect the aggregation of the molecules, thus the surface morphology of the spin coated films. It may be the main reason of the lower efficiency of the solar cells than the reported polymers. Photovoltaic cells based on **P1** have a relatively high fill factor (FF) with the maximum of 49.5%. Form the data in Table 4, the FF value for **P1** devices was higher than those for **P2** and **P3**. The reason may come from the more side alkoxy chain of **P2** and **P3** than those of **P1** which are not favorable the aggregation of the molecules. Thus, with a low equivalent series resistance and a higher equivalent shunt resistance, **P1** devices produced less of the currents which were dissipated in internal losses. According to the cyclic voltammetry result, **P2** and **P3** showed p-type semiconductor properties, therefore, they were used as the donor in the active layer. PSCs based on **P2**:PC₆₁BM and **P3**:PC₆₁BM in a ratio of 1:3 showed the highest PCEs of 0.021 and 0.017%, respectively. As reported, the photovoltaic properties of conjugated polymers are very susceptible to molecular structure, even for the conjugated polymers with identical conjugated main chain while different side chain [32]. Thus, the PCEs of **P2** we obtained were better than that of **P3** in the same ratio of donor to acceptor. Moreover, J_{sc} and the efficiency of all the photovoltaic cells based on **P2** and **P3** are relatively low, probably due to more of side alkoxy chain in **P2** and **P3** which can affect the arrangement of the molecules. It is

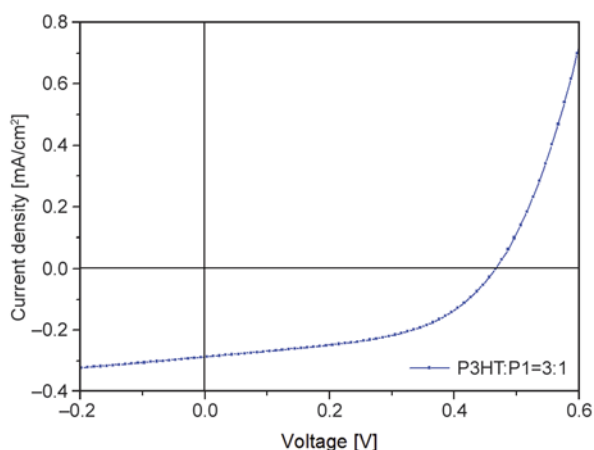


Figure 6. J - V curves of the photovoltaic cells based on **P1** under the illumination of AM 1.5, 100 Mw/cm²

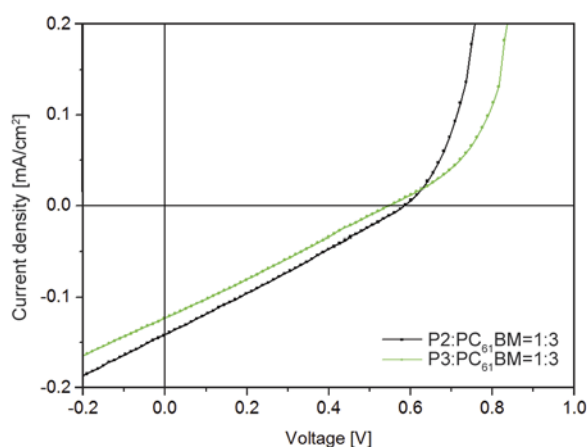


Figure 7. J - V curves of the photovoltaic cells based on **P2** and **P3** under the illumination of AM 1.5, 100 Mw/cm²

unfavorable to charge transfer between donor and acceptor materials.

3.5. Atomic force microscopy (AFM) characterization

To understand the relationship between device performances and active layer morphology, AFM measurements were conducted to investigate the surface morphology of P3HT:**P1** (3:1, w/w), **P2**: PC₆₀BM (1:3, w/w), and **P3**:PC₆₀BM (1:3, w/w) blend films. As shown in Figure 8a, a larger surface roughness and domain size are observed in **P1** with less bulky side chains. In contrast, significantly more homogeneous morphologies are observed from Figures 8b and 8c. Especially more of nanoscale phase separa-

tion and bicontinuous interpenetrating networks can be observed in Figure 8b, which interprets that **P2** has more efficient charge separation and transport than **P3**, and **P2** shows higher J_{sc} than **P3** just as reported in Table 4 [33].

4. Conclusions

In summary, we have successfully synthesized three D–A copolymers containing naphthalenediimide units. All polymers exhibit moderate to high molecular weights, excellent thermal stability and good solubility in common organic solvents. The optical and electrochemical properties indicated that the polymers have broad absorption range and low band gap. With different electron-rich donor units, **P1** shows n-type semiconductor properties, **P2** and **P3** show p-type semiconductor properties. For the first time, the PSCs based on **P1**, **P2** and **P3** were fabricated, with preliminary PCEs of 0.068, 0.021 and 0.017%, respectively. We suppose to change the side chain of the polymers to get a high mobility and optimize the fabricating process of the devices by spinning coated in different solvents and anneal at different temperature, which is our current research interest.

Acknowledgements

The authors express their sincere thanks to Yunbin Hu, Zheng Zhao, Yu Xiong, Jie Li and Prof. Xike Gao in Laboratory of Materials Science, Shanghai Institute of Organic Chemistry for their help in synthesis. This work is supported by Doctoral Fund of Ministry of Education of China (20090075120011), and The National Natural Science Foundation of China (51003012).

References

- [1] Li Y., Guo Q., Li Z., Pei J., Tian W.: Solution processable D–A small molecules for bulk-heterojunction solar cells. *Energy and Environmental Science*, **3**, 1427–1436 (2010). DOI: [10.1039/C003946B](https://doi.org/10.1039/C003946B)
- [2] Treat N. D., Shuttle C. G., Toney M. F., Hawker C. J., Chabinyc M. L.: *In situ* measurement of power conversion efficiency and molecular ordering during thermal annealing in P3HT:PCBM bulk heterojunction solar cells. *Journal of Materials Chemistry*, **21**, 15224–15231 (2011). DOI: [10.1039/C1JM12677F](https://doi.org/10.1039/C1JM12677F)
- [3] Heeger A. J.: Semiconducting polymers: The third generation. *Chemical Society Reviews*, **39**, 2354–2371 (2010). DOI: [10.1039/B914956M](https://doi.org/10.1039/B914956M)

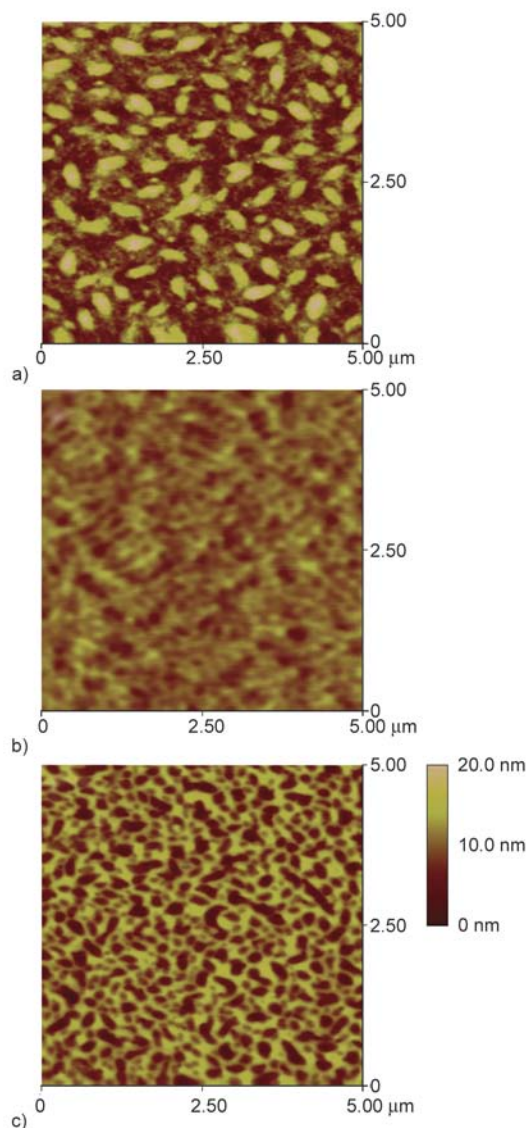


Figure 8. AFM height images ($5 \times 5 \mu\text{m}^2$) of (a) P3HT: **P1** (3:1, w/w), (b) **P2**: PC₆₀BM (1:3, w/w), and (c) **P3**: PC₆₀BM (1:3, w/w) blend films spin coated from chlorobenzene

- [4] Brabec C. J., Sariciftci N. S., Hummelen J. C.: Plastic solar cells. *Advanced Functional Materials*, **11**, 15–26 (2001).
DOI: [10.1002/1616-3028\(200102\)11:1<15::AID-ADFM15>3.0.CO;2-A](https://doi.org/10.1002/1616-3028(200102)11:1<15::AID-ADFM15>3.0.CO;2-A)
- [5] Jørgensen M., Norrman K., Gevorgyan S. A., Tromholt T., Andreasen B., Krebs F. C.: Stability of polymer solar cells. *Advanced Materials*, **24**, 580–612 (2012).
DOI: [10.1002/adma.201104187](https://doi.org/10.1002/adma.201104187)
- [6] Huo L., Huo J., Chen H-Y., Zhang S., Jiang Y., Chen T. L., Yang Y.: Bandgap and molecular level control of the low-bandgap polymers based on 3,6-dithiophen-2-yl-2,5-dihydropyrrolo[3,4-c]pyrrole-1,4-dione toward highly efficient polymer solar cells. *Macromolecules*, **42**, 6564–6571 (2009).
DOI: [10.1021/ma9012972](https://doi.org/10.1021/ma9012972)
- [7] Liang Y., Feng D., Wu Y., Tsai S-T., Li G., Ray C., Yu L.: Highly efficient solar cell polymers developed via fine-tuning of structural and electronic properties. *Journal of the American Chemical Society*, **131**, 7792–7799 (2009).
DOI: [10.1021/ja901545q](https://doi.org/10.1021/ja901545q)
- [8] Liang Y., Xu Z., Xia J., Tsai S-T., Wu Y., Li G., Ray C., Yu L.: For the bright future—bulk heterojunction polymer solar cells with power conversion efficiency of 7.4%. *Advanced Materials*, **22**, E135–E138 (2010).
DOI: [10.1002/adma.200903528](https://doi.org/10.1002/adma.200903528)
- [9] Zhu Y., Champion R. D., Jenekhe S. A.: Conjugated donor–acceptor copolymer semiconductors with large intramolecular charge transfer: Synthesis, optical properties, electrochemistry, and field effect carrier mobility of thienopyrazine-based copolymers. *Macromolecules*, **39**, 8712–8719 (2006).
DOI: [10.1021/ma061861g](https://doi.org/10.1021/ma061861g)
- [10] Durban M. M., Kazarinoff P. D., Luscombe C. K.: Synthesis and characterization of thiophene-containing naphthalene diimide n-type copolymers for OFET applications. *Macromolecules*, **43**, 6348–6352 (2010).
DOI: [10.1021/ma100997g](https://doi.org/10.1021/ma100997g)
- [11] Yan H., Chen Z., Zheng Y., Newman C., Quinn J. R., Dötz F., Kastler M., Facchetti A.: A high-mobility electron-transporting polymer for printed transistors. *Nature*, **457**, 679–686 (2009).
DOI: [10.1038/nature07727](https://doi.org/10.1038/nature07727)
- [12] Gao X., Di C-A., Hu Y., Yang X., Fan H., Zhang F., Liu Y., Li H., Zhu D.: Core-expanded naphthalene diimides fused with 2-(1,3-dithiol-2-ylidene)malonitrile groups for high-performance, ambient-stable, solution-processed n-channel organic thin film transistors. *Journal of the American Chemical Society*, **132**, 3697–3699 (2010).
DOI: [10.1021/ja910667y](https://doi.org/10.1021/ja910667y)
- [13] Kudla C. J., Dolfen D., Schottler K. J., Koenen J-M., Breusov D., Allard S., Scherf U.: Cyclopentadithiazole-based monomers and alternating copolymers. *Macromolecules*, **43**, 7864–7867 (2010).
DOI: [10.1021/ma1014885](https://doi.org/10.1021/ma1014885)
- [14] Ahmed E., Ren G., Kim F. S., Hollenbeck E. C., Jenekhe S. A.: Design of new electron acceptor materials for organic photovoltaics: Synthesis, electron transport, photophysics, and photovoltaic properties of oligothiophene-functionalized naphthalene diimides. *Chemistry of Materials*, **23**, 4563–4577 (2011).
DOI: [10.1021/cm2019668](https://doi.org/10.1021/cm2019668)
- [15] Mishra A., Bäuerle P.: Small molecule organic semiconductors on the move: promises for future solar energy technology. *Angewandte Chemie International Edition*, **51**, 2020–2067 (2012).
DOI: [10.1002/anie.201102326](https://doi.org/10.1002/anie.201102326)
- [16] Thalacker C., Röger C., Würthner F.: Synthesis and optical and redox properties of core-substituted naphthalene diimide dyes. *Journal of Organic Chemistry*, **71**, 8098–8105 (2006).
DOI: [10.1021/jo0612269](https://doi.org/10.1021/jo0612269)
- [17] Chen Z., Zheng Y., Yan H., Facchetti A.: Naphthalenedicarboximide- vs perylenedicarboximide-based copolymers. Synthesis and semiconducting properties in bottom-gate n-channel organic transistors. *Journal of the American Chemical Society*, **131**, 8–9 (2009).
DOI: [10.1021/ja805407g](https://doi.org/10.1021/ja805407g)
- [18] Fuller L. S., Iddon B., Smith K. A.: Thienothiophenes. Part 2.¹ Synthesis, metallation and bromine→lithium exchange reactions of thieno[3,2-*b*]thiophene and its polybromo derivatives. *Journal of the Chemical Society, Perkin Transactions 1*, **1**, 3465–3470 (1997).
DOI: [10.1039/A701877K](https://doi.org/10.1039/A701877K)
- [19] Yuan Z., Xiao Y., Yang Y., Xiong T.: Soluble ladder conjugated polymer composed of perylenediimides and thieno[3,2-*b*]thiophene (LCPT): A highly efficient synthesis via photocyclization with the sunlight. *Macromolecules*, **44**, 1788–1791 (2011).
DOI: [10.1021/ma1026252](https://doi.org/10.1021/ma1026252)
- [20] Wen S., Cheng W., Li P., Yao S., Xu B., Li H., Gao Y., Wang Z., Tian W.: Synthesis and photovoltaic properties of thieno[3,4-*c*]pyrrole-4,6-dione-based donor–acceptor copolymers. *Journal of Polymer Science Part A: Polymer Chemistry*, **50**, 3758–3766 (2012).
DOI: [10.1002/pola.26164](https://doi.org/10.1002/pola.26164)
- [21] Chen J., Shi M-M., Hu X-L., Wang M., Chen H-Z.: Conjugated polymers based on benzodithiophene and arylene imides: Extended absorptions and tunable electrochemical properties. *Polymer*, **51**, 2897–2902 (2010).
DOI: [10.1016/j.polymer.2010.04.035](https://doi.org/10.1016/j.polymer.2010.04.035)
- [22] Li Y.: Molecular design of photovoltaic materials for polymer solar cells: Toward suitable electronic energy levels and broad absorption. *Accounts of Chemical Research*, **45**, 723–733 (2012).
DOI: [10.1021/ar2002446](https://doi.org/10.1021/ar2002446)
- [23] Cao J., Zhang W., Xiao Z., Liao L., Zhu W., Zou Q., Ding L.: Synthesis and photovoltaic properties of low band gap polymers containing benzo[1,2-*b*:4,5-*c'*]dithiophene-4,8-dione. *Macromolecules*, **45**, 1710–1714 (2012).
DOI: [10.1021/ma202578y](https://doi.org/10.1021/ma202578y)

- [24] Zhang M., Guo X., Li Y.: Photovoltaic performance improvement of D–A copolymers containing bithiazole acceptor unit by using bithiophene bridges. *Macromolecules*, **44**, 8798–8804 (2011). DOI: [10.1021/ma201976t](https://doi.org/10.1021/ma201976t)
- [25] Wang X., Sun Y., Chen S., Guo X., Zhang M., Li X., Li Y., Wang H.: Effects of π -conjugated bridges on photovoltaic properties of donor- π -acceptor conjugated copolymers. *Macromolecules*, **45**, 1208–1216 (2012). DOI: [10.1021/ma202656b](https://doi.org/10.1021/ma202656b)
- [26] Wakim S., Alem S., Li Z., Zhang Y., Tse S-C., Lu J., Ding J., Tao Y.: New low band gap thieno[3,4-*b*]thiophene-based polymers with deep HOMO levels for organic solar cells. *Journal of Materials Chemistry*, **21**, 10920–10928 (2011). DOI: [10.1039/c1jm11229e](https://doi.org/10.1039/c1jm11229e)
- [27] Chen S., Bolag A., Nishida J-I., Yamashita Y.: n-type field-effect transistors based on thieno[3,2-*b*]thiophene-2,5-dione and the bis(dicyanomethylene) derivatives. *Chemistry Letters*, **40**, 998–1000 (2011). DOI: [10.1246/cl.2011.998](https://doi.org/10.1246/cl.2011.998)
- [28] Zhou E., Cong J., Wei Q., Tajima K., Yang C., Hashimoto K.: All-polymer solar cells from perylene diimide based copolymers: Material design and phase separation control. *Angewandte Chemie International Edition*, **50**, 2799–2803 (2011). DOI: [10.1002/anie.2011005408](https://doi.org/10.1002/anie.2011005408)
- [29] Lin L-Y., Chen Y-H., Huang Z-H., Lin H-W., Chou S-H., Lin F., Chen C-W., Liu Y-H., Wong K-T.: A low-energy-gap organic dye for high-performance small-molecule organic solar cells. *Journal of the American Chemical Society*, **133**, 15822–15825 (2011). DOI: [10.1021/ja205126t](https://doi.org/10.1021/ja205126t)
- [30] Zhou E., Cong J., Zhao M., Zhang L., Hashimoto K., Tajima K.: Synthesis and application of poly(fluorene-*alt*-naphthalene diimide) as an n-type polymer for all-polymer solar cells. *Chemical Communications*, **48**, 5283–5285 (2012). DOI: [10.1039/C2CC31752D](https://doi.org/10.1039/C2CC31752D)
- [31] Hwang Y-J., Ren G., Murari N. M., Jenekhe S. A.: n-type naphthalene diimide–biselenophene copolymer for all-polymer bulk heterojunction solar cells. *Macromolecules*, **45**, 9056–9062 (2012). DOI: [10.1021/ma3020239](https://doi.org/10.1021/ma3020239)
- [32] Nam C-Y., Qin Y., Park Y. S., Hlaing H., Lu X., Ocko B. M., Black C. T., Grubbs R. B.: Photo-cross-linkable azide-functionalized polythiophene for thermally stable bulk heterojunction solar cells. *Macromolecules*, **45**, 2338–2347 (2012). DOI: [10.1021/ma3001725](https://doi.org/10.1021/ma3001725)
- [33] Bedford N. M., Dickerson M. B., Drummy L. F., Koerner H., Singh K. M., Vasudev M. C., Durstock M. F., Naik R. R., Steckl A.: Nanofiber-based bulk-heterojunction organic solar cells using coaxial electrospinning. *Advanced Energy Materials*, **2**, 1136–1144 (2012). DOI: [10.1002/aenm.201100674](https://doi.org/10.1002/aenm.201100674)

Development of bio-based thermoplastic polyurethanes formulations using corn-derived chain extender for reactive rotational molding

B. J. Rashmi, D. Rusu, K. Prashantha*, M-F. Lacrampe, P. Krawczak

Mines Douai, Department of Polymers and Composites Technology & Mechanical Engineering, 941 rue Charles Bourseul, CS 10838, F-59508 Douai Cedex, France

Received 25 April 2013; accepted in revised form 24 June 2013

Abstract. Partly bio-based segmented thermoplastic polyurethane (TPU) formulations were developed to fulfill the requirements of the reactive rotational molding process. They were obtained by one-shot bulk polymerization between an aliphatic diisocyanate (1,6-hexamethylene diisocyanate), a polyether polyol as macrodiol (polyethylene glycol) and a bio-based corn-derived 1,3-propanediol as chain extender (CE), in presence of a catalyst, at an initial temperature of 45°C. Equivalent TPU formulations with classical petroleum-based 1,3-propanediol were also prepared for a purpose of comparison. TPU with different soft to hard segment (SS/HS) ratios were synthesized by varying the macrodiol and CE concentrations in the formulations. For each formulation, the evolution of the reaction temperature as a function of time was monitored and the kinetics of polymerization was studied by Fourier Transform infrared spectroscopy in attenuated total reflection mode (FTIR-ATR). The morphology, thermal properties, solubility in different solvents and tensile properties of the final products were analyzed. All synthesized polyurethanes are 100% linear polymers and the extent of microphase separation, as well as the thermal and mechanical properties highly depends on the HS content, and glass transition temperature and Young modulus can be tuned by adjustment of the SS/HS ratio. All results indicate that petrochemical CE can be replaced by its recently available corn-derived homologue, without sacrificing any use properties of the final polyurethanes.

Keywords: processing technologies, thermoplastic polyurethanes, bio-based polymers, thermal behavior, mechanical properties

1. Introduction

From chemical point of view, segmented thermoplastic polyurethanes (TPUs) are linear multiblock copolymers consisting of alternating ‘soft’ polyether or polyester segments (SS) and ‘hard’ urethane segments (HS). The thermodynamic incompatibility between the low polarity SS, which are rubbery at usage temperatures, and the high polarity HS, which are vitreous in the same conditions [1–3], induces a micro-phase separation and the formation of HS domains and SS domains, with ill-defined inter-phases. At usage temperatures, the HS domains act as both physical cross-links and filler particles

embedded within the SS matrix [3]. In these conditions, the segmented TPUs behave as elastomers. However, the physical cross-links disappear under heating or in presence of an efficient solvent, and in that case, the multiblock copolymers behave as classical linear thermoplastics.

Basically, TPUs are produced from petroleum-based raw materials, i.e., diisocyanates, polyols and chain extenders. However, it has been demonstrated that at least part of the conventional petroleum-based polyols can be replaced by renewable resources-based equivalent compounds such as vegetable oils [4–7], and now, a major part of bio-based raw mate-

*Corresponding author, e-mail: kalappa.prashantha@mines-douai.fr
© BME-PT

rials derived from plant oils and natural fats is dedicated to polyurethane industry [4, 5]. However, most of the reported bio-based polyurethanes are chemically cross-linked networks (thermosets) [6–9], except for a very few reports on syntheses of thermoplastics using either methanolysis, metathesis or an ozonolysis pathway, which means some parts of the original triacylglycerol were not utilized [10, 13], and for the very recent renewable-sourced thermoplastic polyurethanes Pearlthane[®] ECO from Merquinsa [9].

The approach adopted in this paper aims at developing partially bio-based TPU formulations suitable for reactive rotational molding (RRM), as previously achieved for TPU foams [5]. To the best of our knowledge, the following report is the first to address this approach in the case of bulk TPUs. The chosen polymerization system is based on the synthesis of segmented TPUs starting from an aliphatic diisocyanate, a polyether polyol as macrodiol and a bio-based short diol as chain extender (CE), in presence of a catalyst. For further application, the system should be suitable for RRM and thus the polymerization has to be made in one-step at ambient or slightly higher temperature, the product should be formed in relatively short time (~20 minutes). Moreover, the final product should be thermoplastic, to allow easy recycling. TPUs with synthetic CE are also going to be synthesized and the thermal and mechanical properties of the petrochemical and bio-based materials will be compared.

2. Experimental

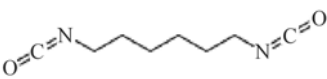
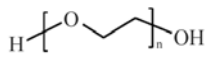


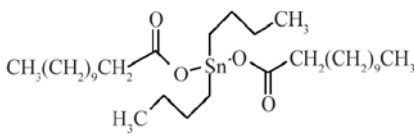
2.1. Materials

The TPU formulations are based on 1,6-hexamethylene diisocyanate (HDI, Sigma Aldrich, France), polyethylene glycol (PEG 1000, VWR International, France) as macrodiol, 1,3-propanediol (PDO, Sigma Aldrich, France) as petrochemical CE or Susterra[®] 1,3-propanediol (bio-PDO[™], DuPont Tate & Lyle Bio Products, USA) as bio-based CE, which is a 100% renewably sourced material derived from corn sugar, in presence of dibutyl tin dilaurate (DBTDL, Fluka, France) as catalyst (Table 1). In order to limit the unwanted side reactions between diisocyanate and water traces, the raw materials were dried prior to TPU synthesis (under vacuum at 80°C for minimum 3 h for PEG and 1 h for CE, by bubbling nitrogen for 2 h for HDI). The DBTDL catalyst was used as received.

2.2. Polyurethane synthesis

All TPU samples were synthesized by one-step bulk polymerization. The polymerization was carried out in a semi-closed beaker, to minimize side reactions with water traces from atmosphere. The synthesis was carried out in a 100 mL beaker placed in an oil bath, equipped with a magnetic stirrer, under hood extractor. A required amount of catalyst was placed in the beaker. Then, the prescribed amounts of PEG and PDO were added under continuous stirring. Once the mixture was homogenous and the required temperature (45°C) attained, the predetermined amount of HDI was added by means of a syringe

Table 1. Characteristics of the raw materials used in this study (according to suppliers' data)

Role	Chemicals	Structure	M ^a [g/mol]	Physical state at T _{ambient}	T _m ^b [°C]	Density [g/cm ³]	Fn ^c
Diisocyanate	HDI		168	Viscous liquid	-67	1.047	2
Macrodiol	PEG 1000		1000	Waxy solid	37–40	1.1–1.2	2
Chain extender	PDO		76	Clear liquid	-30	1.050	2
Chain extender	Bio PDO		76	Clear liquid	-30	1.050	2
Catalyst	DBTDL		632	Liquid	10	1.050	–

^aM – Molecular weight,

^bT_m – Melting temperature,

^cFn – Functionality

Table 2. Formulations of prepared TPUs

Formulation code	Macrodiol	Chain extender	Catalyst	Diisocyanate	Hard segment content ^b [wt%]
	PEG [g]	PDO/Bio PDO [mL]	DBTDL [10 ⁻³ mL]	HDI ^a [mL]	
TPU 912/Bio-TPU 912	9	1	2	4.5	35
TPU 822 Bio-TPU 822	8	2		6.5	51
TPU 732/Bio-TPU 732	7	3		8.5	62
TPU 552/Bio-TPU 552	5	5		13.5	78
HDI-PDO/HDI-Bio PDO	0	10		23.0	100
TPU 914/Bio-TPU 914	9	1	4	4.5	35
TPU 824/Bio-TPU 824	8	2		6.5	51
TPU 734/Bio-TPU 734	7	3		8.5	62
TPU 554/Bio-TPU 554	5	5		13.5	78
HDI-PDO/HDI-Bio PDO	0	10		23.0	100

^aRequired diisocyanate = $I_{NCO/OH} E_{HDI} (V_{PEG}/E_{PEG} + V_{PDO}/E_{PDO})$ where, $I_{NCO/OH}$ the ratio of NCO/OH, E_{HDI} , E_{PEG} et E_{PDO} are equivalent weights of diisocyanate, PEG and PDO respectively, and V_{PEG} et V_{PDO} are volumes of PEG and PDO, respectively.

^bThe hard segment content [wt%] = $(W_{HS})/(W_{SS} + W_{HS})$ where W_{HS} ≡ weight of HDI + PDO, and W_{SS} ≡ weight of PEG in grams.

and the stirring was continued. The polymerization was assumed to start directly after the addition of diisocyanate. The stirring was continued until the increase in viscosity made stirring impossible. The synthesized polyurethanes were then collected in an air tight container and kept for conditioning ($23 \pm 2^\circ\text{C}$, $50 \pm 5\%$ relative humidity) for one week at least before further testing.

Different formulations were prepared (Table 2) varying by macrodiol/CE ratio and catalyst concentration. The molar ratio NCO/OH (NCO index of 1.05) and the bath temperature were kept constant. The amount of diisocyanate to be added to each formulation was based on the total hydroxyl content of the diols.

Bio-based TPU samples were named as ‘Bio-TPU XYZ’, where ‘X’ indicates the amount of polyol, ‘Y’ the amount of CE, and ‘Z’ the concentration of catalyst; For instance, TPU 912 corresponds to the

formulation with 90% of PEG, 10% PDO, and 0.02 %vol catalyst, respectively. The equivalent non bio-TPUs were prepared with same formulations (but petrochemical PDO) and same polymerization procedure. They were named simply ‘TPU XYZ’. The general polyaddition reaction is presented in Figure 1.

2.3. Characterization methods

2.3.1. Adiabatic temperature rise

The evolution of reaction temperature as a function of time was monitored and recorded using a house made type J thermocouple placed in the reactive system. Addition of HDI was considered as the zero time of the polymerization reaction.

2.3.2. Fourier transform infrared spectroscopy

A Fourier-transform infrared spectroscopy (FTIR) analyzer (Nicolet 380 FTIR, Thermo Scientific,

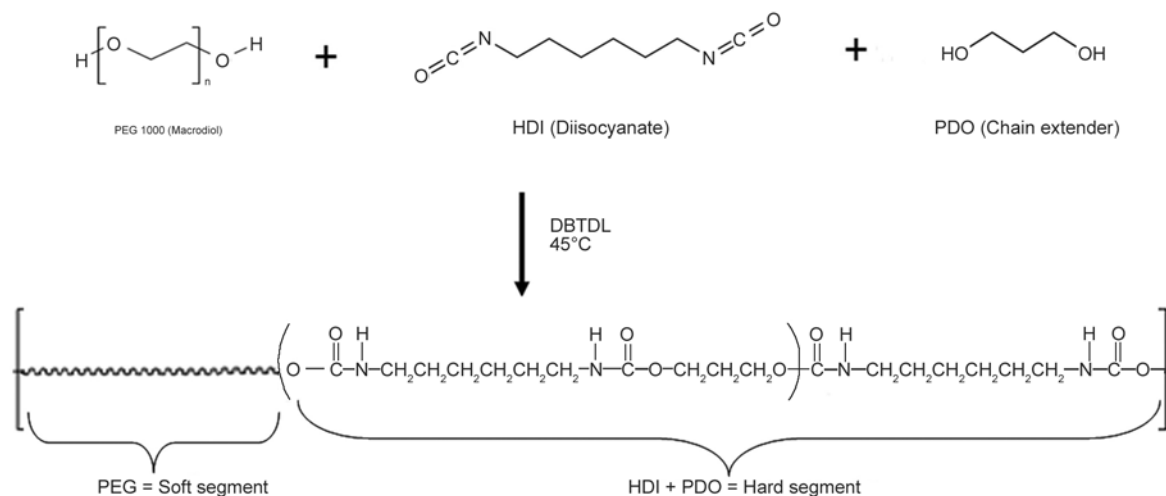


Figure 1. One-step bulk polyaddition of PEG, PDO and HDI to form segmented TPUs (PEG forms the soft segments, while HDI and PDO form the HS)

USA, with OMNIC software for data collection and analysis) equipped with attenuated total reflectance (ATR) attachment was used to record FTIR-ATR spectra for the reaction mixture, at different reaction times, and for the final TPUs. Approximately 40–45 mg of the sample was removed from the reaction flask for each analysis and placed on the ATR crystal. A total of 64 scans were taken on each sample over the wavelength range of 4000 to 400 cm^{-1} at a resolution of 4 cm^{-1} . Three FTIR-ATR spectra were collected at different locations of the sample to verify its uniformity. Three samples were tested for each formulation.

2.3.3. Scanning electron microscopy

The morphology of cryofractured samples (whose surface was coated with a thin gold layer) of the developed polyurethanes was observed under high vacuum with a Scanning Electron Microscope (SEM, S-4300SE/N, Hitachi, Japan) operating at 5 kV.

2.3.4. Solubility

Solubility of polyurethanes was determined in different organic solvents, such as methyl ethyl ketone (MEK), dimethyl sulfoxide (DMSO), dimethyl formamide (DMF), and dimethyl acetamide (DMAc). Experiments were carried out at room temperature for 48 h. The amount of polymer sample and solvents are 10 mg and 1 mL, respectively.

2.3.5. Thermal analysis

Thermal transitions of the final products were analyzed by Differential Scanning Calorimetry (DSC 7, Perkin-Elmer Pyris). Samples of about 5.5 ± 0.1 mg were sealed in aluminium pans. An initial heating to 180°C was carried out and held isothermally for one minute to erase all thermal history of the samples. Subsequent cooling (from 180 to –70°C) and heating (from –70 to 200°C) were carried out at 10°C/min. The first cooling and second heating thermograms were recorded. From all DSC thermographs presented in this study, a baseline, obtained by running an empty pan in the same conditions as the sample, was subtracted and, for comparison purpose, all the thermographs were normalized by the weight of the sample.

2.3.6. Tensile testing

The Young modulus, ultimate tensile strength and elongation at break of each formulation were deter-

mined using standard tensile machine (LR 50K, Lloyd, Bognor Regis, United Kingdom) at a crosshead speed of 10 mm/min. Dumbbell-shaped TPU samples were prepared by cutting from 2 mm thick compression-molded sheets. Compression molding was carried out using a hydraulic press (Dolouets, France) at 100 bars and temperature ranging from 135 to 165°C depending on the melting point of formulation. Then samples were cooled to ambient temperature. All the reported values were calculated as average over five specimens at least for each TPU formulation.

3. Results and discussion

3.1. Fourier transform infrared spectroscopy

FTIR was used to check the final chemical composition of TPU and the relative degree of phase separation due to thermodynamics, mobility and crystallization. Distinct bands related to amine, methylene, carbonyl, and PEG ether were observed at 3320, 2940, 1714 and 1685, and 1110 cm^{-1} , respectively in FTIR spectra shown in Figure 2. Figure 2a shows that equivalent bio- and non bio-TPU formulations give similar chemical structures/extent in phase separation. The lack of an isocyanate peak at 2270 cm^{-1} and the presence of the amine and carbonyl peaks indicate a complete conversion of monomers to urethane [3, 12, 13]. As both soft (PEG) and hard (HDI-PDO) segments forming the final products can crystallize, the strong drive towards crystallization within the HDI-PDO hard segment is expected to improve the degree of phase separation by excluding SS from the crystalline HS domains. The extent of hydrogen bonding of the urethane carbonyl can approximate the degree of phase separation. The extent and type of hydrogen bonding can be inferred by observing the intensities of the carbonyl ‘shoulder’ at 1714 cm^{-1} and of the PEG peak and its breadth at 1110 cm^{-1} . It was reported [11–13] that the carbonyl peak can be separated into three regions, related to different types of hydrogen bonding in segmented TPUs. Carbonyl not involved in hydrogen bonding has peaks observed near 1732 cm^{-1} , whereas carbonyl associated with poorly ordered hydrogen bonding was observed at 1714 cm^{-1} and well organized carbonyl, strongly hydrogen bonded to amines, was observed around 1685 cm^{-1} [11–13]. Accordingly, it is possible to attribute the 1685 and 1714 cm^{-1} bands to strong and poorly hydrogen-bonded carbonyl groups, respec-

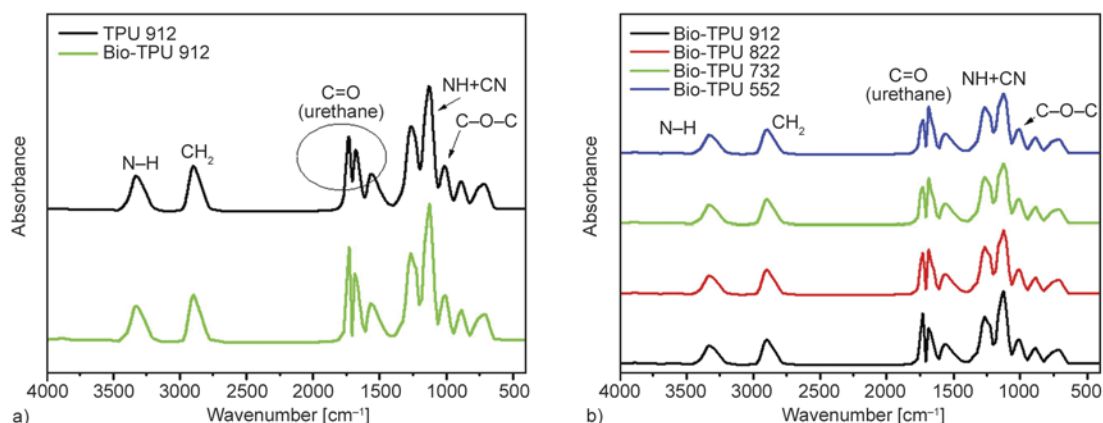


Figure 2. Typical FTIR spectra of (a) TPU 912 and bio-TPU 912 (b) bio-TPU series with different HS content (i.e., different macrodiol/chain extender ratios) and constant catalyst concentration (0.02 vol%)

tively. So, the strong hydrogen-bonded C=O groups could be directly related to important phase separation, while the poorly hydrogen-bonded carbonyl groups correspond more to a mixing phase. A closer look on the influence of the HS content on the extent of phase separation, as detectable by FTIR (Figure 2b), indicates that an increase in HS content, induced an increase in the intensity of C=O peak at 1685 cm^{-1} , indicating the formation of larger HS domains, i.e. a more effective phase separation. Moreover, the amine peak at 3320 cm^{-1} appeared to be narrow and relatively symmetric, which normally suggests the absence of a significant number of free amines to be detected by FTIR. In fact, if the mixing phase was prevalent, a shoulder on the high-frequency side of the 3320 cm^{-1} band would appear, related to free amine, and the full-width at half-maximum would be broad, which was not observed here [11–13].

3.2. Temperature rise as a function of time

Figure 3 shows the temperature rise profiles as a function of reaction process time for bio-based samples at different macrodiol/CE ratios and catalyst concentrations (0.02, and 0.04 vol% of total reaction mixture). Non bio-based samples show similar temperature profiles (not reported here). The reaction rate and exothermicity effect increased with increasing CE content, i.e., decreasing the macrodiol/CE ratio, and did not change noticeably with catalyst concentration. Therefore, further tests were performed only for one catalyst concentration, 0.02 vol%. The higher exothermicity and reaction rate observed in Figure 3a, with the increase in HS content, can be related to the increase in number of polyaddition reactions per mole of polyurethane. In fact, both PDO (chain extender) and PEG (macrodiol) have two OH groups per molecule, but their molecular weight is very different, i.e. 76 g/mol for

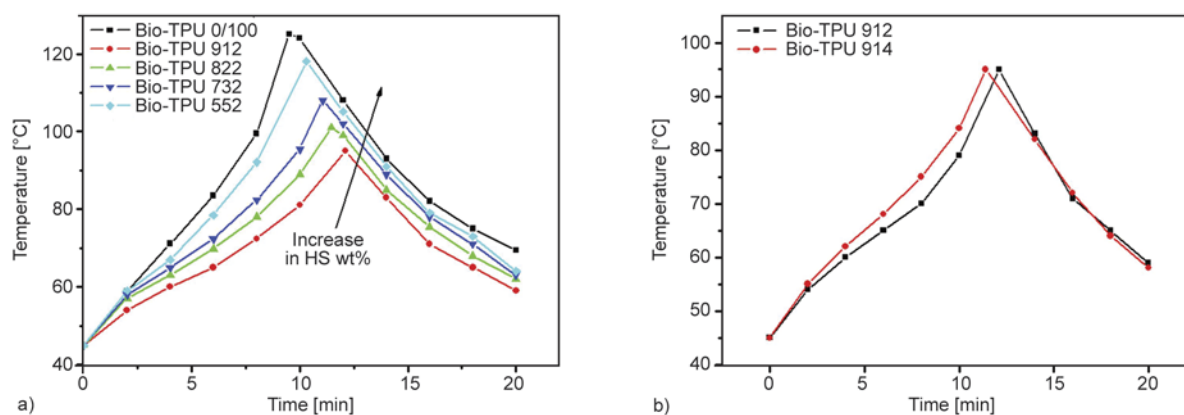


Figure 3. Adiabatic temperatures rise as a function of time for: (a) a bio-TPU series with different macrodiol/CE ratios and constant catalyst concentration (0.02 vol%), and (b) a bio-TPU series with constant macrodiol/CE ratios (90/10) and different catalyst concentration

PDO and 1000 g/mol for PEG used in this study. It means that 100 g of PDO approximately contains 3.6 moles of OH groups, whereas PEG contains 0.2 moles. As mentioned above (section §2.2), the molar ratio of isocyanate groups to hydroxyl groups (NCO/OH) was kept constant at 1.05 for all formulations. Therefore, samples with a higher CE concentration contained a higher number of hydroxyl groups, which caused more urethane linkages between OH groups and NCO groups and so the release of a higher quantity of heat.

3.3. Polymerization kinetics

Traditionally, the kinetics of polyurethane formation was extensively monitored by two direct methods that measure the concentration of reactant or reaction products: standard dibutylamine back titration and FTIR spectroscopy [14–16]. Back-titration is a well-known method for conventionally titrating for free isocyanate content; however, it is both time and chemical consuming. FTIR spectroscopy is a good alternative, but presents some practical limitations due to the requirements in sample preparation. Another possibility is to use the FTIR in ATR mode, which can monitor the polyurethanes formation, as recently suggested in the literature [6, 17, 18]. It allows the analysis of smaller samples without additional preparation. In this study, the FTIR-ATR was used to determine the isocyanate conversion during polyurethane formation. Generally, the kinetics of bulk polymerization of polyurethanes (both catalysed and non-catalysed ways) is considered to fit the overall expression of second order [19–22]. The isocyanate absorption band is assigned at approximately 2270 cm^{-1} , and the decay in intensity of this absorbance was used to monitor the isocyanate group conversion during the polymerization. To determine isocyanates conversion during polymerization, a ratio between the absorbance of -NCO group and an internal standard CH_2 stretching has to be considered, this second group exhibiting constant concentration during polymerization. The absorbance corresponding to the CH_2 stretching region, assigned at approximately $2800\text{--}2900\text{ cm}^{-1}$, was used.

Figure 4 presents an example of evolution of FTIR-ATR spectra during polyurethane synthesis, and Figure 5 illustrates the corresponding evolution of the relative intensity of absorbance, $A_{\text{NCO}}/A_{\text{CH}_2}$, and the calculated isocyanate conversion respec-

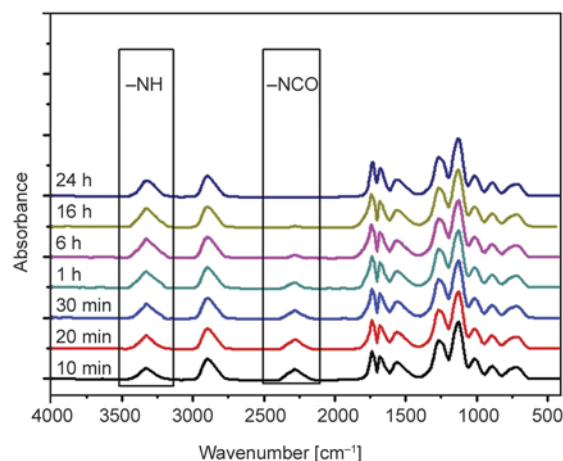


Figure 4. FTIR spectra of bio-TPU 912 at different reaction time intervals

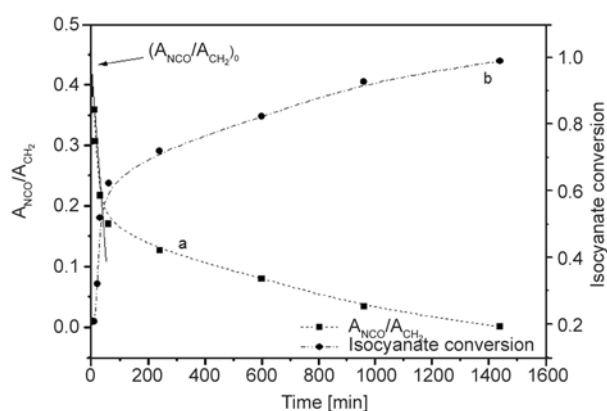


Figure 5. Decay in the relative absorbance ($A_{\text{NCO}}/A_{\text{CH}_2}$) (a) and the corresponding calculated isocyanate conversion ($p = 1 - (A_{\text{NCO}}/A_{\text{CH}_2}) / (A_{\text{NCO}}/A_{\text{CH}_2})_0$) (b). A_{NCO} is the integrated absorbance for the isocyanate group, A_{CH_2} is the integrated absorbance for the CH_2 group and $(A_{\text{NCO}}/A_{\text{CH}_2})_0$ is the relative absorbance extrapolated for time zero.

tively. Complete conversion of isocyanates to polyurethane occurred after 24 hours of reaction. However 30 min after the beginning of polymerization (target time from the viewpoint of further rotational molding application), the conversion of isocyanate groups approached 0.6, and the polyurethane samples were in a solid state with air bubbles in the sample.

3.4. Scanning electron microscopy

Figure 6 shows a typical example of SEM micrographs of segmented Bio-TPUs. As expected from literature data reported for different segmented polyurethanes [3, 11, 23, 24], the TPUs developed in the present study exhibited a hetero-phase structure consisting of hard and soft domains.

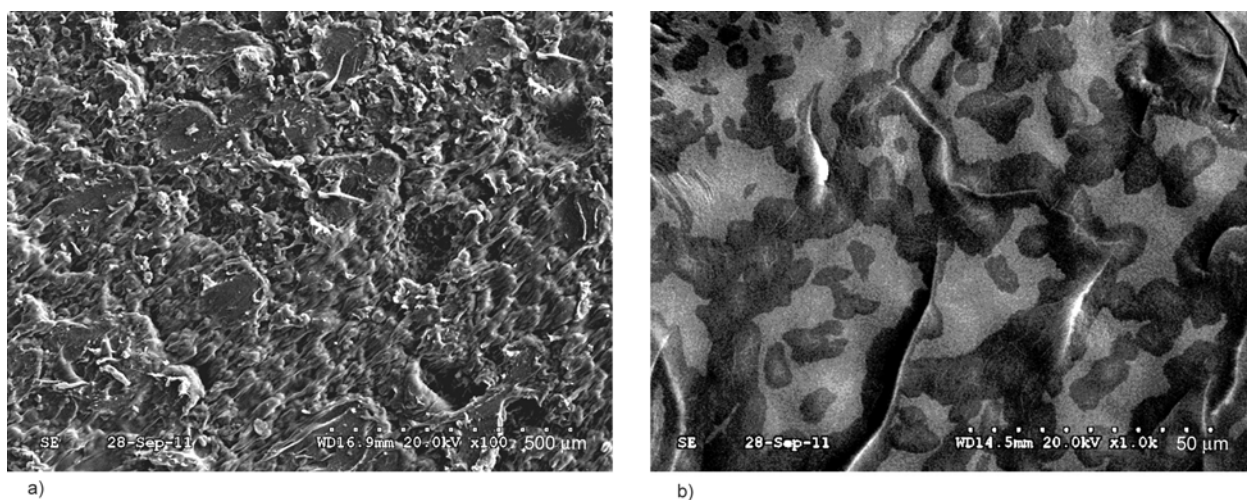


Figure 6. SEM micrographs of fractured surface of bio-TPU 822, with lower (a) and higher (b) magnifications

The thermodynamic incompatibility between the chemically dissimilar HS and SS blocks, on one hand, and the crystallization tendency of both kinds of segments, on another hand, prevented the formation of a homogeneous mixing structure. One should keep in mind that the polymerization system was kept at 45°C, at the beginning of synthesis, then the temperature of the system greatly increased as a consequence of the exothermic polymerization, and the cooling down to ambient temperature was gradual, until reaching the complete conversion of isocyanate groups (after 24 hours). These experimental conditions were favorable to a good phase separation, which is normally more difficult to reach during a relative fast (20–30 min) one-shot bulk polymerization.

3.5. Thermal behavior

Segmented TPUs generally display several thermal transitions, corresponding to the soft and hard micro-domains. So, the SS could present a (low) glass transition temperature, and, if semi-crystalline, a melting transition, whereas the HS may display a glass transition and/or multiple melting transitions. In the present study, the glass transitions (T_g) and melting peaks (T_m) of SS and HS were determined using DSC. First cooling and second heating curves were used to compare the thermal behavior of samples.

Table 3 shows a summary of the results of the DSC thermograms for all the samples. Similar thermal behavior was observed for the non bio-TPU samples, suggesting that Bio-PDO™ and petrochemical

Table 3. Thermal properties of SS and HS domains of the investigated TPUs

Sample	HS content [wt%]	SS domain				HS domain			
		T_g^a [°C]	T_m^b [°C]	T_c^c [°C]	ΔH_f^d	T_g^a [°C]	T_m^b [°C]	T_c^c [°C]	ΔH_f^d
PEG 1000	–	–57	37	18	154	–	–	–	–
TPU 912	35	–55	16	–4	106	90	127	96	108
TPU 822	51	–52	14	–7	79	92	146	104	117
TPU 732	62	–48	12	–9	66	95	150	111	122
TPU 552	78	–30	9	–12	51	97	154	116	137
HDI-PDO	100	–	–	–	–	103	161	131	146
Bio-TPU 912	35	–54	16	–3	105	89	128	98	109
Bio-TPU 822	51	–52	14	–7	79	92	145	103	116
Bio-TPU 732	62	–49	12	–10	67	94	149	109	120
Bio-TPU 552	78	–32	10	–13	50	98	155	118	138
HDI-Bio PDO	100	–	–	–	–	102	160	129	145

The thermal behavior of the pure SS and HS are also included.

^aGlass transition temperature obtained from the second heating curve.

^bMelting transition obtained from the second heating curve.

^cCrystallization temperature obtained from the first cooling curve.

^dEnthalpy of fusion values are per gram of SS and HS, respectively.

PDO gave equivalent TPU, from the viewpoint of crystallization and extent of phase separation. The second heating DSC thermograms had shown two T_g s of SS and HS and two clear endotherms, attributed to the T_m of the SS and HS. The T_g of SS domains was systematically higher than for the native PEG, the difference increasing slowly but continuously with increasing in HS content. Similar results were reported by Korley *et al.* [24] on HDI-BDO-PEG polyurethanes, and this indicates the presence of soft segment crystallites which restrict the mobility of the neighboring amorphous chains and so, increase the glass transition temperature of the soft domains. The SS regions of the polyurethanes developed in the present work showed a melting peak between 9 and 16°C, noticeably lower than the native PEG (37°C). Thus, although the SS do exhibit some crystallization, the crystallites are relatively less stable and less organized than in the native PEG. From practical viewpoint, this decrease in the melting temperature largely below the ambient temperature is expected to be present for the first run too, and will affect the mechanical properties (modulus) of the soft phase domains.

The pure hard segment polymers, called here HDI-PDO and HDI-Bio PDO, exhibited a melting peak at 160–161°C, on the second heating cycle as shown in Table 3. As the HS content increased, the HS endothermic peak shifted towards lower temperatures, and the melting of fusion of HS also decreased, as reported in literature for HDI-BDO-PEG polyurethanes [24]. Here, the HS domains of the developed HDI-PDO-PEG polyurethanes exhibited a T_g within the range of 89–98°C, depending on the HS content. Further, the T_g of pure HS was found to be 102°C (Table 3). Recent results on HDI-BDO-PEG polyurethanes with high %HS content (>45 wt% HS), obtained by one-shot polymerization in solution, indicated that it was impossible to observe glass transition for HS domains, at heating rates of 5 and 40°C/min [11]. This was ascribed to the relatively high degree of crystallization of HS domains, as indicated by the high T_m values of their HS domains, as compared to pure HDI-BDO polymers, and to the small changes in heat capacity. In the present work, the HS domains presented a lower degree of crystallization, and this allowed us to observe the glass transition of the HS.

A decrease in the soft segment crystallization temperature with increasing HS content was observed

(Table 3). The area of crystallization peak decreased in the same sense and showed that the TPUs with more than 50% HS contents developed in the present study present an important part of the SS domains an amorphous state. On the other hand, the crystallinity of the HS domains from segmented TPUs was also much lower as compared with non-segmented HDI-PDO polyurethane. This was recently attributed to the ‘soft confinement effect’ in which a certain degree of phase mixing between the HS and SS occurs, which decreases the HS crystallinity [11].

3.6. Solubility

Solubility of both series of non bio and Bio-TPU samples was determined in different organic solvents and the results are summarized in Table 4. All TPU samples were found to be fully soluble in DMSO, DMF and DMAc and insoluble in MEK. These confirmed that all the samples produced were linear copolymers, without any observable crosslinking that could appear as a consequence of allophanate formation or other unwanted secondary reactions which may occur during polyurethane synthesis.

Table 4. Solubility of polyurethanes prepared

Sample	Solvent			
	MEK	DMSO	DMF	DMAc
TPU 912/Bio-TPU 912	–	+	+	+
TPU 822/Bio-TPU 822	–	+	+	+
TPU 732/Bio-TPU 732	–	+	+	+
TPU 552/Bio-TPU 552	–	+	+	+

+ soluble; – insoluble.

3.7. Mechanical behavior in tension

Figure 7 shows typical tensile stress-strain curves of non-bio and Bio-TPU 732 samples, recorded at room temperature. Similar mechanical behavior was observed for Bio-TPU samples and equivalent non bio-TPUs. The elongation-at-break, ultimate tensile strength, and tensile modulus for all synthesized polyurethanes are outlined in Table 5.

At lower HS fractions, the hard segments aggregate to form hard domains, which serve as reinforcing fillers, in a SS matrix. As the HS content increased, the mechanical data are consistent with a shift in continuous domain morphology, with a better phase separation and an increase in the HS crystallinity. As expected, the TPUs with higher HS contents

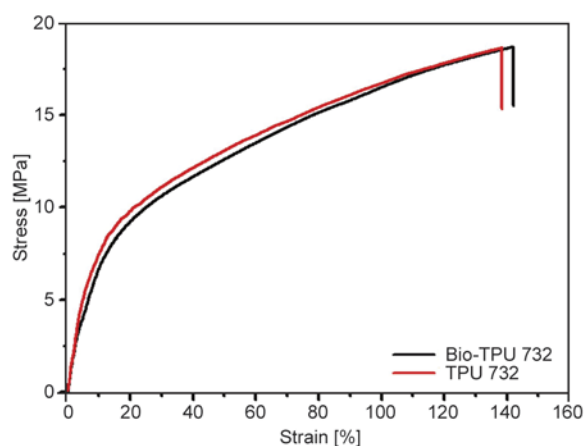


Figure 7. Typical stress-strain curve for non bio and bio-TPU (732) samples

exhibit limited extensibility, but increased tensile modulus, as shown in Table 5.

It is notable that the melting point of SS is just below room temperature (between 9 and 16°C, depending on TPU formulation), and this is significant with respect to deformation mechanism. Even relatively low strains would be expected to induce strain-induced SS crystallization, but the low melting temperature also implies relatively high mobility of the SS chains, thus crystallites may be formed and deformed simultaneously throughout the deformation process. This form of transient, reformable order may play a role in toughening of the polymer matrix, much as observed in a number of naturally occurring materials [25]. The properties of the prepared TPU samples are comparatively lower to those of PUs obtained from prepolymer-based polymerization in solution, which make ‘one-shot’ technique applicability limited [24].

4. Conclusions

Partly bio-based segmented thermoplastic polyurethanes were prepared by one-shot bulk-polymeriza-

tion of industrial raw materials: an aliphatic diisocyanate (1,6-hexamethylene diisocyanate), a polyether polyol as macrodiol (polyethylene glycol) and a corn-derived chain extender (bio-based 1,3-propanediol), in presence of a catalyst. Equivalent thermoplastic polyurethanes formulations with classical petroleum-based 1,3-propanediol were also prepared for sake of comparison. The hard segment content was varied by modifying the macrodiol/chain extender ratio, and the effects on physical, mechanical and morphological properties of samples were investigated.

All the thermoplastic polyurethanes were linear multiblock copolymers, showing a microphase separation. An increase in the hard segment content from 35 to 78 wt%, induced a better phase separation and an increase in the crystallinity of hard domains. Both soft- and hard-segments are semi-crystalline, but the crystallites formed by the polyethylene glycol soft segments in the developed thermoplastic polyurethanes are less stable and less organized than those from native polyethylene glycol. However, the glass-transition temperature of the soft domains increased with increasing the hard segment content, most probably due to the restricted mobility of the amorphous chains in the vicinity of polyethylene glycol crystallites. From mechanical viewpoint, an increase in hard segment content, i.e. an improvement in hard domain ordering, was reflected by an increase in the tensile modulus, while sacrificing elongation.

Finally, the developed polyurethane formulations using bio-based chain extender fulfilled the requirements for reactive rotational molding, namely: (i) synthesis of thermoplastic polyurethanes from industrially available raw materials, by one-shot bulk-polymerization in air; (ii) reaction occurring at 45°C, enabling reduced mold heating and cooling

Table 5. Tensile properties of TPU and bio-TPU samples

Sample	HS content [wt%]	Elongation at break [%]	Ultimate tensile strength [MPa]	Tensile modulus [MPa]
TPU 912	35	167±6	13.5±0.5	55.0±2.5
TPU 822	51	158±11	16.0±0.6	76.3±3.4
TPU 732	62	139±8	18.6±0.6	99.5±5.2
TPU 552	78	119±7	21.0±0.8	122.5±5.8
HDI-PDO	100	108±6	21.9±0.9	138.8±7.1
Bio-TPU 912	35	170±8	13.6±0.3	54.5±2.1
Bio-TPU 822	51	159±10	15.5±0.2	76.3±3.4
Bio-TPU 732	62	142±9	18.7±0.4	98.2±4.6
Bio-TPU 552	78	119±8	20.2±0.6	122.5±5.8
HDI-bio PDO	100	109±5	22.8±0.7	138.8±7.1

times, (iii) relative short product manufacturing time (~20 minutes). Also, it was pointed out that replacing the petroleum-based diol by its commercial bio-based equivalent was successful for preparing thermoplastic polyurethanes, without sacrificing any properties.

Acknowledgements

The authors are grateful to CISIT (International Campus on Safety and Intermodality in Transportation), the Nord-Pas-de-Calais Region for their financial support. We wish to express our gratitude for our former colleagues Dr. A. Bessadok, and Mr. D. Hautecoeur for the help rendered by them during the preparation of the samples.

References

- [1] Lee S.: Thermoplastic polyurethane markets in the EU: Production, technology, application and trends. Rapra, Shawberry (1998).
- [2] Szycher M.: Szycher's handbook of polyurethanes. CRC Press, Boca Raton (1999).
- [3] Ionescu M.: Chemistry and technology of polyols for polyurethanes. Rapra, Shawberry (2005).
- [4] Meier M. A. R., Metzger J. O., Schubert U. S.: Plant oil renewable resources as green alternatives in polymer science. *Chemical Society Reviews*, **36**, 1788–1802 (2007).
DOI: [10.1039/b703294c](https://doi.org/10.1039/b703294c)
- [5] Rashmi B. J., Rusu D., Prashantha K., Lacrampe M. F., Krawczak P.: Development of water-blown bio-based thermoplastic polyurethane foams using bio-derived chain extender. *Journal of Applied Polymer Science*, **128**, 292–303 (2013).
DOI: [10.1002/app.38183](https://doi.org/10.1002/app.38183)
- [6] Cateto C. A., Barreiro M. F., Rodrigues A. E.: Monitoring of lignin-based polyurethane synthesis by FTIR-ATR. *Industrial Crops and Products*, **27**, 168–174 (2008).
DOI: [10.1016/j.indcrop.2007.07.018](https://doi.org/10.1016/j.indcrop.2007.07.018)
- [7] Prashantha K., Vasanth Kumar Pai K., Sherigara B. S., Prasannakumar S.: Interpenetrating polymer networks based on polyol modified castor oil polyurethane and poly(2-hydroxyethylmethacrylate): Synthesis, chemical, mechanical and thermal properties. *Bulletin of Materials Science*, **24**, 535–538 (2001).
DOI: [10.1007/BF02706727](https://doi.org/10.1007/BF02706727)
- [8] Raquez J-M., Deléglise M., Lacrampe M-F., Krawczak P.: Thermosetting (bio)materials derived from renewable resources: A critical review. *Progress in Polymer Science*, **35**, 487–509 (2010).
DOI: [10.1016/j.progpolymsci.2010.01.001](https://doi.org/10.1016/j.progpolymsci.2010.01.001)
- [9] Rusu D., Boyer S. A. E., Lacrampe M. F., Krawczak P.: Bioplastics and vegetal fiber reinforced bioplastics for automotive applications. in 'Handbook of bioplastics and biocomposites engineering applications' (Ed.: Pilla S.) Wiley-Scrivener, Hoboken, 397–448 (2011).
DOI: [10.1002/9781118203699.ch15](https://doi.org/10.1002/9781118203699.ch15)
- [10] Warwel S., Brüse F., Demes C., Kunz M., gen Klaas M. R.: Polymers and surfactants on the basis of renewable resources. *Chemosphere*, **43**, 39–48 (2001).
DOI: [10.1016/S0045-6535\(00\)00322-2](https://doi.org/10.1016/S0045-6535(00)00322-2)
- [11] Hood M. A., Wang B., Sands J. M., La Scala J. J., Beyer F. L., Li C-Y.: Morphology control of segmented polyurethanes by crystallization of hard and soft segments. *Polymer*, **51**, 2191–2198 (2010).
DOI: [10.1016/j.polymer.2010.03.027](https://doi.org/10.1016/j.polymer.2010.03.027)
- [12] Mortley A., Bonin H. W., Bui V. T.: Synthesis and properties of radiation modified thermally cured castor oil based polyurethanes. *Nuclear Instruments and Methods in Physics Research Section B: Beam Interactions with Materials and Atoms*, **265**, 98–103 (2007).
DOI: [10.1016/j.nimb.2007.08.032](https://doi.org/10.1016/j.nimb.2007.08.032)
- [13] Xu Y., Petrovic Z., Das S., Wilkes G. L.: Morphology and properties of thermoplastic polyurethanes with dangling chains in ricinoleate-based soft segments. *Polymer*, **49**, 4248–4258 (2008).
DOI: [10.1016/j.polymer.2008.07.027](https://doi.org/10.1016/j.polymer.2008.07.027)
- [14] Ajithkumar S., Kansara S. S., Patel N. K.: Kinetics of castor oil based polyol–toluene diisocyanate reactions. *European Polymer Journal*, **34**, 1273–1276 (1998).
DOI: [10.1016/S0014-3057\(97\)00270-X](https://doi.org/10.1016/S0014-3057(97)00270-X)
- [15] de Lima V., da Silva P. N., Dullius J., Ligabue R., Einloft S.: Kinetic study of polyurethane synthesis using different catalytic systems of Fe, Cu, Sn, and Cr. *Journal of Applied Polymer Science*, **115**, 1797–1802 (2010).
DOI: [10.1002/app.31298](https://doi.org/10.1002/app.31298)
- [16] Volkova E. R., Tereshatov V. V., Karmanov V. I.: Kinetics of reactions occurring during polyurethane synthesis. *Journal of Applied Spectroscopy*, **77**, 737–740 (2010).
DOI: [10.1007/s10812-010-9396-3](https://doi.org/10.1007/s10812-010-9396-3)
- [17] Madra H., Tantekin-Ersolmaz S. B., Guner F. S.: Monitoring of oil-based polyurethane synthesis by FTIR-ATR. *Polymer Testing*, **28**, 773–779 (2009).
DOI: [10.1016/j.polymertesting.2009.05.013](https://doi.org/10.1016/j.polymertesting.2009.05.013)
- [18] Cateto C. A., Barreiro M. F., Rodrigues A. E., Belgacem M. N.: Kinetic study of the formation of lignin-based polyurethanes in bulk. *Reactive and Functional Polymers*, **71**, 863–869 (2011).
DOI: [10.1016/j.reactfunctpolym.2011.05.007](https://doi.org/10.1016/j.reactfunctpolym.2011.05.007)
- [19] Lipshitz S. D., Macosko C. W.: Rheological changes during a urethane network polymerization. *Polymer Engineering and Science*, **16**, 803–810 (1976).
DOI: [10.1002/pen.760161205](https://doi.org/10.1002/pen.760161205)

- [20] Broyer E., Macosko C. W., Critchfield F. E., Lawler L. F.: Curing and heat transfer in polyurethane reaction molding. *Polymer Engineering and Science*, **18**, 382–387 (1978).
DOI: [10.1002/pen.760180509](https://doi.org/10.1002/pen.760180509)
- [21] Richter E. B., Macosko C. W.: Kinetics of fast (RIM) urethane polymerization. *Polymer Engineering and Science*, **18**, 1012–1018 (1978).
DOI: [10.1002/pen.760181308](https://doi.org/10.1002/pen.760181308)
- [22] Navarchian A. H., Picchioni F., Janssen L. P. B. M.: Rheokinetics and effect of shear rate on the kinetics of linear polyurethane formation. *Polymer Engineering and Science*, **45**, 279–287 (2005).
DOI: [10.1002/pen.20280](https://doi.org/10.1002/pen.20280)
- [23] Melo B. N., Pasa V. M. D.: Composites based on eucalyptus tar pitch/castor oil polyurethane and short sisal fibers. *Journal of Applied Polymer Science*, **89**, 3797–3802 (2003).
DOI: [10.1002/app.12424](https://doi.org/10.1002/app.12424)
- [24] Korley L. T. J., Pate B. D., Thomas E. L., Hammond P. T.: Effect of the degree of soft and hard segment ordering on the morphology and mechanical behavior of semicrystalline segmented polyurethanes. *Polymer*, **47**, 3073–3082 (2006).
DOI: [10.1016/j.polymer.2006.02.093](https://doi.org/10.1016/j.polymer.2006.02.093)
- [25] Li J., Tammer M., Kremer F., Komp A., Finkelmann H.: Strain-induced reorientation and mobility in nematic liquid-crystalline elastomers as studied by time-resolved FTIR spectroscopy. *European Physics Journal E*, **17**, 423–428 (2005).
DOI: [10.1140/epje/i2005-10018-6](https://doi.org/10.1140/epje/i2005-10018-6)

Tensile properties of *in-situ* precipitated polydimethylsiloxane networks

Y-L. Yue^{1,4}, C. Zhang², H. Zhang¹, D-H. Zhang³, X. Chen², Y-F. Chen³, Z. Zhang^{1*}

¹National Center for Nanoscience and Technology, 100190 Beijing, China

²State Grid Smart Grid Research Institute, 102211 Beijing, China

³Institute of Process Engineering, Chinese Academy of Sciences, 100190 Beijing, China

⁴University of Chinese Academy of Sciences, 100049 Beijing, China

Received 8 May 2013; accepted in revised form 26 June 2013

Abstract. Tensile properties of polydimethylsiloxane (PDMS) networks filled with *in-situ* precipitated silica were investigated. Experimental results showed that increasing the swelling time of cured rubber sheets in tetraethoxysilane (TEOS) solution or elevating the humidity and temperature of precipitation reaction atmosphere can render to a positive reinforcing effect. Moreover the *in-situ* precipitation method can be used to further enhance the tensile properties of fumed silica filled PDMS networks. The reinforcement introduced by the *in-situ* precipitated silica gel particles can probably be attributed to the adsorption of polymer chains onto silica surface, the pinning effect of polymer chains within gel particles, and the filler-filler gel structure among gel particles.

Keywords: rubber, polymer composites, reinforcements, mechanical properties

1. Introduction

The sol-gel method is generally used to prepare polymer-matrix composites (PMCs) using pure ceramic precursors at relatively low temperatures [1–3]. In 1982, Mark and Pan [4] firstly introduced this method to *in-situ* precipitate silica within PDMS networks. The *in-situ* precipitation reaction can be roughly divided into two steps: hydrolysis of alkoxy-silicates to produce hydroxyl groups, followed by polycondensation of the hydroxyl groups and residual alkoxy groups to form a three-dimensional gel network. The reactions typically proceed with either an acid or a base as catalyst to accelerate the reaction rate [5]. Thus, the total precipitation reaction using typical TEOS can be described as:



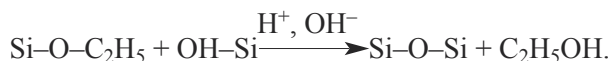
which consists of hydrolysis:



and polycondensation:



or,



The precipitation process consists of hydrolysis, polycondensation (including nucleation, growth and aggregation), gelation, aging (including polymerization, coarsening and syneresis) and drying (including evaporation and densification), which has been

*Corresponding author, e-mail: zhong.zhang@nanoctr.cn

overall reviewed by Brinker [6]. Different kinds of catalyst have dramatic effect on the precipitation process and on the final gel structure [7, 8]. Experimental results [9] have shown that acid catalyzed reactions tend to produce more chain-like polymeric entities while basic environments tend to produce more highly condensed and discrete particulate structures. Herein, we pay more attention to the acid-catalyzed precipitation process because only acid catalyst is adopted in our experiments. Acid-catalyzed hydrolysis occurs by the nucleophilic attack of the oxygen contained in water molecules on the silicon atoms and acid-catalyzed condensation involves the protonation of silanol species, which makes the silicon more electrophilic and more susceptible to nucleophilic attack [6].

Many literatures [10–15] have reported that *in-situ* precipitated networks show much improved mechanical properties compared with pure networks. Further researches [16–19] demonstrated that, compared with the agglomerated fumed silica particles incorporated by mechanical blending, *in-situ* precipitated silica gel particles are more homogeneously dispersed within the networks, thanks to the molecular-level dispersion of precursors. Also, the gel particles are generally in the nanoscale length with very narrow size distribution. Fragiadakis and coworkers [20–22] have studied the chain dynamics by various techniques. They found an interfacial structure with reduced segmental mobility between gel particles and polymer matrix. Hernandez *et al.* [23] have proven that the formation of continuous silica phase (or filler network) above the percolation concentration can also have an influence on the dynamic mechanical modulus of composites.

Although the *in-situ* precipitation method has been developed for decades, the mechanisms of reinforcement caused by the gel particles have not yet been completely clarified. The objective of the current work is to explore the reinforcing mechanisms and investigate the effect of different precipitation conditions on the tensile properties.

2. Experimental section

2.1. Materials

The α , ω -hydroxylated PDMS with average molecular weight of 80 300 g/mol and polydispersity index of 1.35 was purchased from WACKER (Germany). The fumed silica with a trademark of R106 was provided by Evonik Degussa (Germany), which

has been partially surface-modified from pristine fumed silica A300 using octamethylcyclotetrasiloxane (D₄). The tetra-functional cross-linker tetraethoxysilane (TEOS) and catalyst dibutyltin dilaurate (DBTDL) were supplied by Tian Jin Bodi Corporation (China). The toluene (A.R.) was obtained from Beijing Chemical Works (China). All materials were used as received without further treatment.

2.2. Preparation of filled networks

Fumed silica was mechanically blended with PDMS on a three-roll mill (EXAKT80E, Germany). After addition of TEOS and DBTDL, the pure PDMS and R106/PDMS suspensions were vulcanized at room temperature using solution curing method. More detailed process can be referred to our previous work [24].

The *in-situ* precipitated networks were prepared by immersing cured rubber sheets into TEOS solution containing 3 wt% of DBTDL for various time, as depicted in the work of Dewimille *et al.* [17]. The swollen sheets were laid at labs with normal conditions (temperature of 23±2°C and relative humidity of 50±20%) or within the constant temperature and humidity chamber (EYELAKCL-2000, Japan) to react for 24 h and then placed in an oven at 80°C until constant weights reached. Water molecular for hydrolysis reaction was obtained from water vapor in the atmosphere. DBTDL can generate lauric acid by hydrolysis, which acts as the catalyst for the hydrolysis and condensation reactions of TEOS. The amounts of silica *in-situ* precipitated within the networks were calculated from the sheet weights before and after precipitation. The reaction conditions and concentrations were listed in Table 1.

2.3. Tensile tests

The samples for tensile tests were stamped out from rubber sheets (with a thickness of ca. 2 mm) using a dumbbell-shaped cutter (with a 4 mm width and 20 mm initial gauge length). The tests were performed at room temperature on a tensile testing machine CMT-4104 (SANS, China) at a crosshead rate of 50 mm/min. At least five specimens were tested for each sample. The ultimate tensile strength (f_m^*) and break elongation (α_m) can be directly obtained from stress-strain (f^* - α) curves. The area under the stress-strain curve corresponds to the network breakup energy (E_b), which can be used as a measure of material toughness [25]. Meanwhile,

elastic modulus or reduced stress can be obtained from the well-known Mooney-Rivlin equation (Equation (1)):

$$[f^*] = 2C_1 + 2C_2\alpha^{-1} \quad (1)$$

where constant $2C_1$ is taken as the limit modulus of a phantom network and $2C_2$ is regarded as a measure of the extent of non-affine deformation [26, 27].

2.4. Characterization

Equilibrium swelling method was adopted to evaluate the cross-linking degree of networks. Pieces of measured weights of vulcanized rubber sheets (m_1) were immersed in toluene for 72 h at room temperature. Then the swollen sheets were wiped gently with a filter paper to remove unabsorbed solvent and their weights were measured as m_2 . The amount of absorbed toluene can be determined by the weight difference before and after swelling ($m_2 - m_1$). Herein, the equilibrium swelling ratio (q_{es}) was employed to reflect the degree of cross-linking, which is simply defined as the mass ratio of the absorbed solvent to the pure rubber (Equation (2)):

$$q_{es} = \frac{m_2 - m_1}{m_1(1 - \phi)} \quad (2)$$

where ϕ is the mass fraction of filler.

Small-angle X-ray scattering (SAXS) is widely used to provide averaged statistical information of multi-phase composites having phase structures in the nanoscale [17, 28, 29]. 2D SAXS patterns were collected within 100 s at room temperature on the beamline BL16B1 in Shanghai Synchrotron Radiation Facility (SSRF) in China. The wavelength was 0.154 nm and the sample-to-detector distance was 5110 mm. The thickness of testing specimens was about 0.5 mm. One dimensional scattering intensity curves ($I(q)$ vs. q) were obtained by radial average method using FIT2D program [30]. The data were calibrated by pure rubber sheet and normalized with respect to the incoming beam intensity.

The fractured cross-sectional surface of filled networks was examined by an atomic force microscope (AFM, Multimode 8, Bruker, Germany) in the tapping mode at the frequency of 1 Hz.

3. Results and discussion

3.1. Effect of swelling time on tensile properties

As shown in Figure 1, the swelling rate of pure rubber sheet in TEOS solution decreases with time according to a power law. The swelling ratio, defined as the mass ratio of the solution to the pure rubber, increases sharply at the initial stage and slows down gradually until an equilibrium swelling state reached. Thus, networks filled with various loadings of precipitated silica can be obtained by changing the swelling time.

Tensile properties of networks filled with various concentrations of silica gel particles precipitated at normal conditions were presented in Figure 2 and listed in Table 1. It can be seen that the modulus, tensile strength, break elongation and network breakup energy all increase with filler concentration. Compared with pure network, all filled networks exhibit non-Gaussian effect, i.e. the anomalous upturn in modulus plots. Meanwhile, the non-Gaussian effect emerges at a lower strain as concentration increases, suggesting the existence of more and shorter segments within the filled networks. Moreover, the upturn becomes suppressed at large strains for concentrations above 9.04 wt% and it nearly vanishes for the extremely high concentration of 17.26 wt%. It is beneficial to compare the *in-situ* precipitated networks with the fumed silica filled networks to explore the reinforcing mechanisms. In our previous work [24], we have discussed the tensile properties of fumed silica filled PDMS networks in detail. Therein, the reinforcement was attributed to

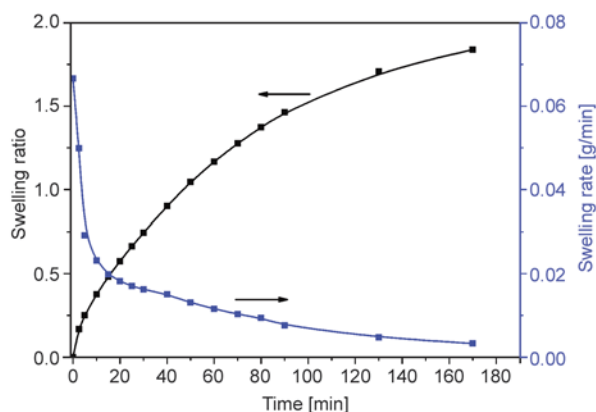


Figure 1. Swelling ratio and swelling rate of pure PDMS in TEOS solution as a function of time

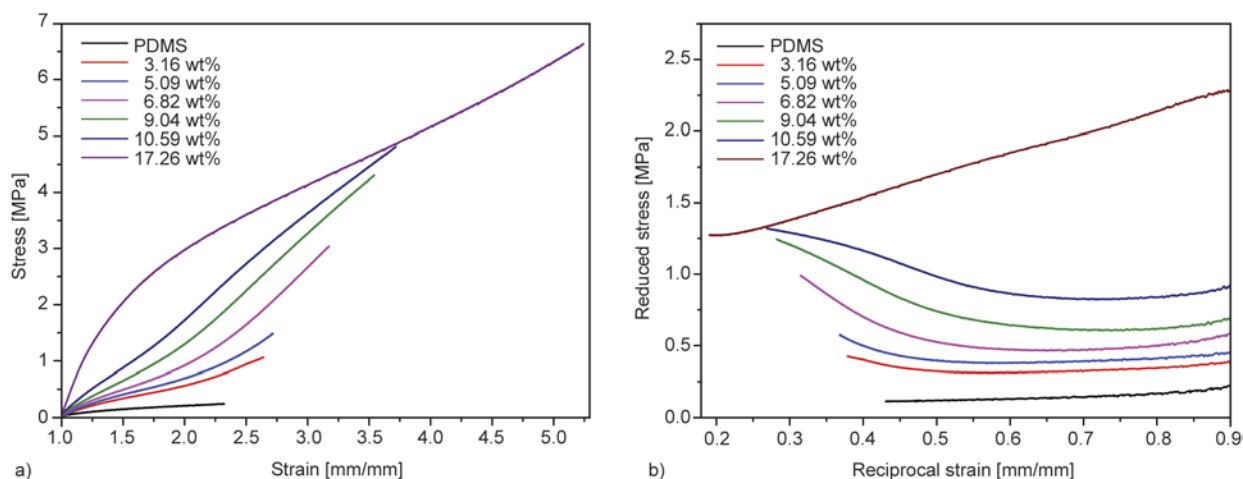


Figure 2. Stress-strain curves (a) and Mooney-Rivlin plots (b) for networks filled with various concentrations of *in-situ* precipitated silica

Table 1. Tensile testing results and equilibrium swelling ratio for unfilled and filled networks

Samples (Concentrations)	f_m^* [MPa]	α_m [%]	E_b [J/mm ³]	q_{es}
PDMS	0.25±0.02	141±9	0.21±0.02	3.35
3.16 wt%	0.97±0.12	164±10	0.83±0.03	2.29
5.09 wt%	1.47±0.11	176±12	1.12±0.05	2.24
6.82 wt%	3.05±0.08	217±4	2.68±0.01	2.18
9.04 wt%	4.31±0.08	255±2	4.97±0.01	2.11
10.59 wt%	4.93±0.10	287±13	6.62±0.05	2.05
17.26 wt%	6.41±0.45	398±15	17.40±0.08	0.95
25°C-40% (3.82 wt%)	2.20±0.12	216±9	1.82±0.03	2.21
25°C-60% (5.32 wt%)	2.76±0.13	230±13	2.72±0.05	2.23
25°C-80% (6.43 wt%)	3.43±0.12	260±8	3.70±0.04	2.24
20°C-60% (4.33 wt%)	2.01±0.11	207±14	1.74±0.05	2.30
30°C-60% (6.03 wt%)	3.40±0.22	252±15	4.10±0.06	1.87

both the effective volume effect originated from filler volume and polymer-filler interaction and the synergistic effect between network chains of different length scales within the ‘hierarchical network’. The ‘hierarchical network’ sets a stage for the shorter network chains or segments to exhibit non-Gaussian behavior at lower strains and for the networks to show non-Gaussian effect, just as the case in bimodal networks [25, 31, 32]. Herein, the polymer-filler interaction within the interfacial structure includes a new interaction type of ‘pinning effect’ within gel particles, in addition to the adsorption effect caused by hydrogen bond and van der Waals forces on the gel particle surface. Specifically, a certain number of PDMS chains can be trapped and pinned up during the formation of silica gel particles, thanks to the excellent compatibility between organic and inorganic components. The pinning effect can behave, to some extent, like chemical cross-links because generally, the rupture of chemical bonds is needed to remove the pinning effect. Consequently,

the force of overcoming pinning effect is obviously much larger than the desorption force. This is part of the reason why *in-situ* precipitated networks exhibit better mechanical properties than fumed silica filled networks at the same filler concentration [10]. The pinning and adsorption divide network chains into shorter segments in a great larger number, thus increase the degree of cross-linking density. McCarthy *et al.* [33] found that no non-Gaussian effect was observed in polymethylphenylsiloxane (PMPS) networks *in-situ* precipitated with titania, which is probably due to the very weak polymer-filler interaction including no pinning and adsorption effect. On the other hand, unlike fumed silica particles tend to form agglomerates (especially at high filler loadings), *in-situ* precipitated gel particles are well dispersed within the networks. This can be inferred from SAXS plots in Figure 3, where fumed silica filled networks only show a strong shoulder at low scattering vectors while precipitated networks show a rather weak peak within the

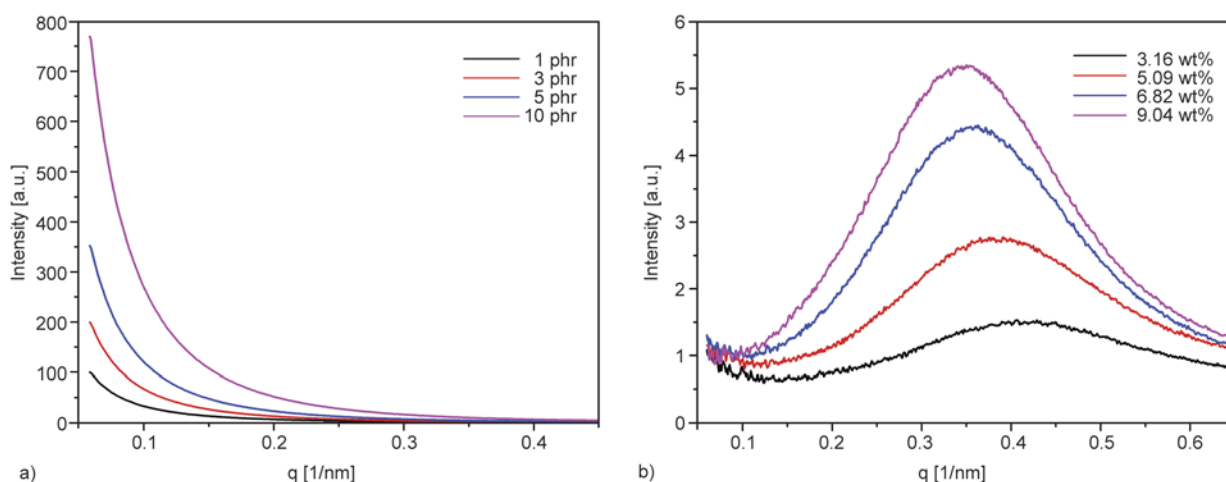


Figure 3. SAXS plots of networks filled with various concentrations of: (a) fumed silica R106, (b) *in-situ* precipitated silica

range of 0.2–0.5 1/nm. These peaks can be attributed to the relative scattering between well dispersed gel particles. Besides, the fractal dimension of scattering entities calculated from the SAXS plots using program PRIMUS [34] increases from 1.78 to 3.10, suggesting that the gel structure become more and more condensed as filler concentration increases. The increase of these scattering peaks is a combined effect of the increase in the number, size and condensed structure of gel particles. This is different from the case of fumed silica filled networks, where the increase of scattering peak is caused only by the increase of particle number. Due to the strong polymer-filler interaction and well dispersed nanoparticles, the percolation concentration of precipitated silica for the formation of ‘hierarchical network’ structure is expected to be much lower than that of fumed silica (2–3 phr for R106 filled networks [24]).

Therefore, the stress-strain behaviors of *in-situ* precipitated networks can be explained. The augmented modulus in the linear regime can still be attributed to the filler’s effective volume effect including the increase of both filler volume and cross-linking density (caused by adsorption and pinning effect). The increase of cross-linking density can be confirmed by the decrease of equilibrium swelling ratio as listed in Table 1. The upturn of modulus at large strains can be attributed to the synergistic effect between network chains of different length scales within the ‘hierarchical network’ generated by gel particles. The suppression of modulus upturn at very large strains for highly precipitated networks can be interpreted by the breakup of bridging gel structure. The bridging gel structure between

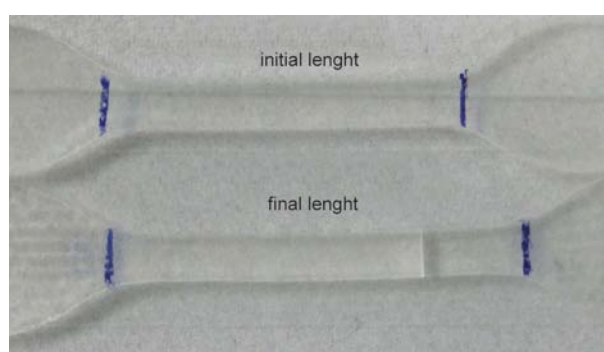


Figure 4. Photo image of the sample before and after tensile tests at the concentration of 9.04%

gel particles can be directly seen on the transmission electron microscope (TEM) graph in the work of Dewimille *et al.* [17]. This interpretation can further be adopted to explain the decrease of modulus for the network precipitated with 17.26 wt% of gel particles, where the gel filler network makes the dominant contribution to the mechanical properties. The deformation and breakup of gel structure is some sort of irreversible plastic deformation, which can be confirmed by the apparent residual strain (or, permanent set) as shown in Figure 4 and be observed from the 3D AFM height graphs in Figure 5. Only sparse valleys were seen on the fractured cross-sectional surface of fumed silica filled network, while dense peaks and dips were observed on the surface of *in-situ* precipitated network.

3.2. Effect of humidity and temperature on tensile properties

The reaction conditions have a huge influence on the dynamics of hydrolysis and polycondensation reaction and on the structure of formed silica gel particles [6, 7, 35]. Consequently, the precipitated

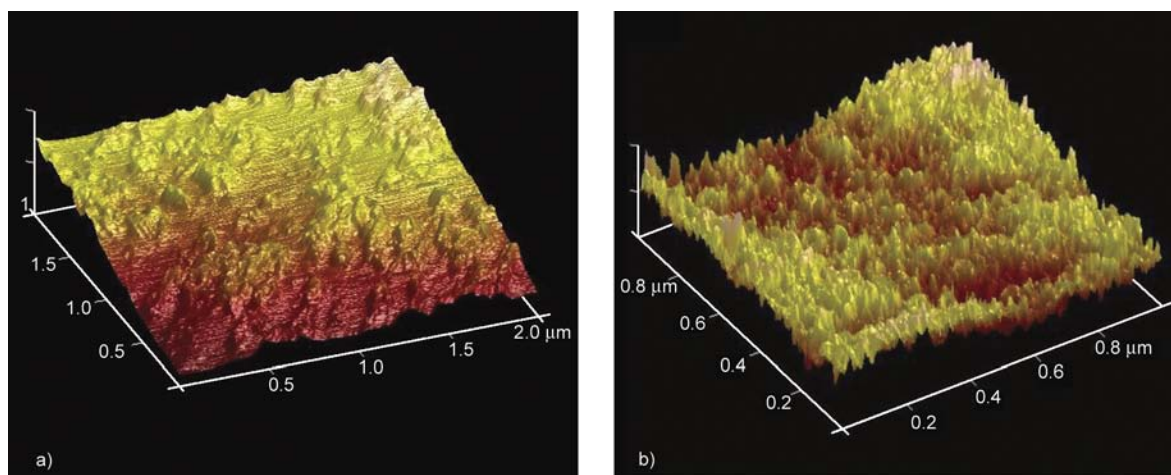


Figure 5. 3D AFM height graphs of fractured cross-sectional surface for networks filled with: (a) 10 phr of fumed silica R106, (b) 9.04% of *in-situ* precipitated silica

networks prepared under different conditions can exhibit various mechanical properties. Herein, we mainly study on the effect of humidity and temperature on the tensile properties of *in-situ* precipitated networks. Experimental results in the first column of Table 1 show that the concentration of silica gel particles within the networks (swelled in TEOS solution for 30 minutes) increases with both humidity and temperature, suggesting the higher transformation efficiency of TEOS to silica gel. Again, the structure of gel particles can be examined from SAXS plots in Figure 6. The increase of scattering peaks can again be regarded as the combined effect of the increase in the number, size and condensed structure of gel particles.

From Figure 7 and Table 1, it is seen that all mechanical parameters increase with the humidity and temperature. Meanwhile, the upturn of modulus occurs at a lower strain, suggesting the existence of more and shorter segments within the networks. The

humidity provides water molecular for the hydrolysis of both TEOS and DBTDL. Thus, the most obvious effect of increased humidity is the promotion of hydrolysis [36]. Brinker *et al.* [37] found that when hydrolysis is fast, higher density coarse textured gel particles are formed, otherwise, less low density fine textured gel particles are formed. This can be confirmed by the SAXS curves in Figure 6a. The elevated temperature has an influence on the whole precipitation process, such as accelerating the dynamics of hydrolysis and polycondensation, increasing the gelation rate, shortening the periods of aging and drying, etc. As a result, more high density coarse textured gel particles form at higher temperatures, as demonstrated by SAXS plots in Figure 6b.

To some extent, the raising of humidity and temperature generates the same reinforcing effect as the increase of swelling time. Therefore, the reinforcing mechanisms can be analyzed from the aspects

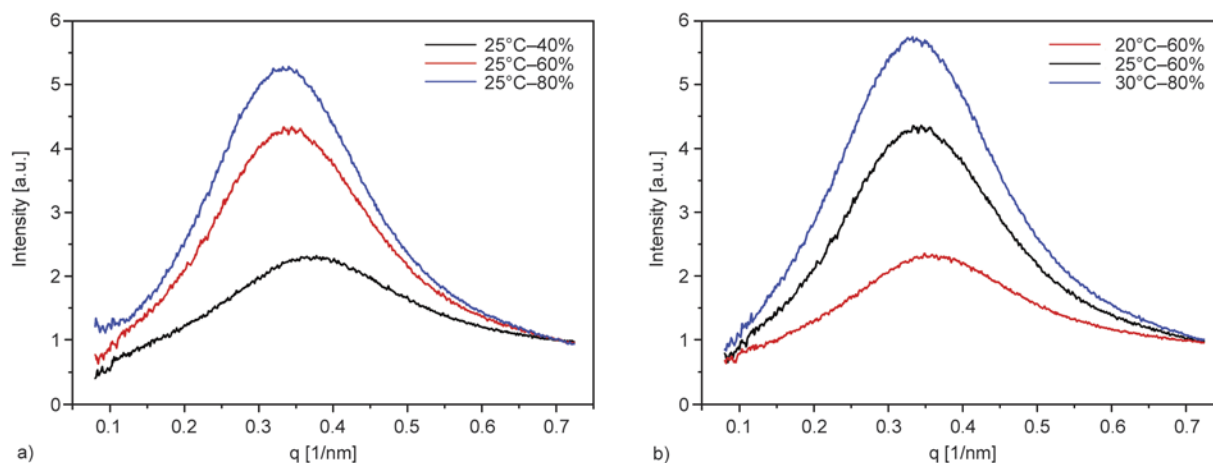


Figure 6. SAXS plots of networks filled with *in-situ* precipitated silica at variant humidities (a) and temperatures (b)

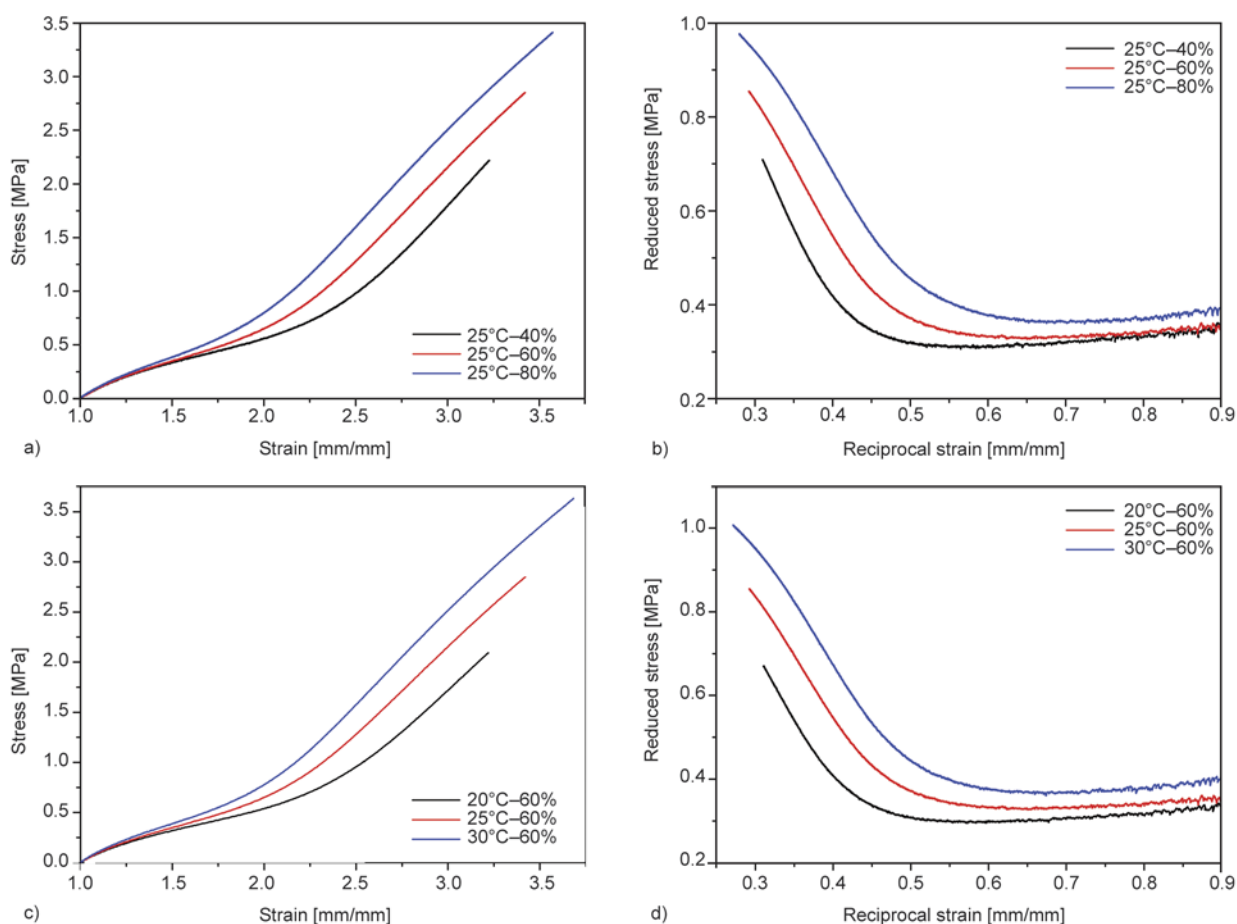


Figure 7. Stress-strain curves (a, c) and Mooney-Rivlin plots (b, d) for networks filled with silica *in-situ* precipitated at variant humidities and temperatures

of both effective volume effect and synergistic effect similar to the analysis in the above section. In short, the tensile properties of networks precipitated at higher humidity and temperature benefit from more silica gel particles with condensed structure, stronger polymer-filler interaction from pinning and adsorption effect and larger extent of synergistic effect from more and shorter segments.

3.3. Effect of second reinforcement

One advantage of *in-situ* precipitation method is that it can provide a second reinforcement on the filled networks, non-destructively. These secondly filled networks possess much better mechanical properties and have extended service life in extremely harsh applications. Moreover, this method can overcome the shortcomings of blending method involving the poor processability of high-viscosity mixtures caused by adding lots of reinforcing fillers [4]. We firstly conducted a second *in-situ* precipitation (swell for 30 min, react at 20°C and 40%) using the precipitated network labeled as ‘25°C-40%’. The

concentration of silica gel particles increases from 3.82 to 5.76 wt% after the second precipitation. The stress-strain curves and Mooney-Rivlin plots of networks after the first and second precipitation were presented in Figure 8. It can be seen that the tensile strength increases from 2.22 to 3.47 MPa, break elongation increases from 223 to 241% and network breakup energy increases from 1.82 to 3.40 J/mm³. The emergence of non-Gaussian effect of second precipitated network occurs at a lower strain, suggesting that the network chains have been further shortened due to the addition of pinning and adsorption effect. Meanwhile, the equilibrium swelling ratio decreases from 2.21 to 1.97, confirming that the cross-linking degree of filled networks further increases.

We also conducted a second *in-situ* precipitation (swell for 5 min, react at normal conditions) on the fumed silica R106 filled networks. The results of tensile tests before and after precipitation were presented in Figure 9. It can be seen that the modulus, tensile strength and network breakup energy increase

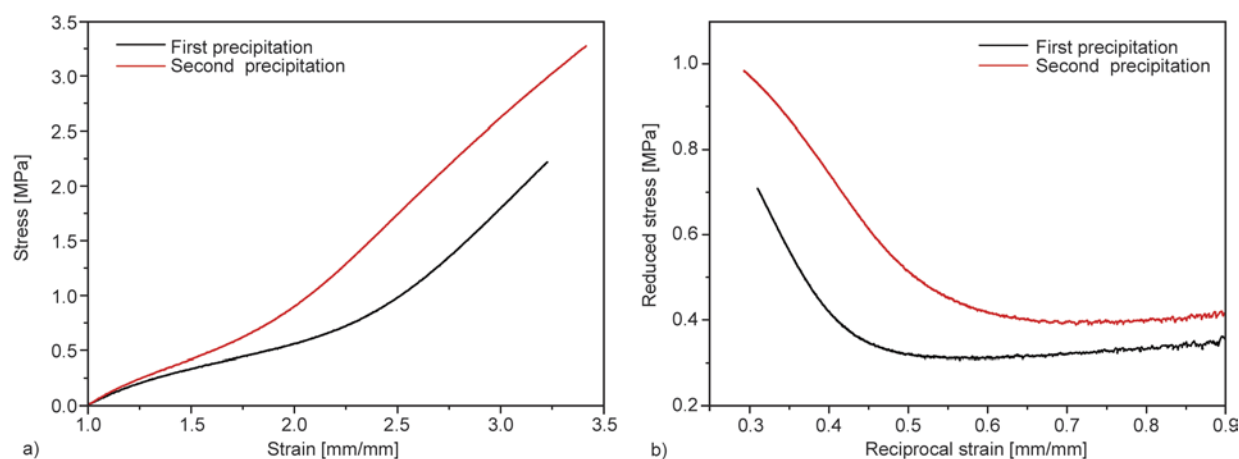


Figure 8. Stress-strain curves (a) and Mooney-Rivlin plots (b) for networks filled with first and second precipitation

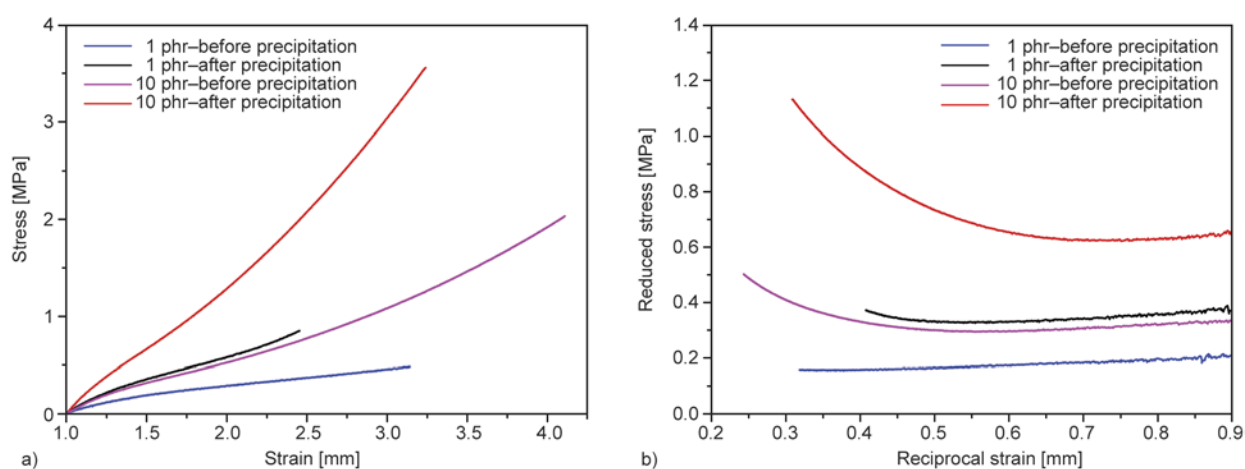


Figure 9. Stress-strain curves (a) and Mooney-Rivlin plots (b) for fumed silica filled networks before and after second precipitation

after the precipitation, while the break elongation decreases. For network filled with 1 phr of R106, Gaussian effect becomes non-Gaussian after the precipitation, suggesting the formation of the ‘hierarchical network’ structure; for network filled with 10 phr of R106, non-Gaussian effect occurs at a lower strain after the precipitation, indicating more and shorter network chains form due to the pinning and adsorption effect. The decrease of break elongation seems unexpected and elusive. This phenomenon indicates that there is some kind of incompatibility between fumed silica and silica gel particles within the networks. The two types of particles probably have different influences on the fracture properties of filled networks.

4. Conclusions

In-situ precipitation method can be used to improve the mechanical properties of pure and filled polydimethylsiloxane networks. By changing the swelling

time, humidity and temperature, various concentrations of silica gel particles with different structures can be generated within the networks. Due to the polymer-filler interaction, including the adsorption effect on the gel particle surface and the pinning effect within the gel particles, precipitated networks show much improved tensile properties. The bridging gel structures between gel particles also have a positive influence on the mechanical properties, especially at high filler concentrations. More research work is needed to clarify the fracture mechanisms of networks filled by different methods.

Acknowledgements

This project was jointly supported by a key international collaboration project (Grant No. 2011DFR50200) and the National Key Basic Research Program of China (Grant No. 2012CB937503) of the Ministry of Science and Technology of China, and the National Nature Science Foundation of China (Grant Nos. 11225210 and 51073044), and a research project of State Grid of China (Grant No. DG17201200051).

References

- [1] Wen J. Y., Wilkes G. L.: Organic/inorganic hybrid network materials by the sol-gel approach. *Chemistry of Materials*, **8**, 1667–1681 (1996).
DOI: [10.1021/cm9601143](https://doi.org/10.1021/cm9601143)
- [2] Kickelbick G.: Concepts for the incorporation of inorganic building blocks into organic polymers on a nanoscale. *Progress in Polymer Science*, **28**, 83–114 (2003).
DOI: [10.1016/S0079-6700\(02\)00019-9](https://doi.org/10.1016/S0079-6700(02)00019-9)
- [3] Mark J. E.: Some novel polymeric nanocomposites. *Accounts of Chemical Research*, **39**, 881–888 (2006).
DOI: [10.1021/ar040062k](https://doi.org/10.1021/ar040062k)
- [4] Mark J. E., Pan S.-J.: Reinforcement of polydimethylsiloxane networks by *in-situ* precipitation of silica: A new method for preparation of filled elastomers. *Die Makromolekulare Chemie, Rapid Communications*, **3**, 681–685 (1982).
DOI: [10.1002/marc.1982.030031006](https://doi.org/10.1002/marc.1982.030031006)
- [5] Artaki I., Bradley M., Zerda T. W., Jonas J.: NMR and Raman study of the hydrolysis reaction in sol-gel processes. *Journal of Physical Chemistry*, **89**, 4399–4404 (1985).
DOI: [10.1021/j100266a050](https://doi.org/10.1021/j100266a050)
- [6] Brinker C. J.: Hydrolysis and condensation of silicates: Effects on structure. *Journal of Non-Crystalline Solids*, **100**, 31–50 (1988).
DOI: [10.1016/0022-3093\(88\)90005-1](https://doi.org/10.1016/0022-3093(88)90005-1)
- [7] Osterholtz F. D., Pohl E. R.: Kinetics of the hydrolysis and condensation of organofunctional alkoxysilanes: A review. *Journal of Adhesion Science and Technology*, **6**, 127–149 (1992).
DOI: [10.1163/156856192X00106](https://doi.org/10.1163/156856192X00106)
- [8] Pope E. J. A., Mackenzie J. D.: Sol-gel processing of silica: II. The role of the catalyst. *Journal of Non-Crystalline Solids*, **87**, 185–198 (1986).
DOI: [10.1016/S0022-3093\(86\)80078-3](https://doi.org/10.1016/S0022-3093(86)80078-3)
- [9] Brinker C. J., Keefer K. D., Schaefer D. W., Assink R. A., Kay B. D., Ashley C. S.: Sol-gel transition in simple silicates II. *Journal of Non-Crystalline Solids*, **63**, 45–59 (1984).
DOI: [10.1016/0022-3093\(84\)90385-5](https://doi.org/10.1016/0022-3093(84)90385-5)
- [10] Yuan Q. W., Mark J. E.: Reinforcement of poly(dimethylsiloxane) networks by blended and *in-situ* generated silica fillers having various sizes, size distributions, and modified surfaces. *Macromolecular Chemistry and Physics*, **200**, 206–220 (1999).
DOI: [10.1002/\(SICI\)1521-3935\(19990101\)200:1<206::AID-MACP206>3.0.CO;2-S](https://doi.org/10.1002/(SICI)1521-3935(19990101)200:1<206::AID-MACP206>3.0.CO;2-S)
- [11] Kumudinie C., Mark J. E.: Tearing energies for *in-situ* reinforced poly(dimethylsiloxane) networks. *Materials Science and Engineering C*, **11**, 61–66 (2000).
DOI: [10.1016/S0928-4931\(00\)00143-0](https://doi.org/10.1016/S0928-4931(00)00143-0)
- [12] Mark J. E., Ning Y.-P.: Effects of ethylamine catalyst concentration in the precipitation of reinforcing silica filler in an elastomeric network. *Polymer Bulletin*, **12**, 413–417 (1984).
DOI: [10.1007/BF00255427](https://doi.org/10.1007/BF00255427)
- [13] McCarthy D. W., Mark J. E., Schaefer D. W.: Synthesis, structure, and properties of hybrid organic–inorganic composites based on polysiloxanes. I. Poly(dimethylsiloxane) elastomers containing silica. *Journal of Polymer Science Part B: Polymer Physics*, **36**, 1167–1189 (1998).
DOI: [10.1002/\(SICI\)1099-0488\(199805\)36:7<1167::AID-POLB7>3.0.CO;2-R](https://doi.org/10.1002/(SICI)1099-0488(199805)36:7<1167::AID-POLB7>3.0.CO;2-R)
- [14] Rajan G. S., Sur G. S., Mark J. E., Schaefer D. W., Beaucage G.: Preparation and characterization of some unusually transparent poly(dimethylsiloxane) nanocomposites. *Journal of Polymer Science Part B: Polymer Physics*, **41**, 1897–1901 (2003).
DOI: [10.1002/polb.10565](https://doi.org/10.1002/polb.10565)
- [15] Bokobza L., Diop A.: Reinforcement of poly(dimethylsiloxane) by sol-gel *in situ* generated silica and titania particles. *Express Polymer Letters*, **4**, 355–363 (2010).
DOI: [10.3144/expresspolymlett.2010.45](https://doi.org/10.3144/expresspolymlett.2010.45)
- [16] Mark J. E., Ning Y.-P., Jiang C.-Y., Tang M. Y., Roth W. C.: Electron microscopy of elastomers containing *in-situ* precipitated silica. *Polymer*, **26**, 2069–2072 (1985).
DOI: [10.1016/0032-3861\(85\)90189-2](https://doi.org/10.1016/0032-3861(85)90189-2)
- [17] Dewimille L., Bresson B., Bokobza L.: Synthesis, structure and morphology of poly(dimethylsiloxane) networks filled with *in situ* generated silica particles. *Polymer*, **46**, 4135–4143 (2005).
DOI: [10.1016/j.polymer.2005.02.049](https://doi.org/10.1016/j.polymer.2005.02.049)
- [18] Ning Y. P., Tang M. Y., Jiang C. Y., Mark J. E., Roth W. C.: Particle sizes of reinforcing silica precipitated into elastomeric networks. *Journal of Applied Polymer Science*, **29**, 3209–3212 (1984).
DOI: [10.1002/app.1984.070291022](https://doi.org/10.1002/app.1984.070291022)
- [19] Bale H. D., Schmidt P. W.: Small-angle X-ray-scattering investigation of submicroscopic porosity with fractal properties. *Physical Review Letters*, **53**, 596–599 (1984).
DOI: [10.1103/PhysRevLett.53.596](https://doi.org/10.1103/PhysRevLett.53.596)
- [20] Fragiadakis D., Pissis P., Bokobza L.: Glass transition and molecular dynamics in poly(dimethylsiloxane)/silica nanocomposites. *Polymer*, **46**, 6001–6008 (2005).
DOI: [10.1016/j.polymer.2005.05.080](https://doi.org/10.1016/j.polymer.2005.05.080)
- [21] Fragiadakis D., Pissis P., Bokobza L.: Modified chain dynamics in poly(dimethylsiloxane)/silica nanocomposites. *Journal of Non-Crystalline Solids*, **352**, 4969–4972 (2006).
DOI: [10.1016/j.jnoncrysol.2006.02.159](https://doi.org/10.1016/j.jnoncrysol.2006.02.159)
- [22] Fragiadakis D., Pissis P.: Glass transition and segmental dynamics in poly(dimethylsiloxane)/silica nanocomposites studied by various techniques. *Journal of Non-Crystalline Solids*, **353**, 4344–4352 (2007).
DOI: [10.1016/j.jnoncrysol.2007.05.183](https://doi.org/10.1016/j.jnoncrysol.2007.05.183)
- [23] Hernández J. C. R., Pradas M. M., Ribelles J.: Properties of poly(2-hydroxyethyl acrylate)-silica nanocomposites obtained by the sol-gel process. *Journal of Non-Crystalline Solids*, **354**, 1900–1908 (2008).
DOI: [10.1016/j.jnoncrysol.2007.10.016](https://doi.org/10.1016/j.jnoncrysol.2007.10.016)

- [24] Yue Y. L., Zhang H., Zhang Z., Chen Y. F.: Tensile properties of fumed silica filled polydimethylsiloxane networks. *Composites Part A: Applied Science and Manufacturing*, in press (2013). DOI: [10.1016/j.compositesa.2013.06.016](https://doi.org/10.1016/j.compositesa.2013.06.016)
- [25] Llorente M. A., Andradý A. L., Mark J. E.: Model networks of end-linked polydimethylsiloxane chains. XI. Use of very short network chains to improve ultimate properties. *Journal of Polymer Science: Polymer Physics Edition*, **19**, 621–630 (1981). DOI: [10.1002/pol.1981.180190406](https://doi.org/10.1002/pol.1981.180190406)
- [26] Mark J. E., Sullivan J. L.: Model networks of end-linked polydimethylsiloxane chains. I. Comparisons between experimental and theoretical values of the elastic modulus and the equilibrium degree of swelling. *Journal of Chemical Physics*, **66**, 1006–1011 (1977). DOI: [10.1063/1.434056](https://doi.org/10.1063/1.434056)
- [27] Mark J. E.: The constants $2C_1$ and $2C_2$ in phenomenological elasticity theory and their dependence on experimental variables. *Rubber Chemistry and Technology*, **48**, 495–512 (1975). DOI: [10.5254/1.3547463](https://doi.org/10.5254/1.3547463)
- [28] Craievich A. F.: Synchrotron SAXS studies of nanostructured materials and colloidal solutions. A review. *Materials Research*, **5**, 1–11 (2002). DOI: [10.1590/S1516-14392002000100002](https://doi.org/10.1590/S1516-14392002000100002)
- [29] Young R. J., Al-Khudhairy D. H. A., Thomas A. G.: Characterization of filled rubbers using small-angle X-ray scattering. *Journal of Materials Science*, **21**, 1211–1218 (1986). DOI: [10.1007/BF00553253](https://doi.org/10.1007/BF00553253)
- [30] Hammersley A., Svensson S., Hanfland M., Fitch A., Hausermann D.: Two-dimensional detector software: From real detector to idealised image or two-theta scan. *International Journal of High Pressure Research*, **14**, 235–248 (1996). DOI: [10.1080/08957959608201408](https://doi.org/10.1080/08957959608201408)
- [31] Andradý A. L., Llorente M. A., Mark J. E.: Model networks of end-linked polydimethylsiloxane chains. VII. Networks designed to demonstrate non-Gaussian effects related to limited chain extensibility. *Journal of Chemical Physics*, **72**, 2282–2290 (1980). DOI: [10.1063/1.439472](https://doi.org/10.1063/1.439472)
- [32] Smith T. L., Haidar B., Hedrick J. L.: Origin of the self-reinforcement in PDMS bimodal networks. *Rubber Chemistry and Technology*, **63**, 256–264 (1990). DOI: [10.5254/1.3538256](https://doi.org/10.5254/1.3538256)
- [33] McCarthy D. W., Mark J. E., Clarson S. J., Schaefer D. W.: Synthesis, structure, and properties of hybrid organic-inorganic composites based on polysiloxanes. II. Comparisons between poly(methylphenylsiloxane) and poly(dimethylsiloxane), and between titania and silica. *Journal of Polymer Science Part B: Polymer Physics*, **36**, 1191–1200 (1998). DOI: [10.1002/\(SICI\)1099-0488\(199805\)36:7<1191::AID-POLB8>3.0.CO;2-X](https://doi.org/10.1002/(SICI)1099-0488(199805)36:7<1191::AID-POLB8>3.0.CO;2-X)
- [34] Konarev P. V., Volkov V. V., Sokolova A. V., Koch M. H. J., Svergun D. I.: PRIMUS: a Windows PC-based system for small-angle scattering data analysis. *Journal of Applied Crystallography*, **36**, 1277–1282 (2003). DOI: [10.1107/S0021889803012779](https://doi.org/10.1107/S0021889803012779)
- [35] Chen K. C., Tsuchiya T., Mackenzie J. D.: Sol-gel processing of silica. I. The role of the starting compounds. *Journal of Non-Crystalline Solids*, **81**, 227–237 (1986). DOI: [10.1016/0022-3093\(86\)90272-3](https://doi.org/10.1016/0022-3093(86)90272-3)
- [36] Pouxviel J. C., Boilot J. P., Beloeil J. C., Lallemand J. Y.: NMR study of the sol/gel polymerization. *Journal of Non-Crystalline Solids*, **89**, 345–360 (1987). DOI: [10.1016/S0022-3093\(87\)80277-6](https://doi.org/10.1016/S0022-3093(87)80277-6)
- [37] Brinker C. J., Keefer K. D., Schaefer D. W., Ashley C. S.: Sol-gel transition in simple silicates. *Journal of Non-Crystalline Solids*, **48**, 47–64 (1982). DOI: [10.1016/0022-3093\(82\)90245-9](https://doi.org/10.1016/0022-3093(82)90245-9)

Processing – morphology – property relationships of polyamide 6/polyethylene blend–clay nanocomposites

R. Scaffaro*, L. Botta, M. C. Mistretta, F. P. La Mantia

Dipartimento di Ingegneria Civile, Ambientale, Aerospaziale, dei Materiali, Università di Palermo, Viale delle Scienze, Ed. 6, 90128 Palermo, Italy

Received 4 April 2013; accepted in revised form 4 July 2013

Abstract. In this work, we studied the effect of the method of preparation and of reprocessing on the morphology and, consequently, on the physical properties of polyamide 6 (PA6)/ high density polyethylene (HDPE)-clay nanocomposite blends in the presence of different compatibilizers. In particular, the nanocomposites were obtained by melt mixing using a co-rotating twin screw extruder (E1). The blends thus obtained were re-extruded (E2) under the same operating conditions. Moreover, blends with the same final composition were produced using a masterbatch of the compatibilizer with the clay prepared in a separated stage in a batch mixer (MB). All the materials were characterized by scanning electron microscopy (SEM), transmission electron microscopy (TEM) and X-ray diffractometry (XRD) analyses. In addition, the rheological behaviour and the, tensile and impact, properties were evaluated. The XRD and TEM analysis showed that re-extrusion slightly improves the morphology of the nanocomposites. A further improvement of the morphology, in terms of lower clay dimension and better dispersion, was observed in the MB blends. The results of the mechanical tests showed that reprocessing (E2) induced an increase of all the properties for all the three systems. A further general increase of the mechanical properties was showed by the MB blends.

Keywords: nanocomposites, organoclay, compatibilization, polymer blends

1. Introduction

There are several studies on the preparation and the properties of nanocomposites based on polymer blends in the presence or not of compatibilizers [1–9].

Blends of polyamides with polyolefins and polyesters are particularly interesting and attractive from an industrial point of view. During the last years, it has been shown that such blends can be efficiently compatibilized with numerous compounds derived from maleic anhydride, acrylic acid, glycidyl methacrylate, oxazoline, etc., grafted onto the polyolefin chain so that hydrogen bonds, or even covalent bonds, can be formed between the two polymers at the blending stage [10–18].

Nanocomposites based on polyethylene (PE) and polyamide (PA) blends have also been studied. In particular, the effect of the composition and of filler level was investigated [19–24]. In our previous works we presented the properties of high density polyethylene (HDPE) and polyamide 6 (PA6) blends containing an organically modified montmorillonite (OMM) [25, 26]. We evaluated the effect of different compatibilizing systems on the properties of the blends. The results indicated that, despite a good morphology achieved in the filled blends and a moderate intercalation level, the mechanical performance, especially the properties at break, were not satisfactory. This behaviour was attributed to degradation phenomena involving the organic modifier of the clay that were reduced by using a stabi-

*Corresponding author, e-mail: roberto.scaffaro@unipa.it
© BME-PT

lizing system. These degradation phenomena were deeply investigated in other works [27, 28]. We studied the effect of thermal treatments under different atmospheres and for different times on the behaviour of organically modified clays, demonstrating that the degradation products of the modifier (α -olefins transforming into various carboxyl compounds if oxygen is present) initially increased the basal spacing, followed by a collapse of the particle layers when the decomposition products migrated toward the surface and eventually volatilized. Moreover, in order to understand the possible different interactions of neat and degraded modified clay, composites were prepared in the melt and fully characterized.

There are several works regarding the effect of reprocessing on the morphology and on the properties of polymer based nanocomposites, but to the best of our knowledge no similar studies was performed on nanocomposite based on polymer blends [29–34].

Aim of this work is to evaluate the influence of morphology, at nano and micro scale, achieved by different processing methods on the rheological and mechanical properties of blends of PA6/HDPE in the presence of OMM and different compatibilizing systems. The morphology of the blends was studied by XRD, TEM and SEM analyses.

2. Experimental section

2.1. Materials and pre-treatments

The PA6 used in this work was a sample of Radilon S35 100 NAT, kindly supplied by Radicinova, Italy. It has an intrinsic viscosity (measured in sulfuric acid) equal to 3.4 dL/g. The HDPE was an injection moulding grade (MP94, Polimeri Europa, Italy, Melt Flow Index at 190°C/2,16 kg = 7 g/10 min).

Three compatibilizing systems were used in this work: an ethylene-co-acrylic acid copolymer (EAA) (Escor 5001, Exxon chemical, acrylic acid content 6.2 wt%) together with a 2,2'-(1,3-phenylene)-bis(2-oxazoline) (PBO) (1,3-PBO, Adeka Palmarole, melting point 146°C); a high-density polyethylene modified with acrylic acid (HDAA) (Polybond 1009, Chemtura, acrylic acid content 6 wt%) together

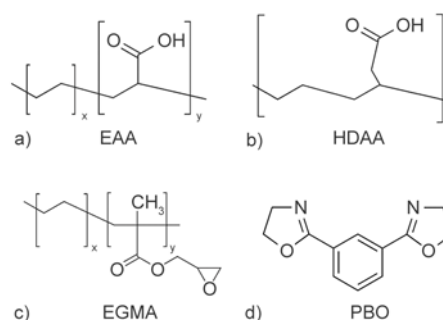


Figure 1. Chemical structure of each compatibilizer used in this work: a) EAA; b) HDAA, c) EGMA, d) PBO

with PBO and an ethylene-co-glycidyl methacrylate copolymer (EGMA) (Lotader AX8840, Arkema, glycidyl methacrylate content 8 wt%). The chemical structure of each compatibilizer is reported in the Figure 1.

Nanocomposites were prepared by adding 5 phr of montmorillonite modified with alkylammonium salts (Cloisite 15A, Southern Clay). The organic modifier is a dimethyl-ditallow, with two organophilic tails fully hydrogenated with an average composition of 65% C₁₈, 30% C₁₆ and 5% C₁₄. Prior to processing, all the materials, except PBO and HDPE used as-received, were dried in order to prevent hydrolytic scission of the polyamide. PA6 was dried for 10 h in a ventilated oven at 90°C followed by 16 h under vacuum at 120°C, while EAA, HDAA and EGMA were dried for 3 h under vacuum at 70°C and the Cloisite was dried 12 h under vacuum at 120°C.

2.2. Processing

Blends PA6/HDPE 25/75 w/w were produced by using a co-rotating modular twin screw extruder (OMC, Italy). All the blends prepared together with sample code and composition are reported in Table 1. The materials were prepared using different procedures as reported in Table 2. Some blends were prepared by premixing all the components in the solid state and then feeding them all together into the extruder (E1). The thermal profile was 180–200–210–220–230–240–240°C and the screw speed 220 rpm. Under these conditions, the residence time, measured by feeding a colour tracer to the extruder

Table 1. Sample code and composition of the blends prepared in the present work

Code sample	PA6	HDPE	EAA	HDAA	EGMA	PBO	CL15A
PA6/HDPE/EAA/PBO/15A	25	75	5	–	–	0.2	5
PA6/HDPE/HDAA/PBO/15A	25	75	–	5	–	0.2	5
PA6/HDPE/EGMA/15A	25	75	–	–	5	–	5

Table 2. Sample code of different preparation method

Code sample	Processing
PA6/HDPE/EAA/PBO/15A/E1	Extrusion
PA6/HDPE/HDAA/PBO/15A/E1	Extrusion
PA6/HDPE/EGMA/15A/E1	Extrusion
PA6/HDPE/EAA/PBO/15A/E2	Re-Extrusion
PA6/HDPE/HDAA/PBO/15A/E2	Re-Extrusion
PA6/HDPE/EGMA/15A/E2	Re-Extrusion
PA6/HDPE/EAA/PBO/15A/MB	Masterbatch
PA6/HDPE/HDAA/PBO/15A/MB	Masterbatch
PA6/HDPE/EGMA/15A/MB	Masterbatch

in a separated test, was about 80 s. The molten material coming out from the extruder die was immediately cooled on line in a water bath, pelletized and then used for further characterization. In another procedure, part of the pelletized blends was further re-extruded adopting the same conditions in order to evaluate the effect of the re-processing (E2). In another procedure, blends with the same final composition were prepared using a masterbatch of the compatibilizer (EAA, HDAA or EGMA) with Cloisite 15A, prepared in a separated stage at 180°C and 64 rpm in a Brabender batch mixer. In particular, the masterbatch and the other components of the blends were premixed in the solid state and fed to the extruder adopting the same conditions reported above (MB).

2.3. Characterization

The morphology of the clay and of the nanocomposites was evaluated by using X-ray diffractometry (XRD), scanning electron microscopy (SEM) and transmission electron microscopy (TEM). XRD analyses were performed using a diffractometer Siemens D-500 in reflection mode with an incident X-ray wavelength of 0.1542 nm. The morphology of the samples was analyzed by a scanning electron microscope (SEM) (Quanta 200F ESEM, FEI, USA). All samples were fractured in liquid nitrogen and sputter-coated with a thin layer of gold to avoid electrostatic charging under the electron beam. Transmission electron microscopy (TEM) images were obtained with a Philips EM 208 TEM with 100 keV accelerating voltage. Ultrathin sections (50 nm thickness) of the specimens, cooled at ; 80°C, were obtained by cryo-ultramicrotomy with a diamond knife cooled at -60°C.

Rheological measurements were carried out using a parallel plate rheometer (RD AII, Rheometrics) equipped with plates of 25 mm diameter in dynamic

mode. The testing temperature was 240°C and the frequency range 0.1–500 rad/s.

Mechanical characterization was carried out on specimens cut off from compression-moulded sheets (10 × 90 × ~0.6 mm). Mechanical testing was performed using an Instron 4443 tensile testing machine according to ASTM D882. The grip distance was 50 mm and the crosshead speed was 50 mm/min. IZOD impact test were carried out using a CEAST 6545/000 according with ASTM D256 on notched specimens.

All the specimens for the mechanical and rheological characterization were prepared by compression moulding at 240°C using a Carver Laboratory press (100 bar, 7 min) on materials dried for 3 h at 120°C in a vacuum oven.

3. Results and discussion

3.1. X-ray diffractometry (XRD)

In order to evaluate the morphology of OMM after processing, XRD diffraction has been carried out on all the samples. In Figure 2, there are reported the XRD patterns of blends compatibilized with EAA, Figure 2a, HDAA, Figure 2b and EGMA, Figure 2c, prepared by single extrusion (E1), re-extrusion (E2) and extrusion with a masterbatch (MB). As reported in our previous works, the XRD pattern of Cloisite 15A (here not reported for sake of clarity) presents a main broad peak at 2.8° (the position is indicated with dotted vertical lines included in Figure 2a–2c) corresponding to a d-spacing of 3.15 nm [26, 35–37]. In Table 3 there are reported the values of 2θ corresponding to the main diffraction peak of the XRD patterns and the respective values of interlayer distance calculated by Bragg's law.

As regards all the blends, it is worth observing that they all present peaks associated to the clay. This feature suggests that an exfoliated structure was never achieved at least under the processing and composition conditions here adopted.

In all compatibilized blends E1 the peak related to Cloisite 15A shifted towards lower angles and, as reported in Table 3, therefore the d-spacing increased. In accordance with our previous work, this is particularly true for the blend compatibilized with EAA/PBO system as the interlayer distance is above 4 nm [26]. The structure achieved by the organoclay in the compatibilized blends can be explained considering that, on increasing the compatibilizing effect, the adhesion between the different phases and the

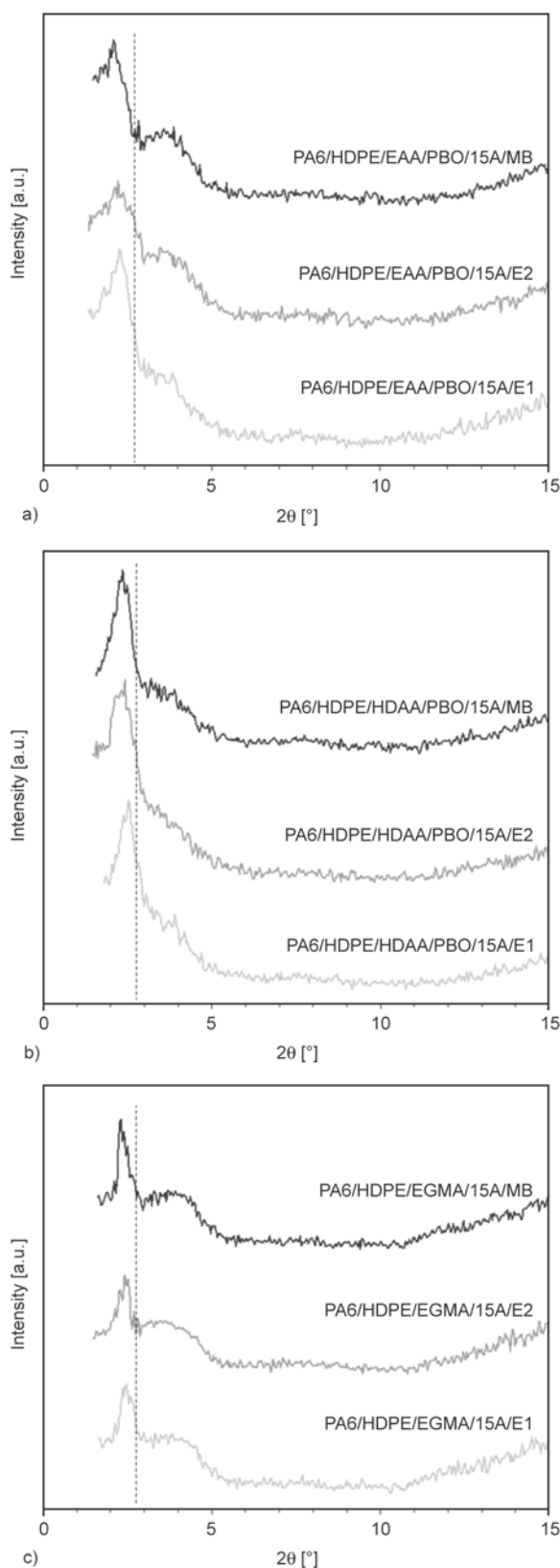


Figure 2. XRD patterns of blends compatibilized with a) EAA, b) HDAA and c) EGMA prepared by single extrusion (E1), re-extrusion (E2) and extrusion with a masterbatch (MB). The dotted vertical lines indicates the position corresponding to main peak at 2.8° of neat Cloisite 15A

Table 3. Interlayer distance of neat CL15A and of compatibilized blends prepared by single extrusion (E1), re-extrusion (E2) and extrusion with a masterbatch (MB)

Sample	2θ [°]	d-spacing [nm]
CL 15A as received	2.80	3.15
PA6/HDPE/EAA/PBO/15A/E1	2.20	4.02
PA6/HDPE/EAA/PBO/15A/E2	2.14	4.13
PA6/HDPE/EAA/PBO/15A/MB	2.07	4.27
PA6/HDPE/HDAA/PBO/15A/E1	2.48	3.56
PA6/HDPE/HDAA/PBO/15A/E2	2.38	3.72
PA6/HDPE/HDAA/PBO/15A/MB	2.31	3.83
PA6/HDPE/EGMA/15A/E1	2.40	3.68
PA6/HDPE/EGMA/15A/E2	2.39	3.70
PA6/HDPE/EGMA/15A/MB	2.25	3.93

melt stresses, are increased. As a consequence, the clay tactoids are more stressed and the polymer chains can enter the galleries thus increasing the d-spacing [26].

The XRD spectra of the re-extruded blends (E2) show that both in the system containing EAA, Figure 2a, and in that containing HDAA, Figure 2b, the peak related to Cloisite 15A shifts to lower angles. Indeed, as reported in Table 3, the interlayer distance of the clay incorporated in the polymer matrix increases after the reprocessing growing from 4.02 to 4.13 nm for the EAA compatibilized blends and from 3.56 to 3.72 nm for blends containing HDAA. Such result, according to the scientific literature, can be likely ascribed to the supplementary stresses induced on the blend by the second processing. This would allow a further dispersion/redistribution of the nanofiller with consequent higher intercalation level [32–34].

As regards the EGMA compatibilized materials, Figure 2c, the position of the peak identifying Cloisite 15A remains practically unchanged after the reprocessing and consequently the d-spacing is almost the same for both the samples, i.e. 3.68 nm for PA6/HDPE/EGMA/15A/E1 and 3.70 nm for PA6/HDPE/EGMA/15A/E2.

When a compatibilizer-clay masterbatch is used, there is always a shift of the peak of Cloisite toward angles even lower than those observed for E1 and E2 materials, thus indicating a higher interlayer distance as highlighted by the values of d-spacing reported in Table 3. Indeed, for each compatibilized system the MB blend exhibits the higher interlayer distance.

These results, in accordance with the literature, can be explained considering that the preparation of the

compatibilizer-clay masterbatch may induce a certain initial intercalation/expansion of the clay that becomes more intense during the subsequent extrusion processing [38].

Moreover, the differences observed between the different compatibilizers could depend on their different viscosity and affinity with the nanofiller. This feature, indeed, may cause higher or lower pre-intercalation of the compatibilizer during the masterbatch preparation. HDAA, in fact, having a lower viscosity if compared with the other compatibilizers as reported in our previous work, could be less

effective in dispersing the clay compared with EAA or EGMA [26]. Of course, the affinity between the clay and the compatibilizer plays also a key role in determining the final morphology in the masterbatch and a dedicated study to go deeper inside these aspects will be object of a future work.

3.2. Transmission electron microscopy (TEM)

To better understand the structure of the nanocomposites and to corroborate the conclusions achieved by XRD analysis, TEM analysis was carried out on the nanocomposites.

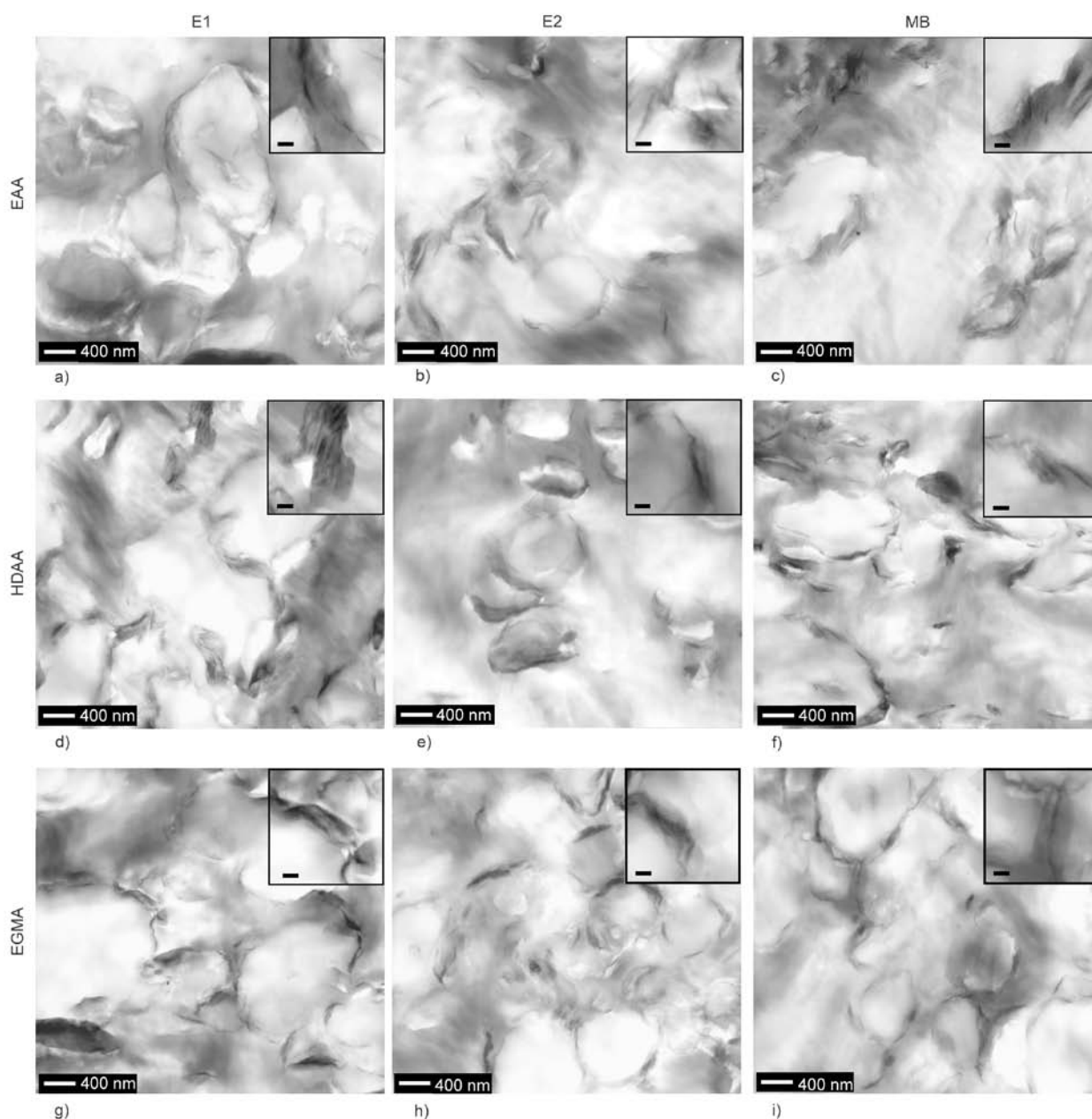


Figure 3. TEM micrographs of compatibilized blends prepared by single extrusion (E1: a, d, g), re-extrusion (E2: b, e, h) and extrusion with a masterbatch (MB: c, f, i). Each TEM image contains inside a frame with the magnification of an illustrative particular. The scale bar contained in each frame corresponds to 100 nm.

In Figure 3 the TEM micrographs of blends compatibilized with EAA, Figure 3a–3c, HDAA, Figure 3d–f, and EGMA, Figure 3g–3i prepared by single extrusion (E1), re-extrusion (E2) and extrusion with a masterbatch (MB) are reported. Each image contains inside a frame with the magnification of an illustrative part.

The TEM micrographs of blends E1 show that the clay in all the materials is mainly organized in intercalated tactoids although some isolated exfoliated silicate sheet can be found. Moreover, it is interesting to note that, despite PA6 is the minor polymeric phase, the filler is mainly located inside the PA6 phase and at HDPE/PA6 interface. This is in agreement with the observation of other authors on similar systems and can be reasonably explained considering that, despite the presence of the organic modifier, the clay is essentially a polar component that, therefore, tends to migrate to the polar part of the blend [39].

In the re-processed materials, it is possible to individuate areas in which the clay tactoids are smaller than those observed in the same non-reprocessed

blends. This is particularly true for the blends containing EAA and HDAA as compatibilizers, Figure 3b and 3e. This is in agreement with the XRD analysis and confirms that the second processing helps in dispersing the nanofiller inside the matrix achieving a better morphology.

A further improvement of the morphology, in terms of lower clay dimension and better dispersion, can be observed in the blends prepared using the compatibilizer-clay masterbatch prepared in a separated step prior extruding, Figure 3c, 3f and 3i. Also this result is fully according with the XRD analysis, confirming the positive effects of this procedure on the intercalation/exfoliation of the clay.

3.3. Scanning electron microscopy (SEM)

Differently from TEM that observes very small portions of the material, SEM analysis is a powerful characterization to investigate the overall phase morphology of the polymer blends and of the related composites. In particular, it is possible to evaluate the interfacial modification in the presence of compatibilizers, the dispersion of the phases and the

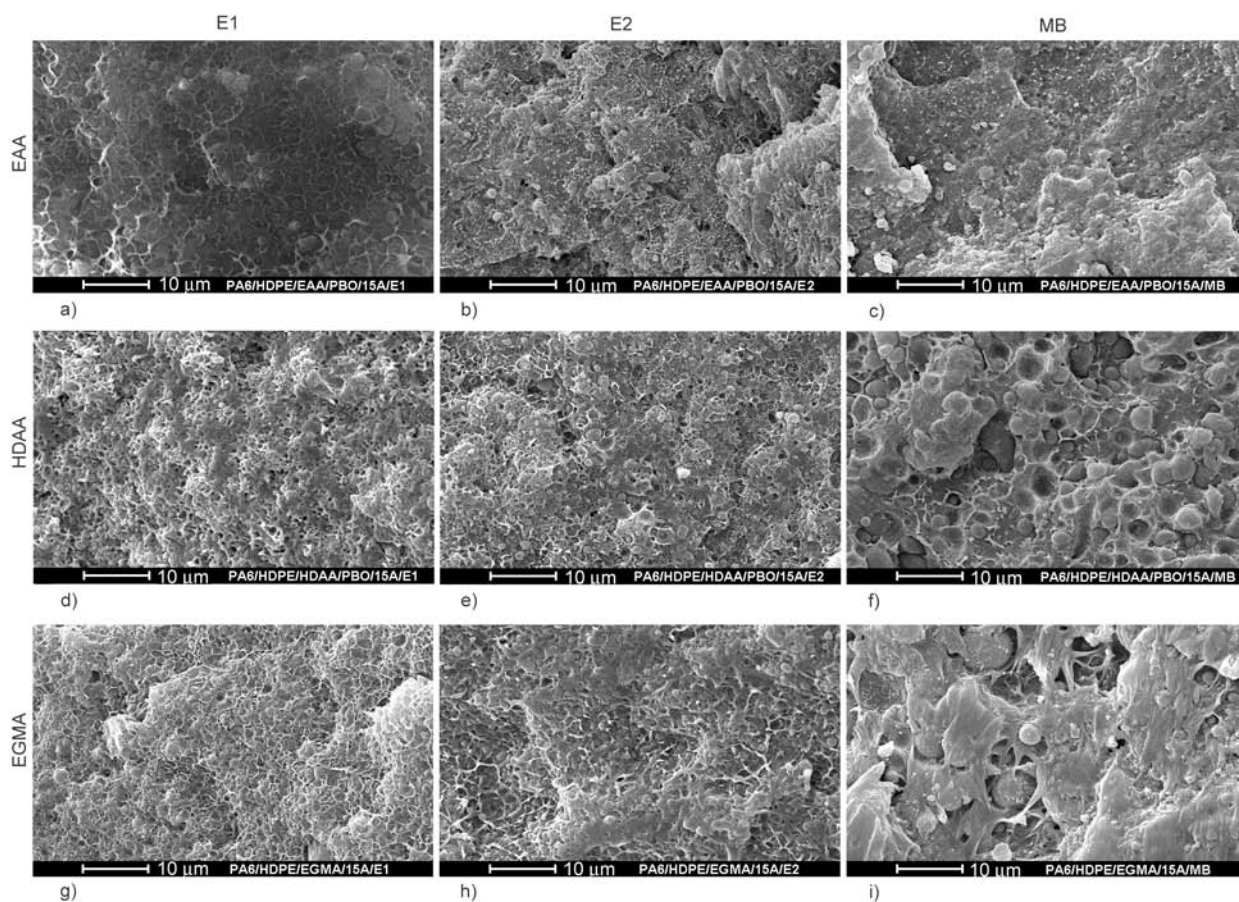


Figure 4. SEM micrographs of compatibilized blends prepared by single extrusion (E1: a, d, g), re-extrusion (E2: b, e, h) and extrusion with a masterbatch (MB: c, f, i)

reciprocal adhesion achieved by different processing methods, with particular reference to the two polymeric phases constituting the matrix.

In Figure 4 there are reported the SEM micrographs of blends compatibilized with EAA, Figure 4 a–4c, HDAA, Figure 4d–4f, and EGMA, Figure 4g–4i prepared by single extrusion (E1), re-extrusion (E2) and extrusion using a clay/compatibilizer masterbatch (MB).

It is evident that in the blends PA6/HDPE/EAA/PBO/15A/E2, Figure 4b, and PA6/HDPE/EAA/PBO/15A/MB, Figure 4c, the dimension of the particles of the PA6 dispersed phase is definitely smaller and the interfacial adhesion better than those observed in the corresponding E1 blend, Figure 4a. It is also possible to see smaller aggregates with a different contrast, ascribable to the clay tactoids, well dispersed both in E1, in E2 and in MB materials.

When using HDAA as compatibilizer, the dimension of the particles of E2, Figure 4e, and especially of MB materials, Figure 4f, is higher if compared with that of E1, Figure 4d. However, the adhesion of E2 seems to be the best. Also in this case, it is possible to find small clay aggregates, better dispersed in E2 and MB materials.

The situation is similar for the EGMA compatibilized blends. In this case, the blends E2, Figure 4h and MB, Figure 4i, display a rougher morphology if compared with E1, Figure 4g, but the adhesion of the former is definitely better, as the particles are well embedded in the matrix. It is worth noting that the dispersion of the clay aggregates is here less uniform if compared with that observed in the materials compatibilized with EAA/PBO or HDAA.

3.4. Rheological characterization

The complex viscosity, the storage modulus and the loss modulus as a function of frequency are reported in Figure 5–7 for all the materials.

As regards the blends compatibilized with the EAA/PBO system, Figure 5, the viscosity of PA6/HDPE/EAA/PBO/15A/E2 is the lowest of this series of materials while E1 and MB show almost the same values. This can be likely interpreted with degradation phenomena occurring during the second reprocessing. It must be highlighted that, from one side, reprocessing can absolutely improve the overall morphology, especially in terms of dimension. Nevertheless, it cannot be disregarded that in E2 blends,

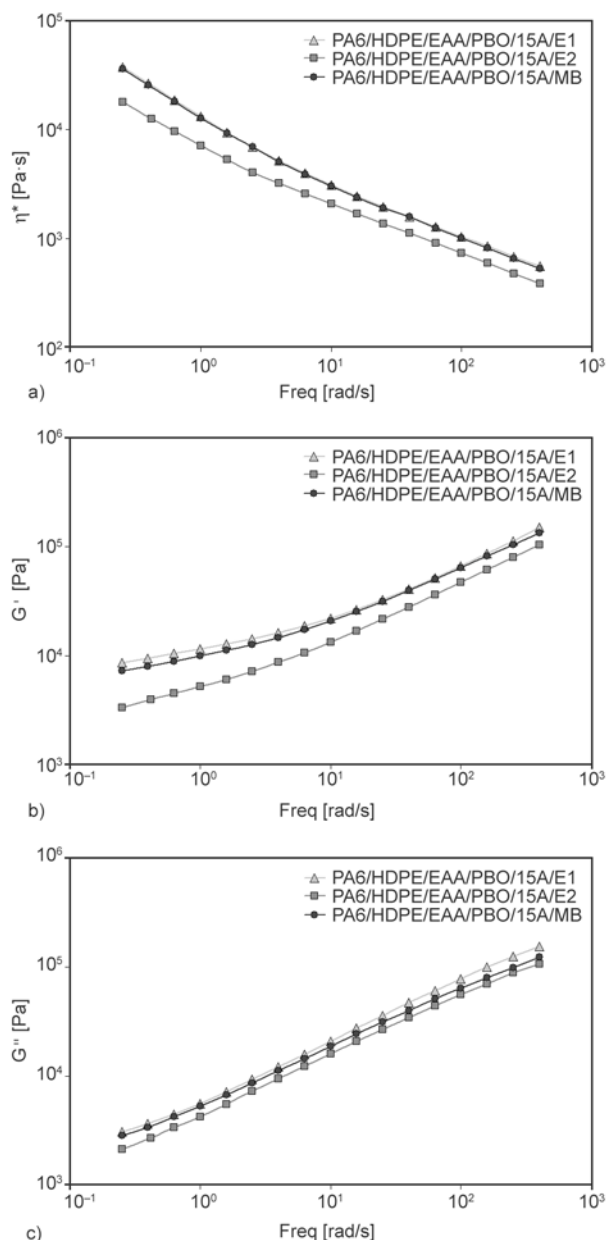


Figure 5. Complex viscosity (a), storage modulus (b) and the loss modulus (c) as a function of frequency of blend compatibilized with EAA prepared by single extrusion (E1), re-extrusion (E2) and extrusion with a masterbatch (MB)

HDPE, PA6 and the clay are exposed to high temperatures and mechanical stresses for a second time. According to our previous results, the degradation products of the clay can be responsible of a marked deactivation of the compatibilizing system [26, 27]. The decrease of the compatibilizing action given by EAA/PBO induces a lower phase adhesion and, consequently, a lower melt viscosity. For MB materials, actually, this phenomenon is less marked and the double processing of the clay has fewer consequences reasonably because the masterbatch prepa-

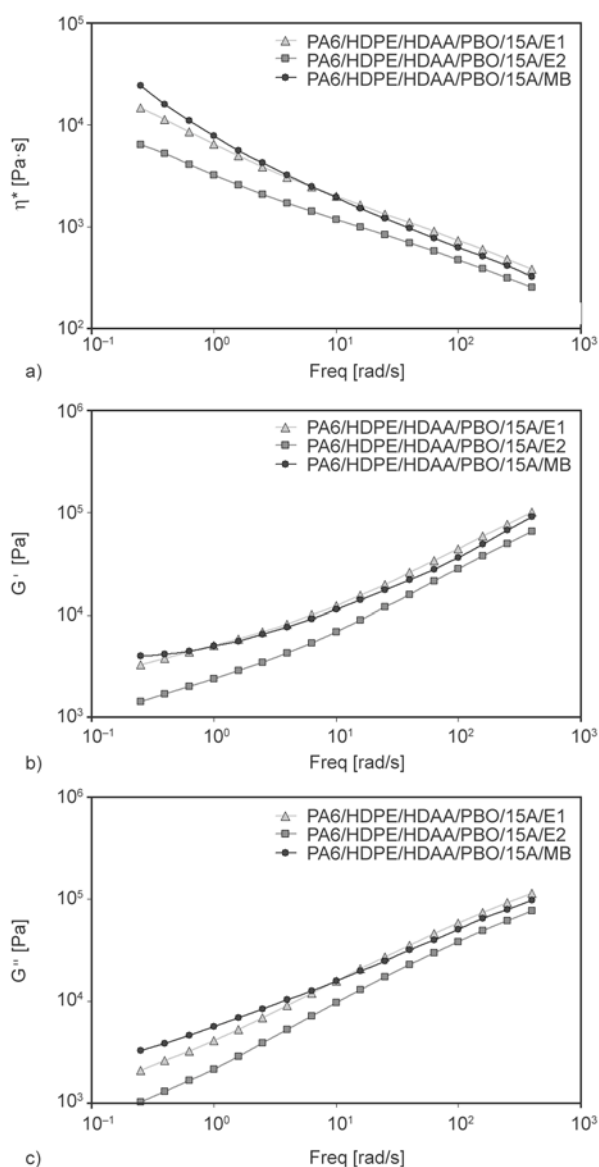


Figure 6. Complex viscosity (a), storage modulus (b) and the loss modulus (c) as a function of frequency of blend compatibilized with HDAA prepared by single extrusion (E1), re-extrusion (E2) and extrusion with a masterbatch (MB)

ration is carried out at 180°C, thus reducing the potential degradation effects on the clay after this step. Similar considerations can be done for the systems containing HDAA/PBO, Figure 6, and EGMA, Figure 7, even if in this latter case the reduction of viscosity is less relevant reasonably because of a minor compatibilizing effect of this agent and a lower antagonistic effect with the clay degradation products, confirming previous findings [26].

The analysis of the storage and loss moduli show that, for the EAA/PBO compatibilized blends, Figure 5, the differences in the rheological behaviour can be mainly attributed to the conservative compo-

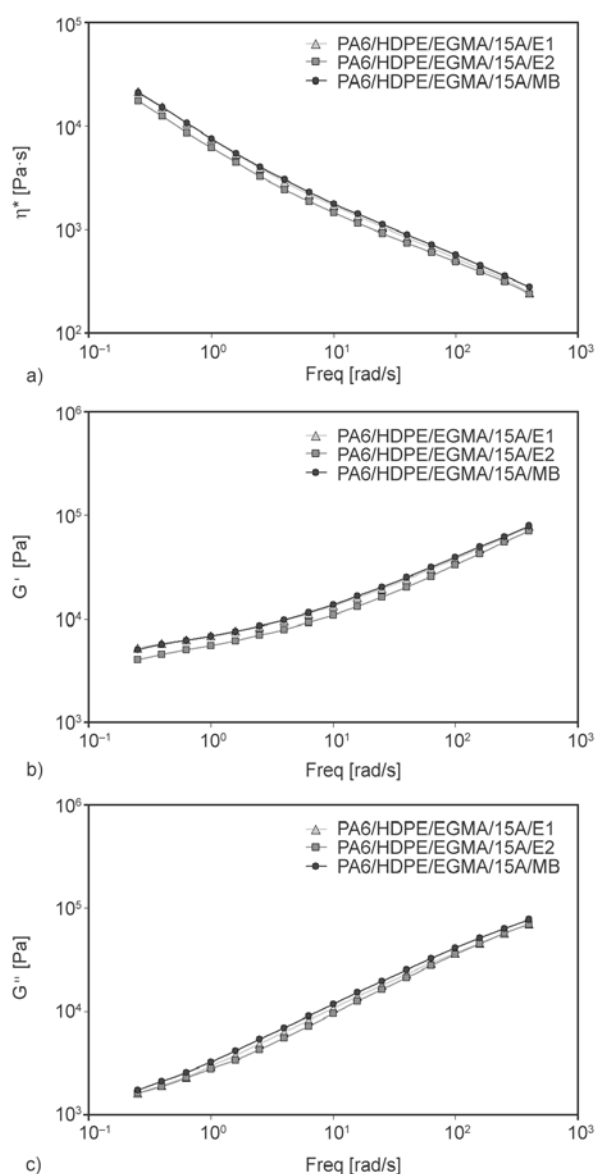


Figure 7. Complex viscosity (a), storage modulus (b) and the loss modulus (c) as a function of frequency of blend compatibilized with EGMA prepared by single extrusion (E1), re-extrusion (E2) and extrusion with a masterbatch (MB)

nent, G' , as the dissipative component, G'' , remains practically unaltered for E1, E2 and MB materials. This is not true for the HDAA containing materials, Figure 6 as both G' and G'' significantly change comparing E1/MB materials with E2. EGMA containing blends, finally, Figure 7, show very small differences in G' and G'' , thus corroborating the hypothesis of a bland activity of this compound as compatibilizing agent.

3.5. Mechanical characterization

In Table 4 it is reported the elastic modulus, E , the tensile stress, TS , the elongation at break, EB and

Table 4. Elastic modulus (*E*), tensile stress (*TS*), elongation at break (*EB*) and impact strength (*IS*) of compatibilized blends prepared by single extrusion (E1), re-extrusion (E2) and extrusion with a masterbatch (MB). The samples were prepared by compression moulding.

Sample	E [MPa]	TS [MPa]	EB [%]	IS [J/m]
PA6/HDPE/EAA/PBO/15A/E1	1283±32	23.6±0.3	3.1±0.1	24.0±1.0
PA6/HDPE/EAA/PBO/15A/E2	1348±39	23.4±0.4	3.4±0.2	28.5±0.9
PA6/HDPE/EAA/PBO/15A/MB	1452±43	23.8±0.3	4.0±0.2	33.3±1.1
PA6/HDPE/HDAA/PBO/15A/E1	1169±27	17.3±0.6	1.9±0.2	23.7±0.9
PA6/HDPE/HDAA/PBO/15A/E2	1229±33	21.6±0.4	2.4±0.1	30.3±1.0
PA6/HDPE/HDAA/PBO/15A/MB	1353±41	22.6±0.5	2.9±0.1	31.2±0.8
PA6/HDPE/EGMA/15A/E1	1173±28	23.3±0.8	5.0±0.3	28.3±0.7
PA6/HDPE/EGMA/15A/E2	1287±34	26.7±0.6	5.9±0.3	36.4±1.1
PA6/HDPE/EGMA/15A/MB	1297±28	27.3±0.7	7.5±0.4	42.0±1.3

the impact strength, *IS*, measured on compression moulded specimens of all the nanocomposites.

As regards all the compatibilized systems reprocessing (E2) induce an increase of all the properties for all the systems.

This improvement is in full agreement with the better blend morphology and with the improved clay distribution and intercalation after the second processing, as commented above. To go deeper inside this aspect, i.e. to investigate if the improvement of the mechanical properties was due to a better filler redistribution or to a finer polymer blend matrix morphology after reprocessing, unfilled materials were re-extruded and tested. The values of all the mechanical properties (here not reported for sake of brevity) do not show significant changes after the second processing for all the compatibilizing systems used, exception made for *EB* that shows a slight reduction. It can be therefore concluded that the improvement of the mechanical properties in the composites have to be attributed to the clay rather than to the polymer blend matrix.

Also the composites prepared using the compatibilizer-clay masterbatch show a general increase of the mechanical properties even if some specific comments must be given. The highest increase of Young's modulus can be found in the EAA containing system but the overall better improvement is found in the EGMA system. These results confirm that the pre-dispersion of the clay in the compatibilizer helps in achieving a further dispersion in the final material. Moreover, the differences in the performances of the different compatibilizers can be explained either with the different viscosity of the compatibilizers under the masterbatch preparation conditions. In particular, the lower the viscosity the lower the shear stress acting in the melt and the

worse the dispersion. In this sense, as reported in EAA and EGMA show the highest viscosities and therefore it is reasonable to suppose that the initial dispersion of the clay in the masterbatch preparation step is more effective than that of HDAA [26]. Of course, a different affinity between the compatibilizer and the clay leading to different melt interactions between the two components could be also taken into account.

As regards the impact strength, Table 4, it can be observed the same trend already evidenced in the tensile properties. *IS* is increasing according to $E1 < E2 < MB$. Again, the highest increase are observed for EAA and especially for EGMA containing materials while when using HDAA this increment is definitely lower. These results confirm that, beyond the better dispersion of the clay, there is also an improved adhesion between the filler and the matrix that enhances the stress transmission between the phases and, consequently, reduces crack propagation.

4. Conclusions

We studied the influence of morphology achieved by different processing methods, on the rheological and mechanical properties of PA6/HDPE-clay nanocomposite blends in the presence of different compatibilizing systems. The XRD and TEM analysis showed that the re-extrusion improves slightly the morphology probably because to the supplementary stresses induced on the blend by the second processing allowing a further dispersion of the nanofiller with consequent higher intercalation level. A further improvement of the morphology, in terms of lower clay dimension and better dispersion, can be observed in the blends MB. These results can be explained considering that the preparation of the

compatibilizer-clay masterbatch may induce a certain initial intercalation/expansion of the clay that becomes more intense during the subsequent extrusion processing. The rheological characterization showed that the E2 blends have a lower viscosity in comparison with the respective E1 blends. This can be likely interpreted with degradation phenomena occurring during the second reprocessing. Indeed, in E2 blends, HDPE, PA6 and the clay are exposed to high temperatures and mechanical stresses for a second time. On the contrary, the MB blends exhibited values of viscosity similar to E1 blends. This can be explained considering that the masterbatch preparation is carried out at 180°C, thus reducing the potential degradation effects on the clay after this step. The results of the mechanical tests showed that reprocessing (E2) induced an increase of all the properties for all the three systems. This improvement is in full agreement with the better blend morphology and with the improved clay distribution and intercalation after the second processing. A further general increase of the mechanical properties was showed by the blends MB. These results confirm that the pre-dispersion of the clay in the compatibilizer helps in achieving a further dispersion in the final material.

Acknowledgements

University of Palermo (ex 60% 2007).

References

- [1] Nazari T., Garmabi H.: Effect of organoclays on the rheological and morphological properties of poly (acrylonitrile-butadiene-styrene)/poly(methyl methacrylate)/clay nanocomposites. *Polymer Composites*, **33**, 1893–1902 (2012).
DOI: [10.1002/pc.22329](https://doi.org/10.1002/pc.22329)
- [2] Yu Z., Yin J., Yan S., Xie Y., Ma J., Chen X.: Bio-degradable poly(L-lactide)/poly(ϵ -caprolactone)-modified montmorillonite nanocomposites: Preparation and characterization. *Polymer*, **48**, 6439–6447 (2007).
DOI: [10.1016/j.polymer.2007.07.024](https://doi.org/10.1016/j.polymer.2007.07.024)
- [3] Bhatia A., Gupta R. K., Bhattacharya S. N., Choi H. J.: An investigation of melt rheology and thermal stability of poly(lactic acid)/poly(butylene succinate) nanocomposites. *Journal of Applied Polymer Science*, **114**, 2837–2847 (2009).
DOI: [10.1002/app.30933](https://doi.org/10.1002/app.30933)
- [4] Martín Z., Jiménez I., Gómez M. Á., Ade H., Kilcoyne D. A.: Interfacial interactions in PP/MMT/SEBS nanocomposites. *Macromolecules*, **43**, 448–453 (2010).
DOI: [10.1021/ma901952p](https://doi.org/10.1021/ma901952p)
- [5] Praveen S., Chattopadhyay P. K., Jayendran S., Chakraborty B. C., Chattopadhyay S.: Effect of rubber matrix type on the morphology and reinforcement effects in carbon black-nanoclay hybrid composites – A comparative assessment. *Polymer Composites*, **31**, 97–104 (2010).
DOI: [10.1002/pc.20772](https://doi.org/10.1002/pc.20772)
- [6] Naderi G., Lafleur P. G., Dubois C.: The influence of matrix viscosity and composition on the morphology, rheology, and mechanical properties of thermoplastic elastomer nanocomposites based on EPDM/PP. *Polymer Composites*, **29**, 1301–1309 (2008).
DOI: [10.1002/pc.20495](https://doi.org/10.1002/pc.20495)
- [7] Chow W. S., Mohd Ishak Z. A., Karger-Kocsis J., Apostolov A. A., Ishiaku U. S.: Compatibilizing effect of maleated polypropylene on the mechanical properties and morphology of injection molded polyamide 6/polypropylene/organoclay nanocomposites. *Polymer*, **44**, 7427–7440 (2003).
DOI: [10.1016/j.polymer.2003.09.006](https://doi.org/10.1016/j.polymer.2003.09.006)
- [8] Calcagno C. I. W., Mariani C. M., Teixeira S. R., Mauler R. S.: The role of the MMT on the morphology and mechanical properties of the PP/PET blends. *Composites Science and Technology*, **68**, 2193–2200 (2008).
DOI: [10.1016/j.compscitech.2008.03.012](https://doi.org/10.1016/j.compscitech.2008.03.012)
- [9] Hong J. S., Namkung H., Ahn K. H., Lee S. J., Kim C.: The role of organically modified layered silicate in the breakup and coalescence of droplets in PBT/PE blends. *Polymer*, **47**, 3967–3975 (2006).
DOI: [10.1016/j.polymer.2006.03.077](https://doi.org/10.1016/j.polymer.2006.03.077)
- [10] Paul D. R., Bucknall C. B.: *Polymer blends, formulation*. Wiley, New York (2000).
- [11] La Mantia F. P., Scaffaro R., Colletti C., Dimitrova T., Magagnini P., Paci M., Filippi S.: Oxazoline functionalization of polyethylenes and their blends with polyamides and polyesters. *Macromolecular Symposia*, **176**, 265–278 (2001).
DOI: [10.1002/1521-3900\(200112\)176:1<265::AID-MASY265>3.0.CO;2-I](https://doi.org/10.1002/1521-3900(200112)176:1<265::AID-MASY265>3.0.CO;2-I)
- [12] Liu X., La Mantia F. P., Scaffaro R.: Oxazoline-containing compatibilizers for polyamide/SAN and polyamide/ABS blends. *Journal of Applied Polymer Science*, **86**, 449–455 (2002).
DOI: [10.1002/app.11002](https://doi.org/10.1002/app.11002)
- [13] Scaffaro R., La Mantia F. P., Canfora L., Polacco G., Filippi S., Magagnini P.: Reactive compatibilization of PA6/LDPE blends with an ethylene-acrylic acid copolymer and a low molar mass bis-oxazoline. *Polymer*, **44**, 6951–6957 (2003).
DOI: [10.1016/j.polymer.2003.06.001](https://doi.org/10.1016/j.polymer.2003.06.001)

- [14] Utracki L. A.: Polymer blends handbook. Kluwer, Dordrecht (2003).
- [15] Scaffaro R., Botta L., La Mantia F. P., Magagnini P., Acierno D., Gleria M., Bertani R.: Effect of adding new phosphazene compounds to poly(butylene terephthalate)/polyamide blends. I: Preliminary study in a batch mixer. *Polymer Degradation and Stability*, **90**, 234–243 (2005).
DOI: [10.1016/j.polymdegradstab.2005.03.019](https://doi.org/10.1016/j.polymdegradstab.2005.03.019)
- [16] Scaffaro R., Botta L., La Mantia F. P., Gleria M., Bertani R., Samperi F., Scaltro G.: Effect of adding new phosphazene compounds to poly(butylene terephthalate)/polyamide blends. II: Effect of different polyamides on the properties of extruded samples. *Polymer Degradation and Stability*, **91**, 2265–2274 (2006).
DOI: [10.1016/j.polymdegradstab.2006.04.019](https://doi.org/10.1016/j.polymdegradstab.2006.04.019)
- [17] Robeson L. M.: Polymer blends: A comprehensive review. Hanser, Munich (2007).
- [18] Samperi F., Bazzano S., Battiato S., Scaffaro R., Botta L., Mistretta M. C., Bertani R., Milani R.: Reactions occurring during the melt mixing of nylon 6 and oxazoline–cyclophosphazene units. *Macromolecules*, **42**, 5579–5592 (2009).
DOI: [10.1021/ma9008466](https://doi.org/10.1021/ma9008466)
- [19] Filippone G., Dintcheva N. Tz., La Mantia F. P., Acierno D.: Selective localization of organoclay and effects on the morphology and mechanical properties of LDPE/PA11 blends with distributed and co-continuous morphology. *Journal of Polymer Science Part B: Polymer Physics*, **48**, 600–609 (2010).
DOI: [10.1002/polb.21928](https://doi.org/10.1002/polb.21928)
- [20] Ophir A., Dotan A., Belinsky I., Kenig S.: Barrier and mechanical properties of nanocomposites based on polymer blends and organoclays. *Journal of Applied Polymer Science*, **116**, 72–83 (2010).
DOI: [10.1002/app.31285](https://doi.org/10.1002/app.31285)
- [21] Contreras V., Cafiero M., Da Silva S., Rosales C., Perera R., Matos M.: Characterization and tensile properties of ternary blends with PA-6 nanocomposites. *Polymer Engineering and Science*, **46**, 1111–1120 (2006).
DOI: [10.1002/pen.20572](https://doi.org/10.1002/pen.20572)
- [22] Sharif-Pakdaman A., Morshedian J., Jahani Y.: Effect of organoclay and silane grafting of polyethylene on morphology, barrierity, and rheological properties of HDPE/PA6 blends. *Journal of Applied Polymer Science*, **127**, 1211–1220 (2013).
DOI: [10.1002/app.37974](https://doi.org/10.1002/app.37974)
- [23] Yoo Y., Park C., Lee S-G., Choi K-Y., Kim D. S., Lee J. H.: Influence of addition of organoclays on morphologies in nylon 6/LLDPE blends. *Macromolecular Chemistry and Physics*, **206**, 878–884 (2005).
DOI: [10.1002/macp.200400526](https://doi.org/10.1002/macp.200400526)
- [24] Fang Z., Xu Y., Tong L.: Effect of clay on the morphology of binary blends of polyamide 6 with high density polyethylene and HDPE-graft-acrylic acid. *Polymer Engineering and Science*, **47**, 551–559 (2007).
DOI: [10.1002/pen.20675](https://doi.org/10.1002/pen.20675)
- [25] Scaffaro R., Mistretta M. C., La Mantia F. P.: Compatibilized polyamide 6/polyethylene blend–clay nanocomposites: Effect of the degradation and stabilization of the clay modifier. *Polymer Degradation and Stability*, **93**, 1267–1274 (2008).
DOI: [10.1016/j.polymdegradstab.2008.04.008](https://doi.org/10.1016/j.polymdegradstab.2008.04.008)
- [26] Scaffaro R., Botta L., Mistretta M. C., La Mantia F. P.: Preparation and characterization of polyamide 6/polyethylene blend-clay nanocomposites in the presence of compatibilisers and stabilizing system. *Polymer Degradation and Stability*, **95**, 2547–2554 (2010).
DOI: [10.1016/j.polymdegradstab.2010.07.029](https://doi.org/10.1016/j.polymdegradstab.2010.07.029)
- [27] Scaffaro R., Mistretta M. C., La Mantia F. P., Frache A.: Effect of heating of organo-montmorillonites under different atmospheres. *Applied Clay Science*, **45**, 185–193 (2009).
DOI: [10.1016/j.clay.2009.06.002](https://doi.org/10.1016/j.clay.2009.06.002)
- [28] Scaffaro R., Botta L., Frache A., Bellucci F.: Thermo-oxidative ageing of an organo-modified clay and effects on the properties of PA6 based nanocomposites. *Thermochimica Acta*, **552**, 37–45 (2013).
DOI: [10.1016/j.tca.2012.11.007](https://doi.org/10.1016/j.tca.2012.11.007)
- [29] Goitisolo I., Eguiazabal J. I., Nazabal J.: Effects of reprocessing on the structure and properties of polyamide 6 nanocomposites. *Polymer Degradation and Stability*, **93**, 1747–1752 (2008).
DOI: [10.1016/j.polymdegradstab.2008.07.030](https://doi.org/10.1016/j.polymdegradstab.2008.07.030)
- [30] Karahaliou E-K., Tarantili P. A.: Preparation of poly (acrylonitrile–butadiene–styrene)/montmorillonite nanocomposites and degradation studies during extrusion reprocessing. *Journal of Applied Polymer Science*, **113**, 2271–2281 (2009).
DOI: [10.1002/app.30158](https://doi.org/10.1002/app.30158)
- [31] Abdel Gawad A., Esawi A. M. K., Ramadan A. R.: Structure and properties of nylon 6–clay nanocomposites: effect of temperature and reprocessing. *Journal of Materials Science*, **45**, 6677–6684 (2010).
DOI: [10.1007/s10853-010-4760-5](https://doi.org/10.1007/s10853-010-4760-5)
- [32] Russo G. M., Nicolais V., Di Maio L., Montesano S., Incarnato L.: Rheological and mechanical properties of nylon 6 nanocomposites submitted to reprocessing with single and twin screw extruders. *Polymer Degradation and Stability*, **92**, 1925–1933 (2007).
DOI: [10.1016/j.polymdegradstab.2007.06.010](https://doi.org/10.1016/j.polymdegradstab.2007.06.010)
- [33] Touati N., Kaci M., Bruzaud S., Grohens Y.: The effects of reprocessing cycles on the structure and properties of isotactic polypropylene/Cloisite 15A nanocomposites. *Polymer Degradation and Stability*, **96**, 1064–1073 (2011).
DOI: [10.1016/j.polymdegradstab.2011.03.015](https://doi.org/10.1016/j.polymdegradstab.2011.03.015)
- [34] Remili C., Kaci M., Benhamida A., Bruzaud S., Grohens Y.: The effects of reprocessing cycles on the structure and properties of polystyrene/Cloisite 15A nanocomposites. *Polymer Degradation and Stability*, **96**, 1489–1496 (2011).
DOI: [10.1016/j.polymdegradstab.2011.05.005](https://doi.org/10.1016/j.polymdegradstab.2011.05.005)

- [35] Scaffaro R., Botta L., Ceraulo M., La Mantia F. P.: Effect of kind and content of organo-modified clay on properties of PET nanocomposites. *Journal of Applied Polymer Science*, **122**, 384–392 (2011). DOI: [10.1002/app.34087](https://doi.org/10.1002/app.34087)
- [36] Botta L., Scaffaro R., La Mantia F. P., Dintcheva N. Tz.: Effect of different matrices and nanofillers on the rheological behavior of polymer-clay nanocomposites. *Journal of Polymer Science Part B: Polymer Physics*, **48**, 344–355 (2010). DOI: [10.1002/polb.21896](https://doi.org/10.1002/polb.21896)
- [37] Botta L., La Mantia F. P., Dintcheva N. Tz., Scaffaro R.: Rheological response of polyethylene/clay nanocomposites to annealing treatment. *Macromolecular Chemistry and Physics*, **208**, 2533–2541 (2007). DOI: [10.1002/macp.200700241](https://doi.org/10.1002/macp.200700241)
- [38] Shah R. K., Paul D. R.: Nylon 6 nanocomposites prepared by a melt mixing masterbatch process. *Polymer*, **45**, 2991–3000 (2004). DOI: [10.1016/j.polymer.2004.02.058](https://doi.org/10.1016/j.polymer.2004.02.058)
- [39] Filippone G., Dintcheva N. Tz., Acierno D., La Mantia F. P.: The role of organoclay in promoting co-continuous morphology in high-density poly(ethylene)/poly (amide) 6 blends. *Polymer*, **19**, 1312–1322 (2008). DOI: [10.1016/j.polymer.2008.01.045](https://doi.org/10.1016/j.polymer.2008.01.045)